

2012

## Surface Impedance of Superconducting Radio Frequency (SRF) Materials

Binping Xiao  
*College of William & Mary - Arts & Sciences*

Follow this and additional works at: <https://scholarworks.wm.edu/etd>



Part of the [Materials Science and Engineering Commons](#), and the [Physics Commons](#)

---

### Recommended Citation

Xiao, Binping, "Surface Impedance of Superconducting Radio Frequency (SRF) Materials" (2012).  
*Dissertations, Theses, and Masters Projects*. Paper 1539623605.  
<https://dx.doi.org/doi:10.21220/s2-pfac-0108>

This Dissertation is brought to you for free and open access by the Theses, Dissertations, & Master Projects at W&M ScholarWorks. It has been accepted for inclusion in Dissertations, Theses, and Masters Projects by an authorized administrator of W&M ScholarWorks. For more information, please contact [scholarworks@wm.edu](mailto:scholarworks@wm.edu).

Surface Impedance of Superconducting Radio Frequency (SRF) Materials

Binping Xiao

Ji'An City, JiangXi Province, China

Master of Science, Peking University, 2005  
Bachelor of Science, Peking University, 2002

A Dissertation presented to the Graduate Faculty  
of the College of William and Mary in Candidacy for the Degree of  
Doctor of Philosophy

Department of Applied Science

The College of William and Mary  
August, 2012

## APPROVAL PAGE

This Dissertation is submitted in partial fulfillment of  
the requirements for the degree of

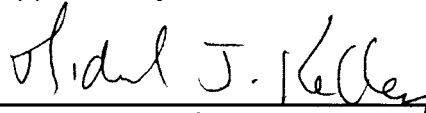
Doctor of Philosophy



---

Binping Xiao

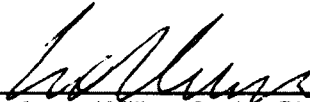
Approved by the Committee, May 2012



---

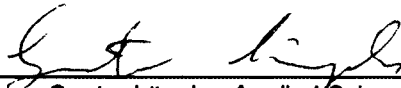
Committee Chair

Professor Michael J. Kelley, Applied Science Department  
The College of William and Mary



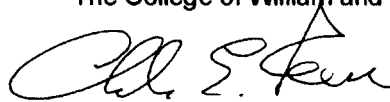
---

Professor William Cooke, Physics Department  
The College of William and Mary



---

Professor Gunter Luepke, Applied Science Department  
The College of William and Mary



---

Dr. Charles E. Reece, SRF Institute  
Thomas Jefferson National Accelerator Facility

## ABSTRACT PAGE

Superconducting radio frequency (SRF) technology is widely adopted in particle accelerators. There remain many open questions, however, in developing a systematic understanding of the fundamental behavior of SRF materials, including niobium treated in different ways and various other bulk/thin film materials that are fabricated with different methods under assorted conditions. A facility that can measure the SRF properties of small samples in a range of 2~40 K temperature is needed in order to fully answer these questions. The Jefferson Lab surface impedance characterization (SIC) system has been designed to attempt to meet this requirement. It consists of a sapphire-loaded cylindrical Nb  $TE_{011}$  cavity at 7.4 GHz with a 50 mm diameter flat sample placed on a non-contacting end plate and uses a calorimetric technique to measure the radio frequency (RF) induced heat on the sample. Driving the resonance to a known field on this surface enables one to derive the surface resistance of a relatively small localized area.  $TE_{011}$  mode identification has been done at room temperature and 4 K, and has been compared with Microwave Studio® and SuperFish simulation results. RF loss mechanisms in the SIC system are under investigation. A VCO phase lock loop system has been used in both CW and pulsed mode. Two calorimeters, with stainless steel and Cu as the thermal path material for high precision and high power versions, respectively, have been designed and commissioned for the SIC system to provide low temperature control and measurement. A power compensation method has been developed to measure the RF induced power on the sample. Simulation and experimental results show that with these two calorimeters, the whole thermal range of interest for SRF materials has been covered. The power measurement error in the interested power range is within 1.2% and 2.7% for the high precision and high power versions, respectively. Temperature distributions on the sample surface for both versions have been simulated and the accuracy of sample temperature measurements have been analysed. Both versions have the ability to accept bulk superconductors and thin film superconducting samples with a variety of substrate materials such as Al,  $Al_2O_3$ , Cu, MgO, Nb and Si. Tests with polycrystalline and large grain bulk Nb samples have been done at <15 mT magnetic field. Based on BCS surface impedance, least-squares fittings have been done using SuperFit2.0, a code developed by G. Ciovati and the author.

Microstructure analyses and SRF measurements of large scale epitaxial MgB2 films have been reported. MgB2 films on 5 cm dia. sapphire disks were fabricated by a Hybrid Physical Chemical Vapor Deposition (HPCVD) technique. The electron-beam backscattering diffraction (EBSD) results suggest that the film is a single crystal complying with a MgB2(0001)//Al2O3(0001) epitaxial relationship. The SRF properties of different film thicknesses (200 nm and 350 nm) were evaluated using SIC system under different temperatures and applied fields at 7.4 GHz. A surface resistance of  $9 \pm 2 \mu\Omega$  has been observed at 2.2 K.

Based on BCS theory with moving Cooper pairs, the electron states distribution at 0K and the probability of electron occupation with finite temperature have been derived and applied to anomalous skin effect theory to obtain the surface impedance of a superconductor with moving Cooper pairs. We present the numerical results for Nb.

**Dedicated to Lixiu Luo**

# TABLE OF CONTENTS

<b>ACKNOWLEDGMENTS</b> .....	vi
<b>LIST OF TABLES</b> .....	vii
<b>LIST OF FIGURES</b> .....	viii
<b>CHAPTER 1</b> .....	2
Introduction.....	2
1.1. Motivation.....	2
1.2. Organization of the Dissertation .....	5
<b>CHAPTER 2</b> .....	7
SRF Surface Impedance .....	7
2.1. Resonance in an RLC Series Circuit.....	7
2.2. Surface Impedance with Moving Cooper Pairs .....	11
<b>CHAPTER 3</b> .....	31
SRF Surface Impedance Measurement Techniques .....	31
3.1. Brief Review .....	31
3.2. Choice of Cavity Geometry .....	31

3.3. Choice of Measuring Technique .....	34
CHAPTER 4 .....	40
SRF Surface Impedance Characterization System – RF Portion.....	40
4.1. Introduction .....	40
4.2. Calculation on Simplified Model .....	41
4.3. SuperFish Simulation .....	44
4.4. RF Couplers .....	44
4.5. Sapphire .....	45
4.6. Choke Joints.....	47
4.7. $TE_{011}$ Mode Identification .....	48
4.8. RF Control Circuit .....	48
4.9. Summary .....	53
CHAPTER 5 .....	64
SRF Surface Impedance Characterization System – Calorimeter Portion .....	64
5. 1. Introduction .....	64
5. 2. Description of Apparatus.....	65
5. 3. Measurement Method and Operating Range .....	67
5.3.1. Measurement Method .....	67
5.3.2. Thermal Path Simulations and Measurements .....	68

5.3.3.	Pulsed Mode Operation .....	69
5.3.4.	Operating Range .....	70
5. 4.	Power Measurement Accuracy Analysis.....	71
5. 5.	Temperature Measurement Accuracy.....	74
5.5.1.	Thermal Contact Resistance Between Sample and Sample Holder .....	74
5.5.2.	Power Distribution on Sample.....	75
5.5.3.	Temperature Distribution on Sample.....	76
5.5.4.	Temperature Measurement Accuracy .....	77
5. 6.	Summary .....	78
CHAPTER 6 .....		89
SRF Surface Impedance Characterization System - Data Acquisition and Analysis ..		89
6.1.	Surface Impedance Characterization.....	89
6.1.1.	Calculation .....	89
6.1.2.	Surface Resistance .....	89
6.1.3.	Surface Reactance.....	90
6.2.	System Measurement Range, Accuracy and Resolution .....	91
6.2.1.	System Measurement Range.....	91
6.2.2.	System measurement accuracy .....	92
6.2.3.	System resolution.....	94



6.3.	Automated LabView Program for Surface Impedance Measurement .....	94
6.3.1.	Proportional–integral–derivative (PID) Feedback Control on Temperature .....	94
6.3.2.	Automated LabView™ Program for Surface Reactance Measurement	95
6.3.3.	Automated LabView™ Program for Surface Resistance Measurement	96
6.4.	Data Analysis Based on BCS Surface Impedance Fitting .....	96
6.5.	Measurements on Bulk Nb Samples .....	96
6.5.1.	Sample Preparation .....	97
6.5.2.	Transition Temperature .....	97
6.5.3.	Surface Reactance .....	97
6.5.4.	Surface Resistance .....	97
6.5.5.	Fitting Results .....	98
CHAPTER 7	.....	112
SRF Surface Impedance Characterization on MgB <sub>2</sub> Thin Films	.....	112
7.1.	Introduction .....	112
7.2.	Experimental details.....	114
7.3.	Surface characterization .....	116
7.4.	Surface impedance characterization.....	117
7.5.	Conclusion .....	120

Appendix A.....	127
Appendix B.....	134
Appendix C.....	143
Appendix D.....	147
Appendix E.....	149
Appendix F.....	150
Bibliography.....	152

# ACKNOWLEDGMENTS

There are many people who have contributed time, knowledge, skill and support to the successful completion of this dissertation.

Firstly I wish to extend my thanks to my advisors, Dr. Michael J. Kelley and Dr. Charles E. Reece, for their patience and guidance on my research, study and editing of this manuscript. Without their support and guidance, this work would not have been done. I also really appreciate Dr. Gunter Lüpke and Dr. William Cooke for taking time out of their busy schedule to serve as my dissertation committee members. Their attention, advice and review of this dissertation are extremely valuable for me.

Secondly I wish to acknowledge the exceptional support from SRF institute in Jefferson Lab: Dr. Larry Philips, Dr. Rongli Geng, Dr. Haipeng Wang, Dr. Genfa Wu (Now in Argonne National Lab) for their helpful instruction and discussion; Dr. Xin Zhao, Dr. Hui Tian, Dr. Grigory Ereemeev, Dr. Gianluigi Ciovati, Anne-Marie Valente-Feliciano, Dr. Peter Kneisel, Dr. Robert Rimmer, Dr. Andy T. Wu, Jared Nance, Joshua Spradlin, Dr. Frank Marhauser and Dr. Jiquan Guo for their help during the experiments and the production of this thesis; Carolyn Camp, for her helpful communication and organization; Pete Kushnick and Tiffany Bass, for their supports on cryogenic operation; Stephen Dutton and Michael Morrone, for their electric supports, and more than that; Scott Williams and Tom Elliott for their supports on the brazing work; Danny Machie and Monroe Major for their help on engineer drawings; Thomas Goodman, Daniel Forehand and Roland Overton for their supports on crane operation; Gary Slack and Casy Apeldoorn for their supports in the machine shop; David Bigelow for his support on leak check of the calorimeter system; Christiana Grenoble for her support on LabView and computer security; Andrew Burrill for his support on high pressure rinse of the SIC cavity; Gary Chen for his help on Ansys simulations; Tom Powers for his help on the VCO-PLL control system. I would also like to express my sincere gratitude to Dr. Xiaoxing Xi and Teng Tan from Temple University and Dr. Tsuyoshi Tajima from Los Alamos National Lab for their MgB<sub>2</sub> samples.

Thirdly I would like to thank my officemates, Dr. Daniel Bowring, Liang Zhao, Chen Xu, Dr. Song Jin, Dr. Jin Dai, Feisi He and Yongming Li. I would also like to thank all my friends in the College of William and Mary, in Jefferson Lab, in Old Dominion University and in Peking University.

Finally, I wish to express my deepest thank for the unconditional trust, love and support from my family.

## LIST OF TABLES

Table 2.1. Matrix elements of single particle scattering operator with moving cooper pairs, compared to BCS theory table II. ....	24
Table 2.2. Mean square matrix elements for possible values of $W_i-W_f$ , compared to BCS theory table III.....	27
Table 3.1. Comparison of RF surface characterization systems.....	39
Table 6.1. Key Parameters to Derive Surface Impedance .....	100
Table 6.2. PID values for different temperature zone with temperature up to 50 K.	101
Table 7.1. Summary of difference in fabrication conditions and measurement results for MgB <sub>2</sub> samples. ....	122

# LIST OF FIGURES

Figure 1.1. A simplified diagram of SRF device [13].	6
Figure 2.1. RLC series circuit.	28
Figure 2.2. Energy gap at 2 K and critical temperature versus Cooper pair velocity with parameters set for Nb. The energy gap at zero Cooper pair velocity is 1.476 meV.	29
Figure 2.3. Surface resistance (red line) and reactance (blue dotted line) versus Cooper pair velocity for Nb at 2 K and 1.5 GHz.	30
Figure 4.1. SIC system overview. A. Cap for sapphire rod, B. Sapphire rod, C. RF coupler, D. Nb cavity body, E. TE011 cavity, F. Double choke joints, G. Sample on top of copper sample holder, H. Stainless steel sample clamp, I. G-10 washer (x6), J. Aluminium bolt (x6), K. Upper and lower thermal insulators, L. Ring heater, M. Port for vacuum and wires. (Vacuum port of the cavity is not shown), N. Thermal sensor mounted on spring, O&P. Thermal sensor, Q. Coupler tuning mechanism, R. Distance tuning mechanism (x3).	55
Figure 4.2. Simplified model of the SIC system with blue color section sapphire and white color section vacuum.	56
Figure 4.3. Magnetic field intensity distribution on the sample surface, normalized to the peak magnetic field intensity on the cavity.	57
Figure 4.4. Maximum magnetic fields on the sample per stored energy under different gap condition for 2 <sup>nd</sup> generation cavity with 0.06 inch cap, based on SuperFish 2D simulation.	58
Figure 4.5. Couplers' external Q versus position.	59
Figure 4.6. Sapphire rod length calculation to the radiation loss external Q in SIC cavity.	60
Figure 4.7. Misalignment of sapphire's physical axis to the axis of Nb cavity, here $\alpha = 10$ degrees is illustrated for visibility only.	61

Figure 4.8. Tuning sensitivity of TE <sub>011</sub> mode: simulation, room temperature and 4 K measurement. ....	62
Figure 4.9. RF control circuit for SIC system. ....	63
Figure 5.1. Simplified thermal model of calorimeter system. A. Sample, B. Sample Holder, C. OFHC copper ring, D. Liquid helium bath, E. Thermal contact impedance between sample and sample holder, F. Thermal impedance of the upper insulator, G. Thermal impedance of the lower insulator. ....	80
Figure 5.2. For the high power calorimeter, temperature on the top surface of sample (line 1), on sensor N (line 2) and on sensor O (line 3) shown in Figure 4.1 as a function of heater power on the top surface of sample, with temperature on sensor O (line 4, shorter than line 3) as a function of heater power from heater L. Red dots show the calculation results based on the 1-D model. ....	81
Figure 5.3. For the high precision calorimeter, temperature on the top surface of sample (green line), on sensor O shown Figure 4.1 as a function of heater power on the top surface of sample (orange line), with temperature on sensor O as a function of heater power from heater L (blue line). The above three lines are overlapped together. Red dots show the calculation results based on the 1-D model. ....	82
Figure 5.4. Power range requested by SRF sample characterization as a function of sample temperature (blue dotted line). Power range for high precision (red) and high power (black) version calorimeters as a function of sample temperature. ....	83
Figure 5.5. Thermal contact resistance between sample and sample holder (red dots). Blue line is the fitting. ....	84
Figure 5.6. RF induced heat distribution on sample. ....	85
Figure 5.7. Ansys <sup>TM</sup> model of calorimeter system with materials: ■ (dark blue) Nb, ■ (orange) Cu, ■ (gray) Stainless steel/Cu for high precision/high power version, ■ (purple) Interlayer between the sample and the sample holder. ....	86
Figure 5.8. Temperature distribution on the 2 cm dia. center area of sample top surface for (a) high precision calorimeter with 30 mW power and (b) high power calorimeter with 2.2 W power, both powers are applied to RF-exposed central area. ....	87
Figure 5.9. Temperature difference between sensor N in Figure 4.1 and the sensor on top of sample G versus temperature on top of sample G, with power on heater L (blue dots) and with power on the heater on sample (read dots) for high precision version calorimeter system. ....	88

Figure 6.1. Measurement capability range of the SIC system. BCS resistance and lower critical field of $MgB_2$ , $Nb_3Sn$ and $NbN$ at 7.5 GHz and different temperature are noted.....	102
Figure 6.2. Measurement capability range of the SIC system. Materials of potential interest, power limits for two TWT amplifiers are noted. ....	103
Figure 6.3. Surface reactance measurement flow chart. ....	104
Figure 6.4. Surface reactance measurement LabView™ front panel. ....	105
Figure 6.5. Surface resistance measurement LabView™ front panel. ....	106
Figure 6.6. Graphic user interface of BCS surface impedance fitting program SuperFit2.0, revised from code SuperFit developed by G. Ciovati.....	107
Figure 6.7. Setup for 1:1:2 buffered chemical polish (BCP) solution of HF (49% wt), $HNO_3$ (69% wt), and $H_3PO_4$ (85% wt) on bulk Nb brazed on Cu substrate. ....	108
Figure 6.8. Penetration depth change versus sample temperature for a large grain bulk Nb sample brazed on a Cu substrate, solid line shows the BCS fit result. ....	109
Figure 6.9. Surface resistance changes with sample temperature for polycrystalline (A) and large grain (B) Nb brazed on Cu substrate. ■ (red) Measured $R_s$ , — (red) Theoretical value with BCS fit results. — (blue) BCS resistance. ....	110
Figure 6.10. Surface resistance versus peak RF magnetic field at 2.5 K for a large grain bulk Nb sample brazed onto a Cu substrate. ....	111
Figure 7.1. Electron backscattering diffraction (EBSD) results of a $MgB_2$ film on C-plane sapphire. a). a scanning electron micrograph (SEM) of a survey area, the inset at top-right is a representative Kikuchi diffraction image, which shows clear diffraction bands. b). a color-coded inverse pole figure (IPF) of the same area, the inset at top-right is the color-coded crystallographic legend. c). and d). are the PFs being deduced from the EBSD survey in (0001) and (1,1,-2,1) representations respectively. ....	123
Figure 7.2. ◆ (blue) $MgB_2$ -200-I with $T_c$ at 39.3 K ● (green) $MgB_2$ -350 with $T_c$ at 39.5 K Penetration depth versus sample temperature of $MgB_2$ on sapphire substrate – BCS penetration depth. ....	124
Figure 7.3. ◆ (blue) $MgB_2$ -200-I ▲ (red) $MgB_2$ -200-II ● (green) $MgB_2$ -350 Effective surface resistance versus sample temperature of $MgB_2$ on sapphire substrate	

■ (purple) Surface resistance versus sample temperature of large grain Nb sample.  
.....125

Figure 7.4. Effective surface resistance of MgB<sub>2</sub>-350 versus magnetic field at 3 K  
sample temperature. ....126



# SURFACE IMPEDANCE OF SUPERCONDUCTING RADIO FREQUENCY (SRF) MATERIALS

# CHAPTER 1

## Introduction

### 1.1. Motivation

Superconducting radio frequency (SRF) technology is widely and increasingly adopted for use in particle accelerators [1-12]. SRF technology applies superconductors, normally niobium or niobium thin film deposited on copper, to conventional RF devices for particle accelerators.

Figure 5.1 shows a simplified SRF device [13]. In this SRF device, a single cell niobium cavity has been put into a liquid helium vessel, and then surrounded by a vacuum thermal insulating vessel. The RF power has been coupled into the cavity with input RF antenna shown on the left side of the cavity in this Figure. Charged particles coming from the left side could be accelerated by the electromagnetic field ( $TM_{010}$  mode in most cases) in the cavity [14]. The SRF technology greatly reduces the RF power dissipation on the SRF devices comparing with conventional RF devices. For a Continuous Electron Beam Accelerator Facility (CEBAF) shape 1.5GHz cavity or a TeV-Energy Superconducting Linear Accelerator (TESLA) shape 1.3GHz cavity, the RF energy loss of niobium cavity at 2 K temperature is 5 orders of

magnitude lower than that of copper cavity at room temperature. Comparing to normal conducting RF devices, the low RF loss guarantees more of the RF power to be used to accelerate charged particles, ensures the SRF devices possible to work at high duty cycle or even CW mode, and also allows the devices more suitable for high current accelerators, because it allows the devices geometry to have larger beam pipe apertures and to minimize deleterious interactions (“beam impedance”) to a particle beam [14]. These properties make SRF technology widely adopted in high average power Free Electron Laser (FEL), storage ring, Energy Recovery Linac (ERL).

Among the various projects that uses SRF technology, the Free-electron LASer in Hamburg (FLASH) program at Deutsches Elektronen-Synchrotron (DESY) in Germany uses 48 9-cell cavities to get 1 GeV electron beam [1]; the X-ray Free Electron Laser (X-FEL) program by DESY in Germany uses 800 9-cell cavities to get 17.5 GeV electron beam [2]; the CEBAF at Thomas Jefferson National Accelerator Facility (JLab) in United States adds 80 7-cell cavities to the existing 338 5-cell cavities to upgrade the beam energy from 6 GeV to 12 GeV [3]; the Spallation Neutron Source (SNS) program at Oak Ridge National Lab (ORNL) in United States uses 117 6-cell cavities to get 1.3 GeV proton beam (with power upgrade plans) [4]; the Soreq Applied Research Accelerator Facility (SARAF) at Soreq Nuclear Research Center (NRC) in Israel uses 44 Half Wave Resonators (HWRs) to get 40 MeV proton/deuteron beam (with phase II) [5]. There are also many colliders, storage rings and ERLs that using SRF technology: the National Synchrotron Light Source-II (NSLS-II) at Brookhaven National Laboratory (BNL) in United States [6]; the

Cornell Electron Storage Ring (CESR) at Cornell University in United States [7]; the Beijing Electron Positron Collider-II (BEPC-II) at Institute of High Energy Physics (IHEP) in China [8]; the KEKB electron–positron collider at Kō Enerugī Kasokuki Kenkyū Kikō (KEK) in Japan [9]; the Peking University ERL-FEL (PKU-ERL-FEL) at PKU in China [8]; the Accelerators and Lasers In Combined Experiments ERL (ALICE-ERL) at Daresbury in UK [10]; the BNL-ERL at BNL in United States [11].

The International Linear Collider (ILC) is a proposed high energy physics project to collide electrons with positrons at 500 GeV (upgradeable to 1 TeV) [12]. This project will use 16,000 9-cell cavities working at 31.5 MV/m gradient to accelerate electron/positron beam to 500 GeV/500 GeV. The total length of this collider will be 19 to 31 miles.

With the expansion of SRF technique worldwide, there remains a need for a systematic understanding of the fundamental behavior of candidate SRF materials, including niobium treated in different ways and various other bulk/thin film materials. The RF surface impedance of superconductors, especially its real part, the RF surface resistance  $R_s$ , is of great importance for the performance of SRF cavities. Measurements of  $R_s$  via quality factor measurements with typical cavities are inherently a weighted average over significantly large, curved surfaces. Thermometric mapping of cavities reveals, however, that  $R_s$ , especially as a function of magnetic flux density, is quite non uniform. To enable definitive correlation of localized losses with localized SRF material characteristics, a facility that can accurately measure the SRF properties of small samples in a range of 0~180 mT

surface magnetic flux density and 2~40 K temperature, with surface resistances down to the BCS limit (several hundred  $n\Omega$  for Nb and can be as low as 1  $n\Omega$  for other materials like NbN, at 2 K and 7.5 GHz in our case) is needed. Utilizing small sample sizes is beneficial to improve the surface preparation and quality control of the samples to better characterize localized material details. In addition, undesirable effects arising from the sample edges should be avoided. The Jefferson Lab surface impedance characterization system (SIC) [15] has been designed to attempt to meet this requirement.

## **1.2. Organization of the Dissertation**

This dissertation is organized as follows.

In Chapter 2 the SRF surface impedance is introduced and the theoretical calculation with moving Cooper pairs under RF field is given, based on BCS theory and anomalous skin effect.

In Chapter 3 a brief review on SRF surface impedance measurement techniques is given.

In Chapter 4 the SIC RF system is described in detail.

In Chapter 5 the SIC calorimeter system is described in detail.

In Chapter 6 measurement results on bulk Nb are reported.

In Chapter 7 measurement results on thin film  $MgB_2$  are reported.

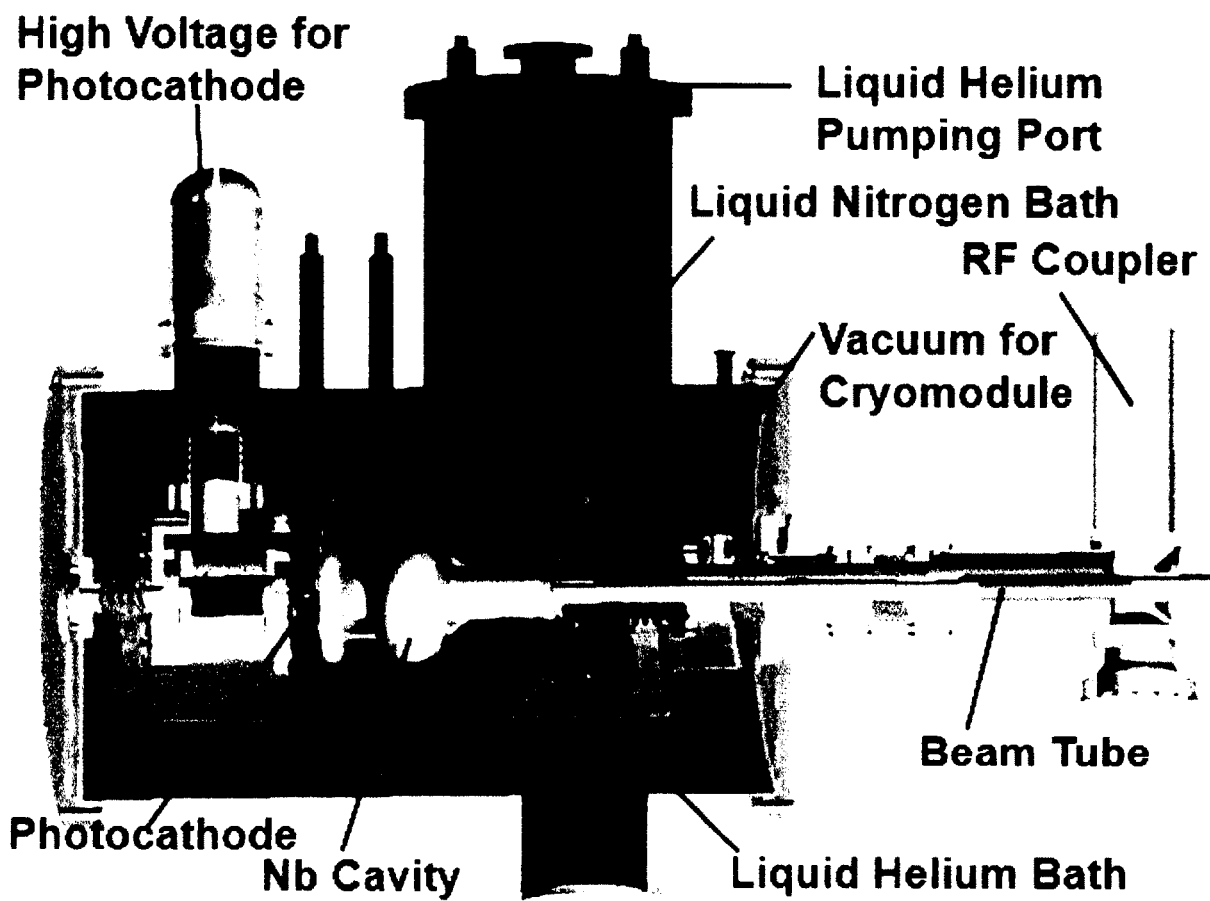


Figure 1.1. A simplified diagram of SRF device [13].

## CHAPTER 2

### SRF Surface Impedance

#### 2.1. Resonance in an RLC Series Circuit

For an SRF cavity at frequencies nearby a resonance mode, it can be modeled as an RLC circuit [16]. In a series RLC circuit that contains a resistor R, a capacitor C and an inductor L, shown in Figure 2.1, while an AC voltage  $u(t) = u_0 e^{i\omega t}$  has been applied, the current I could be solved from:

$$RI + L \frac{dI}{dt} + \frac{1}{C} \int I dt = u_0 e^{-i\omega t}$$

Which leads to:

$$I(t) = \frac{u_0}{\sqrt{R^2 + (\omega L - \frac{1}{\omega C})^2}} e^{i(\omega t - \varphi)}$$

$$\text{Where } \varphi = \arctan\left(\frac{\omega L - \frac{1}{\omega C}}{R}\right)$$

Impedance is defined as the ratio between voltage and current. The impedance of this RLC series circuit is:

$$Z = Z_0 e^{i\varphi} = \frac{u(t)}{I(t)} = \sqrt{R^2 + (\omega L - \frac{1}{\omega C})^2} e^{i\varphi} = R + i(\omega L - \frac{1}{\omega C})$$

$Z_0$  represents the amplitude change between voltage and current and  $\varphi$  represents the phase change between them. The real part of impedance is called resistance and the imaginary part is reactance.

Resonance phenomena occur while the system oscillates with larger amplitude at some frequencies. In the RLC series circuit, for a voltage with given amplitude, the current has a maximum amplitude at frequency  $\omega_0 = \frac{1}{\sqrt{LC}}$ , it is the resonant frequency of this RLC series circuit. At this frequency, the reactance of this circuit shrinks to 0 and the impedance shows only resistance, the stored energy in this circuit is  $U = \frac{Lu_0^2}{Z_0^2}$ , which is the total of the average magnetic energy stored in the inductor and the average electric energy stored in the capacitor, the power dissipation is  $P_{diss} = U \frac{R}{L}$ , and the quality factor is  $Q = \frac{1}{R} \sqrt{\frac{L}{C}}$ . The peak voltage on the capacitor is  $u_c = Qu_0$ , an RLC series circuit magnifies the AC voltage to as high as Q times of the input voltage. For an appropriately shaped cavity mode, it could be used as the accelerating voltage for charged particles, the ratio between effective accelerating voltage for particle traveling with finite velocity and peak voltage is the transit time factor.

The surface impedance of a conducting material is defined as the ratio between the E field and the H field parallel to the material surface [17].

$$Z = R + i\omega L = R + i\omega\mu_0\lambda_L$$



An SRF Cavity can be represented by an RLC series circuit, with total impedance:

$$Z_{\text{total}} = R + i\omega L + i\omega L_v - i \frac{1}{\omega C_v}$$

In this expression the first term is surface resistance, the second term is surface reactance, the combination of first two terms are surface impedance. The surface impedance is decided by the top most layers of the cavity material and is directly related to the surface treatment technique. In the last two terms,  $L_v$  and  $C_v$  represent the inductance and capacitance of the vacuum space in the cavity, which is decided by the geometry of the cavity.

The resonant frequency is  $\omega_0 = \frac{1}{\sqrt{(L+L_v)C_v}}$ , the stored energy in this circuit is  $U = (L + L_v) \frac{u_0^2}{Z_0^2}$ , twice the average magnetic energy stored in the inductor, and also twice the average electric energy stored in the capacitor, the power dissipation is  $P_{\text{diss}} = U \frac{R}{L+L_v}$ , and the quality factor is  $Q = \frac{1}{R} \sqrt{\frac{L+L_v}{C_v}}$ . The stored energy, power dissipation and quality factor also satisfy:

$$U = \frac{1}{2} \mu_0 \iiint H^2 dv = \frac{1}{2} \epsilon_0 \iiint E^2 dv$$

$$P_{\text{diss}} = \frac{R}{2} \iint H^2 ds$$

$$Q = \frac{1}{R} \frac{\omega_0 \mu_0 \iiint H^2 dv}{\iint H^2 ds}$$

$s$  is the interior surface of the cavity and  $v$  is the interior volume of the cavity.

Here  $G = \frac{\omega_0 \mu_0 \iiint H^2 dv}{\iint H^2 ds}$  is geometry dependent only, defined as geometry factor of this cavity, so that  $Q = \frac{G}{R}$ .

The electric energy is stored inside the vacuum space of the cavity, average value is  $E_e = \frac{1}{4} \mu_0 \iiint H^2 dv$ . A large portion of the magnetic energy is stored inside the vacuum space of the cavity, average value is  $E_m = \frac{L_v}{4(L+L_v)} \mu_0 \iiint H^2 dv$ . A small portion of the magnetic energy is stored on the cavity interior surface, average value is  $E_s = \frac{L}{4(L+L_v)} \mu_0 \iiint H^2 dv$ . And the average dissipation energy is  $E_{diss} = \frac{P_{diss}}{\omega_0} = \frac{R}{2\omega_0(L+L_v)} \mu_0 \iiint H^2 dv$ . The ratio between them is:

$$E_{diss} : E_s : E_m : E_e = R : \frac{\omega_0 L}{2} : \frac{\omega_0 L_v}{2} : \frac{1}{2\omega_0 C_v}$$

Now we consider a TE<sub>011</sub> cylindrical cavity with resonance frequency at 7.5 GHz and 300 Ω geometry factor,  $L_v = 6 \times 10^{-9}$  H and  $C_v = 7 \times 10^{-14}$  F, reactance from inductance is 300 Ω and reactance from capacitance is -300 Ω. For Cu at room temperature, surface resistance is 0.02 Ω and surface reactance is 0.045 Ω [17, 18]. For Nb at 2 K temperature, surface resistance is 300 nΩ and surface reactance is 2 mΩ, calculated from BCS theory [19]. The ratio  $E_{diss} : E_s : E_m : E_e$  is 0.02:0.0225:150:150 = 1:1.125:7500:7500 for Cu cavity at room temperature and  $300 \times 10^{-9} : 10^{-3} : 150 : 150 = 1:3333:5 \times 10^8 : 5 \times 10^8$  for Nb cavity at 2 K temperature, the quality factor would be 15000 for Cu cavity at room temperature and  $5 \times 10^8$  for Nb cavity at 2 K temperature and 7.5 GHz.

## 2.2. Surface Impedance with Moving Cooper Pairs

The RF surface impedance of a superconductor is a consequence that Cooper pairs in this superconductor cannot follow the change of the RF magnetic field  $H$  due to their mass, or inertia. The incomplete shielding of RF field indicates the ability of the superconductor to store RF energy inside its surface, which is also represented by surface reactance, the imaginary part of surface impedance. The RF field that enters the superconductor will interact with quasi-particles, causing RF power dissipation, which is represented by surface resistance, the real part of surface impedance. Based on the BCS theory [20] and anomalous skin effect theory [21], a derivation of a superconductor's surface impedance, called Mattis-Bardeen theory, has been successfully achieved [19, 21]. In reference [22], Mattis-Bardeen theory has been written in terms of the Fourier components of current  $\mathbf{j}(\mathbf{p})$  and vector potential  $\mathbf{A}(\mathbf{p})$  by defining  $K(p)$  as,

$$\mathbf{J}(\mathbf{p}) = -\frac{c}{4\pi} K(p) \mathbf{A}(\mathbf{p}) \quad (1)$$

where

$$K(p) = \frac{-3}{4\pi\hbar v_F \lambda_L^2(0)} \int_0^\infty \int_{-1}^1 e^{ipRu} e^{-\frac{R}{l}} (1-u^2) \times I(\omega, R, T) dudR = \frac{-3}{4\pi\hbar v_F \lambda_L^2(0)} \int_0^\infty \frac{4}{(pR)^2} \left[ \frac{\sin(pR)}{pR} - \cos(pR) \right] e^{-\frac{R}{l}} \times I(\omega, R, T) dR \quad (2)$$

with  $v_F$  the Fermi velocity,  $\lambda_L(0)$  the London penetration depth at 0 K,  $\omega$  the angular frequency of the RF field. The integration over  $R$  and  $u$  are the space and angular

integration, respectively. The term  $I(\omega, R, T)$  is calculated from the single-particle scattering operator based on BCS theory, one could refer to [21] for more detail.

The surface impedance of superconductors with random scattering at the surface is [22],

$$Z = i\pi\omega\mu_0\left\{\int_0^\infty \ln[1 + K(p)/p^2]dp\right\}^{-1} \quad (3)$$

The Mattis-Bardeen theory, however, did not consider field-dependent effects. The RF field could directly affect the directional velocity of Cooper pairs ( $v_S$ ) additional to their random movement, which is [23],

$$v_S(H) = \frac{\pi}{2^{3/2}} \frac{H}{H_c} \frac{\Delta_0}{p_F}$$

with  $H_c$  the critical RF field,  $\Delta_0$  the energy gap without field and  $p_F$  the Fermi momentum.

In SRF applications, the field dependence of surface impedance, especially its real part, surface resistance, is of great interest. Based on Rogers and Bardeen's work [24], the field dependence of surface resistance has been calculated with simplified models: Kulik and Palmieri [25] use a model that the energy gap could be reduced by the existence of an RF field,  $\Delta = \Delta_0 - p_F v_S(H)$  [24], with  $\Delta$  the energy gap with field; and Gurevich [23] used a model based on the field dependence of the quasi-particle distribution function [24].

Here, starting from the BCS theory with a net current in a superconductor, the electron states distribution at 0 K and the probability of electron occupation with finite temperature have been calculated and applied to anomalous skin effect theory,

which describes the response of metals to high frequency electromagnetic field in low temperature, yielding a new form of Cooper pair velocity dependence of the surface impedance.

In BCS theory, paired particles in the ground state, with total mass  $2m$  and zero total momentum that occupy state  $(\mathbf{k}\uparrow, -\mathbf{k}\downarrow)$ , with velocity  $\mathbf{v}_k$  in random direction, and energy relative to the Fermi sea  $\varepsilon_F$  to be  $\varepsilon_k$ , have been considered to give minimum free energy for superconductors. States with a net flow in a certain direction can be obtained by taking a pairing  $(\mathbf{k}+\mathbf{q}\uparrow, -\mathbf{k}+\mathbf{q}\downarrow)$ , with total momentum  $2\mathbf{q}$  the same for all Cooper pairs, corresponding to net velocity  $\mathbf{v}_s = \hbar\mathbf{q}/m$ .

With temperature  $T$  close to 0 and a net current flow, the probability of the state  $(\mathbf{k}+\mathbf{q}\uparrow, -\mathbf{k}+\mathbf{q}\downarrow)$  being occupied by a pair of particles is  $h_k$ . With a finite  $T$ , single electrons start to appear,  $f_{-\mathbf{k}+\mathbf{q}\downarrow}$  is defined as the probability that state  $-\mathbf{k}+\mathbf{q}\downarrow$ , with Bloch energy relative to the Fermi sea of  $\varepsilon_{-\mathbf{k}+\mathbf{q}}$ , being occupied, and  $f_{\mathbf{k}+\mathbf{q}\uparrow}$ , that probability for state  $\mathbf{k}+\mathbf{q}\uparrow$ , with Bloch energy relative to the Fermi sea to be  $\varepsilon_{\mathbf{k}+\mathbf{q}}$ . We have,

$$\varepsilon_{\mathbf{k}+\mathbf{q}} = \frac{1}{2}m(\mathbf{v}_k + \mathbf{v}_s)^2 - \varepsilon_F = \varepsilon_k + \varepsilon_s + \varepsilon_{ext} \quad (4)$$

$$\varepsilon_{-\mathbf{k}+\mathbf{q}} = \frac{1}{2}m(-\mathbf{v}_k + \mathbf{v}_s)^2 - \varepsilon_F = \varepsilon_k + \varepsilon_s - \varepsilon_{ext} \quad (5)$$

with  $\varepsilon_s = \frac{1}{2}m\mathbf{v}_s^2$ ,  $\varepsilon_{ext} = m\mathbf{v}_k\mathbf{v}_s = \sqrt{2m(\varepsilon_F + \varepsilon_k)}\mathbf{v}_s\chi \approx p_F\mathbf{v}_s\chi$  and  $\chi = \cos\alpha$ ,  $\alpha$  is the angle between  $\mathbf{v}_k$  and  $\mathbf{v}_s$ , from 0 to  $\pi$ .  $\mathbf{k}_F$  is Fermi wave vector.

We define  $h_k$  the probability that state  $(-k+q\downarrow, k+q\uparrow)$  is occupied by a ground pair while  $T \rightarrow 0$ , and define  $s_{-k+q\downarrow}$  the probability that  $-k+q\downarrow$  is occupied and  $k+q\uparrow$  is empty,  $s_{k+q\uparrow}$  for vice versa,  $p_k$  the probability that state  $(-k+q\downarrow, k+q\uparrow)$  is occupied by a pair of excited particles, and

$$s_{-k+q\downarrow} = f_{-k+q\downarrow}(1 - f_{k+q\uparrow}) \quad (6)$$

$$s_{k+q\uparrow} = f_{k+q\uparrow}(1 - f_{-k+q\downarrow}) \quad (7)$$

$$p_k = f_{-k+q\downarrow}f_{k+q\uparrow} \quad (8)$$

$$1 - s_{-k+q\downarrow} - s_{k+q\uparrow} - p_k = (1 - f_{-k+q\downarrow})(1 - f_{k+q\uparrow}) \quad (9)$$

$f$  is the distribution function for excited particles. Above the Fermi surface with  $k > k_F$   $f$  refers to electron occupation, and below the Fermi surface with  $k < k_F$   $f$  refers to hole occupation. (9) is the probability that state  $(-k+q\downarrow, k+q\uparrow)$  is occupied by a pair of ground state particles. For  $-k+q\downarrow$  with  $k > k_F$ , the occupation of single electrons, excited pairs of electrons and ground state pairs of electrons are  $s_{-k+q\downarrow}$ ,  $p_k(1-h_k)$  and  $(1-f_{-k+q\downarrow})(1-f_{k+q\uparrow})h_k$ , respectively; For  $-k+q\downarrow$  with  $k < k_F$ , the occupation of single holes, excited pairs of holes and ground state pairs of holes are  $s_{-k+q\downarrow}$ ,  $p_k h_k$  and  $(1-f_{-k+q\downarrow})(1-f_{k+q\uparrow})(1-h_k)$ , respectively. Similar to (3.16) in reference [20], the total free energy of a superconductor in the superconducting state can then be expressed as:

$$\begin{aligned} F_s = & \sum_{k > k_F} \varepsilon_{-k+q} [s_{-k+q\downarrow} + p_k(1 - h_k) + (1 - f_{-k+q\downarrow})(1 - f_{k+q\uparrow})h_k] + \\ & \sum_{k < k_F} (-\varepsilon_{-k+q}) [s_{-k+q\downarrow} + p_k h_k + (1 - f_{-k+q\downarrow})(1 - f_{k+q\uparrow})(1 - h_k)] + \\ & \sum_{k > k_F} \varepsilon_{k+q} [s_{k+q\uparrow} + p_k(1 - h_k) + (1 - f_{-k+q\downarrow})(1 - f_{k+q\uparrow})h_k] + \end{aligned}$$

$$\begin{aligned}
& \sum_{k < k_F} (-\varepsilon_{k+q}) [S_{k+q\uparrow} + p_k h_k + (1 - f_{-k+q})(1 - f_{k+q\uparrow})(1 - h_k)] - \sum_{k, k'} V [h_k (1 - \\
& h_k) h_{k'} (1 - h_{k'})]^{1/2} (1 - f_{-k+q\downarrow} - f_{k+q\uparrow})(1 - f_{-k'+q\downarrow} - f_{k'+q\uparrow}) + \\
& kT \sum_k [f_{-k+q\downarrow} \ln f_{-k+q\downarrow} + (1 - f_{-k+q\downarrow}) \ln(1 - f_{-k+q\downarrow}) + f_{k+q\uparrow} \ln f_{k+q\uparrow} + \\
& (1 - f_{k+q\uparrow}) \ln(1 - f_{k+q\uparrow})] \tag{10}
\end{aligned}$$

Applying (6)(7)(8)(9) into (10), by minimizing  $F_s$  with respect to  $h_k$  and  $f_{k+q\downarrow}$ , separately, we have,

$$\frac{\sqrt{h_k(1-h_k)}}{1-2h_k} = \frac{\sum_{k'} V [h_{k'}(1-h_{k'})]^{1/2} (1-f_{-k'+q\downarrow}-f_{k'+q\uparrow})}{\varepsilon_{-k+q} + \varepsilon_{k+q}} \tag{11}$$

$$h_k = \frac{1}{2} \left( 1 - \frac{\varepsilon_k + \varepsilon_s}{E_k} \right) \tag{12}$$

$$[h_k(1-h_k)]^{1/2} = \frac{\Delta}{2E_k} \tag{13}$$

$$f_{-k+q\downarrow} = \begin{cases} f(E_{-k+q\downarrow}), & k > k_F \\ f(E_{k+q\uparrow}), & k < k_F \end{cases} \tag{14}$$

$$f_{k+q\uparrow} = \begin{cases} f(E_{k+q\uparrow}), & k > k_F \\ f(E_{-k+q\downarrow}), & k < k_F \end{cases} \tag{15}$$

with  $\beta = \frac{1}{kT}$  and

$$\Delta = \sum_{k'} V [h_{k'}(1-h_{k'})]^{1/2} (1 - f_{-k'+q\downarrow} - f_{k'+q\uparrow}) \tag{16}$$

$$E_{k+q\uparrow} = E_k + \varepsilon_{ext}, E_{-k+q\downarrow} = E_k - \varepsilon_{ext} \tag{17}$$

$$f(E) = \frac{1}{e^{\beta E} + 1} \tag{18}$$

$$\text{and } E_k = [(\varepsilon_k + \varepsilon_s)^2 + \Delta^2]^{1/2} \tag{19}$$

The excited particle distribution functions  $f_{\mathbf{k}+\mathbf{q}\downarrow}$  and  $f_{\mathbf{k}+\mathbf{q}\uparrow}$  are not continuous at  $\mathbf{k} = \mathbf{k}_F$  since they specify electron occupations above Fermi surface and hole occupations below it. The probability that  $-\mathbf{k}+\mathbf{q}\downarrow$  is occupied by an electron and  $\mathbf{k}+\mathbf{q}\uparrow$  is empty, is continuous at  $\mathbf{k} = \mathbf{k}_F$ , with a value at  $f(E_{-\mathbf{k}+\mathbf{q}\downarrow})[1-f(E_{\mathbf{k}+\mathbf{q}\uparrow})]$ .

These results are similar to the results in reference [24] using a different approach, with the expression of  $E_k$  slightly different.

The functions that describe the probability of quasi-particle (single or excited pair of electrons/holes) distribution and the modified density of states are,

$$\frac{1}{2} \int_{-1}^1 f_{-\mathbf{k}+\mathbf{q}\downarrow} dx = \frac{1}{2} \int_{-1}^1 f_{\mathbf{k}+\mathbf{q}\uparrow} dx = 1 + \frac{1}{2\beta p_F v_s} \ln \left( \frac{1+e^{\beta(E_{\mathbf{k}}-p_F v_s)}}}{1+e^{\beta(E_{\mathbf{k}}+p_F v_s)}} \right) \quad (20)$$

$$\frac{1}{2} \int_{-1}^1 \frac{d\varepsilon}{dE_{\mathbf{k}+\mathbf{q}\uparrow}} dx = \frac{1}{2} \int_{-1}^1 \frac{d\varepsilon}{dE_{-\mathbf{k}+\mathbf{q}\downarrow}} dx = \begin{cases} \frac{\sqrt{(E_a+p_F v_s)^2-\Delta^2}-\sqrt{(E_a-p_F v_s)^2-\Delta^2}}{2p_F v_s}, & E_a > \Delta + p_F v_s \\ \frac{\sqrt{(E_a+p_F v_s)^2-\Delta^2}}{2p_F v_s}, & \Delta + p_F v_s > E_a > \Delta - p_F v_s \\ 0, & E_a < \Delta - p_F v_s \end{cases} \quad (21)$$

Equation (21), with  $E_a = E_{\mathbf{k}+\mathbf{q}\uparrow}$  or  $E_a = E_{-\mathbf{k}+\mathbf{q}\downarrow}$ , is the same as the corresponding equation in reference [25]. Equation (19) shows  $2\Delta$  energy, which represents the energy gap of this superconducting system, is still necessary for a photon to break a Cooper pair, while the quasi-particles could exist within the  $2\Delta$  regime nearby Fermi surface. The minimum gap in energy spectrum for quasi-particles in this superconductor reduces to  $2(\Delta-p_F v_s)$ , as shown in equations (20) and (21).

The energy gap, as a function of Cooper pair velocity, may be derived by applying (12)(13)(14)(15)(17)(18)(19) into (16) and changing the sum into integration,



$$\frac{1}{NV} = \int_{-1}^1 \frac{dx}{2} \int_{-\hbar\omega_D}^{\hbar\omega_D} \frac{d\varepsilon_k}{2[(\varepsilon_k + \varepsilon_s)^2 + \Delta^2]^{1/2}} \left( 1 - \frac{1}{e^{\beta\left\{[(\varepsilon_k + \varepsilon_s)^2 + \Delta^2]^{1/2} - \varepsilon_{ext}\right\} + 1}} - \frac{1}{e^{\beta\left\{[(\varepsilon_k + \varepsilon_s)^2 + \Delta^2]^{1/2} + \varepsilon_{ext}\right\} + 1}} \right) \quad (22)$$

This expression is the same as B7 in reference [24].

The critical temperature may be calculated with  $\Delta = 0$  in (22),

$$\frac{1}{NV} = \int_{-1}^1 \frac{dx}{2} \int_{-\hbar\omega_D}^{\hbar\omega_D} \frac{d\varepsilon_k}{2|\varepsilon_k + \varepsilon_s|} \left( 1 - \frac{1}{e^{\frac{|\varepsilon_k + \varepsilon_s| - \varepsilon_{ext}}{kT_c} + 1}} - \frac{1}{e^{\frac{|\varepsilon_k + \varepsilon_s| + \varepsilon_{ext}}{kT_c} + 1}} \right) \quad (23)$$

For Nb with  $\Delta_0/kT_c(0) = 1.85$ ,  $T_c(0) = 9.25$  K and  $\xi_0 = 40$  nm [26], with  $T_c(0)$  the critical temperature for  $v_s = 0$  m/s and  $\xi_0$  the coherence length for  $v_s = 0$  m/s at 0 K temperature, the numerical solution of  $\Delta$  and  $T_c$  at 2 K have been plotted in Figure 2.2. The calculation stopped at the critical velocity, which is determined by the critical current, from where Cooper pairs start to break. The corresponding magnetic flux density is also labeled with  $\lambda_L(0) = 32$  nm and above  $\xi_0$  value.

In order to calculate the SRF BCS surface impedance, one may start with the matrix elements of a single-particle scattering operator in references [20, 21], using the new particle distribution equations (12)-(19).

Here we list the matrix elements in Table 2.1. The first type of transition, labeled as (a) in Table 2.1, corresponds to single occupancy of  $\mathbf{k}$  in the initial and of  $\mathbf{k}'$  in the final state. The other types shown in reference [20] can be listed in a similar way.

Using the first row of Table 2.1 as an example, in the initial state,  $\mathbf{k}+\mathbf{q}\uparrow$  is occupied, noted as X,  $-\mathbf{k}+\mathbf{q}\downarrow$ ,  $\mathbf{k}'+\mathbf{q}\uparrow$  and  $-\mathbf{k}'+\mathbf{q}\downarrow$  are unoccupied, noted as 0. In the final state, only  $\mathbf{k}'+\mathbf{q}\uparrow$  is occupied. Pair occupancy of  $(\mathbf{k}'+\mathbf{q}\uparrow, -\mathbf{k}'+\mathbf{q}\downarrow)$  in initial state and of  $(\mathbf{k}+\mathbf{q}\uparrow, -\mathbf{k}+\mathbf{q}\downarrow)$  in final state may be either ground (+) or excited (-), listed in the second column. For  $\mathbf{k}+\mathbf{q}\uparrow$  single occupancy in initial state with both states ground, the initial energy is  $E_{\mathbf{k}+\mathbf{q}\uparrow}$ . For  $\mathbf{k}'+\mathbf{q}\uparrow$  single occupancy in final state with both states ground, the final energy is  $E_{\mathbf{k}'+\mathbf{q}\uparrow}$ . The energy difference between them is listed in column 3. The probability of initial state  $(\mathbf{k}+\mathbf{q}\uparrow, -\mathbf{k}+\mathbf{q}\downarrow)$  to be X0 is  $s_{\mathbf{k}+\mathbf{q}\uparrow}$  and the probability of initial state  $(\mathbf{k}'+\mathbf{q}\uparrow, -\mathbf{k}'+\mathbf{q}\downarrow)$  to be 00 is  $(1-s_{-\mathbf{k}'+\mathbf{q}\downarrow}-s_{\mathbf{k}'+\mathbf{q}\uparrow}-p')$ , the combination of these two probabilities is listed in column 4. Column 5 lists the matrix elements that are the same as Table II in reference [20]. In this column,  $h$  and  $h'$  are used to simplify the expression of  $h_{\mathbf{k}}$  and  $h_{\mathbf{k}'}$ , respectively. One may refer to references [20, 21] for more detail about this table.

While under RF field with angular frequency  $\omega$ , the photon energy  $\hbar(\omega-is)$  should be inserted into either the initial or the final state in Table 2.1. Here a small positive parameter  $s$ , which will be set equal to zero in the final expression, has been introduced to obtain the real and imaginary part of surface resistance [21]. Based on above analysis and the summary in Table 2.2, the single-particle scattering operator, shown as equation (3.2) in reference [21] could be rewritten into,

$$L(\omega, \varepsilon, \varepsilon', x, x') = \frac{1}{4} \left( 1 + \frac{(\varepsilon + \varepsilon_s)(\varepsilon' + \varepsilon_s) + \Delta^2}{E_{\mathbf{k}} E_{\mathbf{k}'}} \right) \left( \frac{1}{E_{\mathbf{k}+\mathbf{q}\uparrow} - E_{\mathbf{k}'+\mathbf{q}\uparrow} + \hbar(\omega - is)} + \frac{1}{E_{\mathbf{k}+\mathbf{q}\uparrow} - E_{\mathbf{k}'+\mathbf{q}\uparrow} - \hbar(\omega - is)} \right) (f_{\mathbf{k}'+\mathbf{q}\uparrow} -$$

$$f_{k+q\uparrow}) + \frac{1}{4} \left( 1 - \frac{(\varepsilon + \varepsilon_s)(\varepsilon' + \varepsilon_s) + \Delta^2}{E_k E_{k'}} \right) \left( \frac{1}{E_{k+q\uparrow} + E_{k'+q\uparrow} + \hbar(\omega - is)} + \frac{1}{E_{k+q\uparrow} + E_{k'+q\uparrow} - \hbar(\omega - is)} \right) (1 - f_{k'+q\uparrow} - f_{k+q\uparrow}) \quad (24)$$

with  $x$  (or  $x'$ ) being cosine of the angle between  $\mathbf{v}_k$  (or  $\mathbf{v}_{k'}$ ) and  $\mathbf{v}_s$ , consider the integration from -1 to 1 for  $x$  and  $x'$ , equation (2) now becomes,

$$K(p) = \frac{-3}{4\pi\hbar v_F \lambda_L^2(0)} \int_0^\infty \frac{4}{(pR)^2} \left[ \frac{\sin(pR)}{pR} - \cos(pR) \right] e^{-\frac{R}{l}} \times \frac{1}{4} \int_{-1}^1 \int_{-1}^1 I(\omega, R, T, x, x') dx dx' dR \quad (25)$$

with  $l$  the mean free path and

$$I(\omega, R, T, x, x') = \int_{-\infty}^\infty \int_{-\infty}^\infty \left[ L(\omega, \varepsilon, \varepsilon', x, x') + \frac{1-2f(\varepsilon)}{\varepsilon' - \varepsilon} \right] \times \cos[\alpha(\varepsilon - \varepsilon')] d\varepsilon' d\varepsilon \quad (26)$$

$$\text{with } \alpha = \frac{R}{\hbar p_F}.$$

Expression (24) can be rearranged as,

$$L(\omega, \varepsilon, \varepsilon', x, x') = -\frac{1}{2} (1 - f(E_{k+q\uparrow}) - f(E_{-k+q\downarrow})) \left\{ \frac{E_{k+q\uparrow} + \hbar(\omega - is) - \varepsilon_{ext}' + \frac{(\varepsilon + \varepsilon_s)(\varepsilon' + \varepsilon_s) + \Delta^2}{E}}{E_k'^2 - [E_{k+q\uparrow} - \varepsilon_{ext}' + \hbar(\omega - is)]^2} + \frac{E_{k+q\uparrow} - \hbar(\omega - is) - \varepsilon_{ext}' + \frac{(\varepsilon + \varepsilon_s)(\varepsilon' + \varepsilon_s) + \Delta^2}{E}}{E_k'^2 - [E_{k+q\uparrow} - \varepsilon_{ext}' - \hbar(\omega - is)]^2} \right\} \quad (27)$$

And thus expression (26) in the limit  $s \rightarrow 0$  is,

$$I(\omega, R, T, x, x') = -\pi i \int_{\Delta - \varepsilon_{ext}'}^{\infty} [1 - f(E_2 + \varepsilon_{ext}) - f(E_2 - \varepsilon_{ext})] \{g \cos[\alpha(\varepsilon_2 + \varepsilon_s)] - i \sin[\alpha(\varepsilon_2 + \varepsilon_s)]\} e^{i\alpha(\varepsilon_1 + \varepsilon_s)} dE + \pi i \int_{\Delta - \varepsilon_{ext}}^{\infty} [1 - f(E_1 + \varepsilon_{ext}) - f(E_1 - \varepsilon_{ext})] \{g \cos[\alpha(\varepsilon_1 + \varepsilon_s)] + i \sin[\alpha(\varepsilon_1 + \varepsilon_s)]\} e^{-i\alpha(\varepsilon_2 + \varepsilon_s)} dE \quad (28)$$

with  $E_1 = E + \varepsilon_{ext}$ ,  $E_2 = E + \varepsilon_{ext}' + \hbar\omega$

$$\varepsilon_1 = \sqrt{E_1^2 - \Delta^2} - \varepsilon_s, \varepsilon_2 = \sqrt{E_2^2 - \Delta^2} - \varepsilon_s$$

$$g = \frac{E_1 E_2 + \Delta^2}{(\varepsilon_1 + \varepsilon_s)(\varepsilon_2 + \varepsilon_s)} \text{ and } \alpha = \frac{R}{\hbar v_F}.$$

Appendix A and Appendix B show the mathematical derivation of (27) and (28).

When the Cooper pair net velocity  $v_s \rightarrow 0$ , (28) reduces to equation (3.5) in reference [21].

One should notice  $\varepsilon_1$ ,  $\varepsilon_2$  and  $g$  are not always real in (28). The following expressions have been used to separate equation (28) into real part and imaginary part,

$$Re[K(p)] = \frac{3}{4r\hbar v_F \lambda_L^2(0)} \int_{-1}^1 \int_{-1}^1 M(p, x, x') dx dx'$$

$$Im[K(p)] = \frac{3}{4r\hbar v_F \lambda_L^2(0)} \int_{-1}^1 \int_{-1}^1 N(p, x, x') dx dx' \quad (29)$$

with

$$M(p, x, x') = \frac{1}{2} \int_{\Delta - \varepsilon_{ext}}^{\infty} \{ [f(E_2 + \varepsilon_{ext}) + f(E_2 - \varepsilon_{ext}) - f(E_1 + \varepsilon_{ext}) - f(E_1 - \varepsilon_{ext})] (g + 1) S(a_-, a_3) - [2 - f(E_2 + \varepsilon_{ext}) - f(E_2 - \varepsilon_{ext}) - f(E_1 + \varepsilon_{ext}) - f(E_1 - \varepsilon_{ext})] (g - 1) S(a_+, a_3) \} dE + \int_{\Delta - \varepsilon_{ext}' - \hbar\omega}^{\Delta - \varepsilon_{ext}} [1 - f(E_2 + \varepsilon_{ext}) - f(E_2 - \varepsilon_{ext})] [g_{1b} R(a_2, a_3 + a_{1b}) + S(a_2, a_3 + a_{1b})] dE$$

$$N(p, x, x') = -\frac{1}{2} \int_{\Delta - \varepsilon_{ext}}^{\infty} [f(E_2 + \varepsilon_{ext}) + f(E_2 - \varepsilon_{ext}) - f(E_1 + \varepsilon_{ext}) - f(E_1 - \varepsilon_{ext})] [(g - 1) R(a_+, a_3) + (g + 1) R(a_-, a_3)] dE$$

while  $\varepsilon_{ext} < \varepsilon'_{ext} + \hbar\omega$  and,

$$M(p, x, x') = \frac{1}{2} \int_{\Delta - \varepsilon_{ext}' - \hbar\omega}^{\infty} \{ [f(E_2 + \varepsilon_{ext}) + f(E_2 - \varepsilon_{ext}) - f(E_1 + \varepsilon_{ext}) - f(E_1 - \varepsilon_{ext})] (g + 1) S(a_-, a_3) - [2 - f(E_2 + \varepsilon_{ext}) - f(E_2 - \varepsilon_{ext}) - f(E_1 + \varepsilon_{ext}) - f(E_1 - \varepsilon_{ext})] (g - 1) S(a_+, a_3) \} dE + \int_{\Delta - \varepsilon_{ext}' - \hbar\omega}^{\Delta - \varepsilon_{ext}} [1 - f(E_2 + \varepsilon_{ext}) - f(E_2 - \varepsilon_{ext})] [g_{1b} R(a_2, a_3 + a_{1b}) + S(a_2, a_3 + a_{1b})] dE$$

$$\begin{aligned}
& \varepsilon_{ext}) - f(E_1 - \varepsilon_{ext})](g - 1)S(a_+, a_3)\}dE + \int_{\Delta - \varepsilon_{ext}}^{\Delta - \varepsilon_{ext}' - \hbar\omega} [1 - f(E_1 + \varepsilon_{ext}) - \\
& f(E_1 - \varepsilon_{ext})][g_{2b}R(a_1, a_3 + a_{2b}) + S(a_1, a_3 + a_{2b})]dE \\
N(p, x, x') = & -\frac{1}{2} \int_{\Delta - \varepsilon_{ext}' - \hbar\omega}^{\infty} [f(E_2 + \varepsilon_{ext}) + f(E_2 - \varepsilon_{ext}) - f(E_1 + \varepsilon_{ext}) - \\
& f(E_1 - \varepsilon_{ext})][(g - 1)R(a_+, a_3) + (g + 1)R(a_-, a_3)]dE \tag{30}
\end{aligned}$$

while  $\varepsilon_{ext} > \varepsilon'_{ext} + \hbar\omega$ ,

$$\text{and } \varepsilon_{1b} = \sqrt{\Delta^2 - E_1^2} - \varepsilon_s, \varepsilon_{2b} = \sqrt{\Delta^2 - E_2^2} - \varepsilon_s$$

$$g_{1b} = \frac{E_1 E_2 + \Delta^2}{(\varepsilon_{1b} + \varepsilon_s)(\varepsilon_2 + \varepsilon_s)}, g_{2b} = \frac{E_1 E_2 + \Delta^2}{(\varepsilon_1 + \varepsilon_s)(\varepsilon_{2b} + \varepsilon_s)}$$

$$a_1 = \frac{\varepsilon_1 + \varepsilon_s}{\hbar v_F}, a_2 = \frac{\varepsilon_2 + \varepsilon_s}{\hbar v_F}, a_3 = \frac{1}{pl}, a_{ext} = \frac{\varepsilon_{ext} - \varepsilon_{ext}'}{\hbar v_F},$$

$$a_{1b} = \frac{\varepsilon_{1b} + \varepsilon_s}{\hbar v_F}, a_{2b} = \frac{\varepsilon_{2b} + \varepsilon_s}{\hbar v_F}, a_+ = a_1 + a_2, a_- = a_1 - a_2$$

$$R(a, b) = -\frac{b}{2} + \frac{ab}{4} \ln \frac{b^2 + (1+a)^2}{b^2 + (1-a)^2} + \frac{1+b^2-a^2}{4} \arctan \frac{2b}{b^2 + a^2 - 1}$$

$$S(a, b) = \frac{a}{2} - \frac{ab}{2} \arctan \frac{2b}{b^2 + a^2 - 1} + \frac{1+b^2-a^2}{8} \ln \frac{b^2 + (1+a)^2}{b^2 + (1-a)^2}$$

Here all the elements in  $M(p, x, x')$  and  $N(p, x, x')$  are real. One now obtains an analytical expression for the surface impedance by incorporating (29)(30) into (3).

The quadruple integral must be solved numerically.

The above analysis is valid to any conventional superconductor. A Mathematica<sup>TM</sup> program, shown in Appendix C, has been developed to calculate this integral. The results are shown in Figure 2.3, using parameters for Nb with  $\Delta_0/kT_c(0) = 1.85$ ,  $T_c(0) = 9.25$  K,  $\xi_0 = 40$  nm,  $\lambda_L(0) = 32$  nm,  $\iota = 40$  nm at 1.5 GHz and 2 K [26].  $\iota$  is the mean free path. The surface resistance and reactance value of the outmost layer of the superconductor are labeled.

The surface resistance  $R_s$ , with a value of 10.9 n $\Omega$  at 0 m/s Cooper pair velocity  $v_s$ , first decreases with increasing  $v_s$ , then increases with increasing  $v_s$ , with a minimum  $R_s$  of 2.04 n $\Omega$  at 200 m/s  $v_s$ .

Qualitative insight into the change in  $R_s$  may be obtained by considering the extreme anomalous limit approximation with  $\alpha \rightarrow 0$  [19, 21]. In this approximation equation (28) becomes,

$$K(p) = \frac{3}{4q\hbar v_F \lambda_L^2(0)} \frac{1}{4} \int_{-1}^1 \int_{-1}^1 \left\{ -\pi i \int_{\Delta - \varepsilon_{ext}' - \hbar\omega}^{\infty} [1 - f(E_2 + \varepsilon_{ext}) - f(E_2 - \varepsilon_{ext})] g dE + \pi i \int_{\Delta - \varepsilon_{ext}}^{\infty} [1 - f(E_1 + \varepsilon_{ext}) - f(E_1 - \varepsilon_{ext})] g dE \right\} dx dx' \quad (31)$$

Based on (31), the energy loss is determined by the integration over energy and angles of the expression  $[f(E_2 + \varepsilon_{ext}) + f(E_2 - \varepsilon_{ext}) - f(E_1 + \varepsilon_{ext}) - f(E_1 - \varepsilon_{ext})] g$ . With the assumption  $E \gg kT$ , the excited particle distribution function changes to  $f(E) = 1/e^{\beta E}$ . The above expression then becomes  $[f(E_2) - f(E_1)][f(\varepsilon_{ext}) + f(-\varepsilon_{ext})] g$ . The scattering between energy level  $E_1$  and  $E_2$ , shown in the first term  $[f(E_2) - f(E_1)]$ , is zero at  $\varepsilon_{ext} = \varepsilon_{ext}' + \hbar\omega$ . The contribution from  $\varepsilon_{ext} < \varepsilon_{ext}' + \hbar\omega$  is partly cancelled by the contribution from  $\varepsilon_{ext} > \varepsilon_{ext}' + \hbar\omega$ . The low field  $R_s$  reduction is caused by the non-symmetric cancellation effect brought by the Cooper pair velocity. The second term,  $[f(\varepsilon_{ext}) + f(-\varepsilon_{ext})]$ , which is considered as equation (3) in reference [23], combining with the reduction of energy gap, gives an increase in  $R_s$  with increasing  $v_s$ .

To obtain the effective surface impedance under RF field  $H$ ,  $Z(v_s)$  should be averaged over the RF period and the depth in the superconductor, as (5) and (6) in [23].

The electron states distribution at 0K and the probability of electron occupation with finite temperature have been calculated based on BCS theory and considering Cooper pairs to be moving coherently. These new expressions have been applied to Nb, the material of greatest interest to SRF applications, to construct the analytical value of its surface impedance. With the parameters given above, the result shows a minimum surface resistance at 200 m/s cooper pair velocity, corresponding to 40 mT magnetic flux density. In the above analysis, local effects, non-equilibrium status and thermal feedback are not included, which will of course give additional contributions to the effective surface resistance of resonant SRF structures.

Table 2.1. Matrix elements of single particle scattering operator with moving cooper pairs, compared to BCS theory table II.

Wave functions				Ground(+) or excited(-)		Energy difference $W_i - W_f$	Probability of initial state	Matrix elements	
Initial, $\psi_i$		Final, $\psi_f$		(+)	(-)			$c_{k\uparrow}^* c_{k\downarrow}$ OR $c_{-k\downarrow}^* c_{k\uparrow}$	$c_{-k\downarrow}^* c_{-k\uparrow}$ OR $c_{k\uparrow}^* c_{k\downarrow}$
$(k+q\uparrow, -k+q\downarrow)$	$(k'+q\uparrow, -k'+q\downarrow)$	$(k+q\uparrow, -k+q\downarrow)$	$(k'+q\uparrow, -k'+q\downarrow)$	$(k+q\uparrow, -k+q\downarrow)$	$(k'+q\uparrow, -k'+q\downarrow)$				
(a)									
X0	00	00	X0	+	+	$E_{k+q\uparrow} - E_{k'+q\uparrow}$	$s_{k+q\uparrow}(1-s_{-k'+q\downarrow}-s_{k'+q\uparrow}-p')$	$[(1-h)(1-h')]^{1/2}$	$-(hh')^{1/2}$
X0	XX	XX	X0	-	-	$-E_{-k+q\downarrow} + E_{-k'+q\downarrow}$	$s_{k+q\downarrow}p'$	$(hh')^{1/2}$	$-[(1-h)(1-h')]^{1/2}$
X0	XX	XX	X0	+	-	$E_{k+q\uparrow} + E_{-k'+q\downarrow}$	$s_{k+q\downarrow}p'$	$-[(1-h)h']^{1/2}$	$-[h(1-h')]^{1/2}$
X0	XX	XX	X0	-	+	$-(E_{-k+q\downarrow} + E_{k'+q\uparrow})$	$s_{k+q\uparrow}(1-s_{-k'+q\downarrow}-s_{k'+q\uparrow}-p')$	$-[h(1-h')]^{1/2}$	$-[(1-h)h']^{1/2}$
X0	00	00	0X	+	+	$E_{k+q\uparrow} - E_{k'+q\uparrow}$	$s_{k+q\uparrow}(1-s_{-k'+q\downarrow}-s_{k'+q\uparrow}-p')$	$[(1-h)(1-h')]^{1/2}$	$-(hh')^{1/2}$
X0	XX	XX	0X	-	-	$-E_{-k+q\downarrow} + E_{k'+q\uparrow}$	$s_{k+q\downarrow}p'$	$(hh')^{1/2}$	$-[(1-h)(1-h')]^{1/2}$
X0	XX	XX	0X	+	-	$E_{k+q\uparrow} + E_{k'+q\uparrow}$	$s_{k+q\downarrow}p'$	$-[(1-h)h']^{1/2}$	$-[h(1-h')]^{1/2}$
X0	XX	XX	0X	-	+	$-(E_{-k+q\downarrow} + E_{k'+q\uparrow})$	$s_{k+q\uparrow}(1-s_{-k'+q\downarrow}-s_{k'+q\uparrow}-p')$	$-[h(1-h')]^{1/2}$	$-[(1-h)h']^{1/2}$
0X	00	00	X0	+	+	$E_{-k+q\downarrow} - E_{k'+q\uparrow}$	$s_{-k+q\downarrow}(1-s_{k'+q\uparrow}-s_{k'+q\uparrow}-p')$	$[(1-h)(1-h')]^{1/2}$	$-(hh')^{1/2}$
0X	XX	XX	X0	-	-	$-E_{k+q\uparrow} + E_{-k'+q\downarrow}$	$s_{-k+q\downarrow}p'$	$(hh')^{1/2}$	$-[(1-h)(1-h')]^{1/2}$
0X	XX	XX	X0	+	-	$E_{-k+q\downarrow} + E_{-k'+q\downarrow}$	$s_{-k+q\downarrow}p'$	$-[(1-h)h']^{1/2}$	$-[h(1-h')]^{1/2}$
0X	XX	XX	X0	-	+	$-(E_{k+q\uparrow} + E_{k'+q\uparrow})$	$s_{-k+q\downarrow}(1-s_{k'+q\uparrow}-s_{k'+q\uparrow}-p')$	$-[h(1-h')]^{1/2}$	$-[(1-h)h']^{1/2}$
0X	00	00	0X	+	+	$E_{-k+q\downarrow} - E_{k'+q\uparrow}$	$s_{-k+q\downarrow}(1-s_{k'+q\uparrow}-s_{k'+q\uparrow}-p')$	$[(1-h)(1-h')]^{1/2}$	$-(hh')^{1/2}$
0X	XX	XX	0X	-	-	$-E_{k+q\uparrow} + E_{k'+q\uparrow}$	$s_{-k+q\downarrow}p'$	$(hh')^{1/2}$	$-[(1-h)(1-h')]^{1/2}$
0X	XX	XX	0X	+	-	$E_{-k+q\downarrow} + E_{k'+q\uparrow}$	$s_{-k+q\downarrow}p'$	$-[(1-h)h']^{1/2}$	$-[h(1-h')]^{1/2}$
0X	XX	XX	0X	-	+	$-(E_{k+q\uparrow} + E_{k'+q\uparrow})$	$s_{-k+q\downarrow}(1-s_{k'+q\uparrow}-s_{k'+q\uparrow}-p')$	$-[h(1-h')]^{1/2}$	$-[(1-h)h']^{1/2}$
(b)									
XX	0X	0X	XX	+	+	$-E_{-k+q\downarrow} + E_{-k'+q\downarrow}$	$(1-s_{-k+q\downarrow}-s_{k'+q\uparrow}-p)s_{k'+q\uparrow}$	$(hh')^{1/2}$	$-[(1-h)(1-h')]^{1/2}$
00	0X	0X	00	-	-	$E_{k+q\uparrow} - E_{k'+q\uparrow}$	$ps_{-k'+q\downarrow}$	$[(1-h)(1-h')]^{1/2}$	$-(hh')^{1/2}$
00	0X	0X	00	+	-	$-(E_{-k+q\downarrow} + E_{k'+q\uparrow})$	$(1-s_{-k+q\downarrow}-s_{k'+q\uparrow}-p)s_{k'+q\uparrow}$	$[h(1-h')]^{1/2}$	$[(1-h)h']^{1/2}$
00	0X	0X	00	-	+	$E_{k+q\uparrow} + E_{-k'+q\downarrow}$	$ps_{-k'+q\downarrow}$	$[(1-h)h']^{1/2}$	$[h(1-h')]^{1/2}$
XX	0X	X0	XX	+	+	$-E_{k+q\uparrow} + E_{-k'+q\downarrow}$	$(1-s_{-k+q\downarrow}-s_{k'+q\uparrow}-p)s_{k'+q\uparrow}$	$(hh')^{1/2}$	$-[(1-h)(1-h')]^{1/2}$
00	0X	X0	00	-	-	$E_{-k+q\downarrow} - E_{k'+q\uparrow}$	$ps_{k'+q\uparrow}$	$[(1-h)(1-h')]^{1/2}$	$-(hh')^{1/2}$
00	0X	X0	00	+	-	$-(E_{k+q\uparrow} + E_{k'+q\uparrow})$	$(1-s_{-k+q\downarrow}-s_{k'+q\uparrow}-p)s_{k'+q\uparrow}$	$[h(1-h')]^{1/2}$	$[(1-h)h']^{1/2}$



				-	+	$E_{k+q} + E_{k'+q}$	$pS_{k'+q}$	$[(1-h)h']^{1/2}$	$[h(1-h')]^{1/2}$
XX	X0	0X	XX	+	+	$-E_{k+q} + E_{k'+q}$	$(1-S_{k+q} - S_{k'+q} - p)S_{k'+q}$	$(hh')^{1/2}$	$-[(1-h)(1-h')]^{1/2}$
00	X0	0X	00	-	-	$E_{k+q} - E_{k'+q}$	$pS_{k'+q}$	$[(1-h)(1-h')]^{1/2}$	$-(hh')^{1/2}$
				+	-	$-(E_{k+q} + E_{k'+q})$	$(1-S_{k+q} - S_{k'+q} - p)S_{k'+q}$	$[h(1-h')]^{1/2}$	$[(1-h)h']^{1/2}$
				-	+	$E_{k+q} + E_{k'+q}$	$pS_{k'+q}$	$[(1-h)h']^{1/2}$	$[h(1-h')]^{1/2}$
XX	X0	X0	XX	+	+	$-E_{k+q} + E_{k'+q}$	$(1-S_{k+q} - S_{k'+q} - p)S_{k'+q}$	$(hh')^{1/2}$	$-[(1-h)(1-h')]^{1/2}$
00	X0	X0	00	-	-	$E_{k+q} - E_{k'+q}$	$pS_{k'+q}$	$[(1-h)(1-h')]^{1/2}$	$-(hh')^{1/2}$
				+	-	$-(E_{k+q} + E_{k'+q})$	$(1-S_{k+q} - S_{k'+q} - p)S_{k'+q}$	$[h(1-h')]^{1/2}$	$[(1-h)h']^{1/2}$
				-	+	$E_{k+q} + E_{k'+q}$	$pS_{k'+q}$	$[(1-h)h']^{1/2}$	$[h(1-h')]^{1/2}$
		(c)		+	+	$E_{k+q} + E_{k'+q}$	$S_{k+q} \cdot S_{k'+q}$	$[(1-h)h']^{1/2}$	$[h(1-h')]^{1/2}$
X0	0X	00	XX	-	-	$-(E_{k+q} + E_{k'+q})$	$S_{k+q} \cdot S_{k'+q}$	$-[h(1-h')]^{1/2}$	$-[(1-h)h']^{1/2}$
X0	0X	XX	00	+	-	$E_{k+q} - E_{k'+q}$	$S_{k+q} \cdot S_{k'+q}$	$[(1-h)(1-h')]^{1/2}$	$-(hh')^{1/2}$
				-	+	$-E_{k+q} + E_{k'+q}$	$S_{k+q} \cdot S_{k'+q}$	$-(hh')^{1/2}$	$[(1-h)(1-h')]^{1/2}$
X0	X0	00	XX	+	+	$E_{k+q} + E_{k'+q}$	$S_{k+q} \cdot S_{k'+q}$	$[(1-h)h']^{1/2}$	$[h(1-h')]^{1/2}$
X0	X0	XX	00	-	-	$-(E_{k+q} + E_{k'+q})$	$S_{k+q} \cdot S_{k'+q}$	$-[(1-h)h']^{1/2}$	$-(hh')^{1/2}$
				+	-	$E_{k+q} - E_{k'+q}$	$S_{k+q} \cdot S_{k'+q}$	$-(hh')^{1/2}$	$[(1-h)h']^{1/2}$
				-	+	$-E_{k+q} + E_{k'+q}$	$S_{k+q} \cdot S_{k'+q}$	$[(1-h)(1-h')]^{1/2}$	$[h(1-h')]^{1/2}$
0X	0X	00	XX	+	+	$E_{k+q} + E_{k'+q}$	$S_{k+q} \cdot S_{k'+q}$	$[(1-h)h']^{1/2}$	$[h(1-h')]^{1/2}$
0X	0X	XX	00	-	-	$-(E_{k+q} + E_{k'+q})$	$S_{k+q} \cdot S_{k'+q}$	$-[(1-h)h']^{1/2}$	$-(hh')^{1/2}$
				+	-	$E_{k+q} - E_{k'+q}$	$S_{k+q} \cdot S_{k'+q}$	$-(hh')^{1/2}$	$[(1-h)h']^{1/2}$
				-	+	$-E_{k+q} + E_{k'+q}$	$S_{k+q} \cdot S_{k'+q}$	$[(1-h)(1-h')]^{1/2}$	$[h(1-h')]^{1/2}$
0X	X0	00	XX	+	+	$E_{k+q} + E_{k'+q}$	$S_{k+q} \cdot S_{k'+q}$	$[(1-h)h']^{1/2}$	$[h(1-h')]^{1/2}$
0X	X0	XX	00	-	-	$-(E_{k+q} + E_{k'+q})$	$S_{k+q} \cdot S_{k'+q}$	$-[(1-h)h']^{1/2}$	$-(hh')^{1/2}$
				+	-	$E_{k+q} - E_{k'+q}$	$S_{k+q} \cdot S_{k'+q}$	$-(hh')^{1/2}$	$[(1-h)h']^{1/2}$
				-	+	$-E_{k+q} + E_{k'+q}$	$S_{k+q} \cdot S_{k'+q}$	$[(1-h)(1-h')]^{1/2}$	$[h(1-h')]^{1/2}$
		(d)		+	+	$-(E_{k+q} + E_{k'+q})$	$(1-S_{k+q} - S_{k'+q} - p)(1-S_{k'+q} - S_{k'+q} - p')$	$[h(1-h')]^{1/2}$	$[(1-h)h']^{1/2}$
XX	00	0X	X0	-	-	$E_{k+q} + E_{k'+q}$	$pp'$	$-[(1-h)h']^{1/2}$	$-[h(1-h')]^{1/2}$
00	XX	0X	X0	+	-	$-E_{k+q} + E_{k'+q}$	$(1-S_{k+q} - S_{k'+q} - p)p'$	$-(hh')^{1/2}$	$[(1-h)(1-h')]^{1/2}$
				-	+	$E_{k+q} - E_{k'+q}$	$p(1-S_{k'+q} - S_{k'+q} - p')$	$[(1-h)(1-h')]^{1/2}$	$-(hh')^{1/2}$
				+	+	$-(E_{k+q} + E_{k'+q})$	$(1-S_{k+q} - S_{k'+q} - p)(1-S_{k'+q} - S_{k'+q} - p')$	$[h(1-h')]^{1/2}$	$[(1-h)h']^{1/2}$

XX	00	0X	0X	-	-	$E_{k+q} + E_{k'+q}$	$pp'$	$-[(1-h)h']^{1/2}$	$-[h(1-h')]^{1/2}$
00	XX	0X	0X	+	-	$-E_{k+q} + E_{k'+q}$	$(1-s_{k+q} - s_{k'+q} - p)p'$	$-(hh')^{1/2}$	$[(1-h)(1-h')]^{1/2}$
				-	+	$E_{k+q} - E_{k'+q}$	$p(1-s_{k'+q} - s_{k'+q} - p')$	$[(1-h)(1-h')]^{1/2}$	$-(hh')^{1/2}$
				+	+	$-(E_{k+q} + E_{k'+q})$	$(1-s_{k+q} - s_{k'+q} - p)(1-s_{k'+q} - s_{k'+q} - p')$	$[h(1-h')]^{1/2}$	$[(1-h)h']^{1/2}$
XX	00	X0	X0	-	-	$E_{k+q} + E_{k'+q}$	$pp'$	$-[(1-h)h']^{1/2}$	$-[h(1-h')]^{1/2}$
00	XX	X0	X0	+	-	$-E_{k+q} + E_{k'+q}$	$(1-s_{k+q} - s_{k'+q} - p)p'$	$-(hh')^{1/2}$	$[(1-h)(1-h')]^{1/2}$
				-	+	$E_{k+q} - E_{k'+q}$	$p(1-s_{k'+q} - s_{k'+q} - p')$	$[(1-h)(1-h')]^{1/2}$	$-(hh')^{1/2}$
				+	+	$-(E_{k+q} + E_{k'+q})$	$(1-s_{k+q} - s_{k'+q} - p)(1-s_{k'+q} - s_{k'+q} - p')$	$[h(1-h')]^{1/2}$	$[(1-h)h']^{1/2}$
XX	00	X0	0X	-	-	$E_{k+q} + E_{k'+q}$	$pp'$	$-[(1-h)h']^{1/2}$	$-[h(1-h')]^{1/2}$
00	XX	X0	0X	+	-	$-E_{k+q} + E_{k'+q}$	$(1-s_{k+q} - s_{k'+q} - p)p'$	$-(hh')^{1/2}$	$[(1-h)(1-h')]^{1/2}$
				-	+	$E_{k+q} - E_{k'+q}$	$p(1-s_{k'+q} - s_{k'+q} - p')$	$[(1-h)(1-h')]^{1/2}$	$-(hh')^{1/2}$

Table 2.2. Mean square matrix elements for possible values of  $W_i$ - $W_j$ , compared to BCS theory table III.

$W_i$ - $W_j$	$E_{k+q^-} - E_{k'+q^-}$	$E_{k+q^+} - E_{k'+q^+}$	$E_{k+q^-} - E_{k'+q^-}$	$E_{k+q^+} - E_{k'+q^+}$
$\langle  (\psi_f   c_{k'\uparrow}^* c_{k\uparrow} \pm c_{k\downarrow}^* c_{k'\downarrow}   \psi_f)  ^2 \rangle_{Av}$	$\frac{1}{2} \left( 1 + \frac{(\varepsilon + \varepsilon_s)(\varepsilon' + \varepsilon_s) \mp \Delta^2}{EE'} \right) \times$ $f_{k+q\uparrow}(1 - f_{k'+q\uparrow})$	$\frac{1}{2} \left( 1 + \frac{(\varepsilon + \varepsilon_s)(\varepsilon' + \varepsilon_s) \mp \Delta^2}{EE'} \right) \times$ $f_{k+q\uparrow}(1 - f_{k'+q\downarrow})$	$\frac{1}{2} \left( 1 + \frac{(\varepsilon + \varepsilon_s)(\varepsilon' + \varepsilon_s) \mp \Delta^2}{EE'} \right) \times$ $f_{-k+q\downarrow}(1 - f_{k'+q\uparrow})$	$\frac{1}{2} \left( 1 + \frac{(\varepsilon + \varepsilon_s)(\varepsilon' + \varepsilon_s) \mp \Delta^2}{EE'} \right) \times$ $f_{-k+q\downarrow}(1 - f_{k'+q\downarrow})$
$W_i$ - $W_j$	$E_{k+q^+} - E_{k+q^+}$	$E_{k'+q^-} - E_{k'+q^-}$	$E_{k'+q^+} - E_{k'+q^+}$	$E_{k'+q^-} - E_{k'+q^-}$
$\langle  (\psi_f   c_{k'\uparrow}^* c_{k\uparrow} \pm c_{k\downarrow}^* c_{k'\downarrow}   \psi_f)  ^2 \rangle_{Av}$	$\frac{1}{2} \left( 1 + \frac{(\varepsilon + \varepsilon_s)(\varepsilon' + \varepsilon_s) \mp \Delta^2}{EE'} \right) \times$ $(1 - f_{k+q\uparrow})f_{k'+q\uparrow}$	$\frac{1}{2} \left( 1 + \frac{(\varepsilon + \varepsilon_s)(\varepsilon' + \varepsilon_s) \mp \Delta^2}{EE'} \right) \times$ $(1 - f_{-k+q\downarrow})f_{k'+q\uparrow}$	$\frac{1}{2} \left( 1 + \frac{(\varepsilon + \varepsilon_s)(\varepsilon' + \varepsilon_s) \mp \Delta^2}{EE'} \right) \times$ $(1 - f_{k+q\uparrow})f_{-k'+q\downarrow}$	$\frac{1}{2} \left( 1 + \frac{(\varepsilon + \varepsilon_s)(\varepsilon' + \varepsilon_s) \mp \Delta^2}{EE'} \right) \times$ $(1 - f_{-k+q\downarrow})f_{-k'+q\downarrow}$
$W_i$ - $W_j$	$-(E_{k+q^+} + E_{k'+q^+})$	$-(E_{k+q^+} + E_{k'+q\downarrow})$	$-(E_{k+q^+} + E_{k'+q^+})$	$-(E_{k+q^+} + E_{k'+q^+})$
$\langle  (\psi_f   c_{k'\uparrow}^* c_{k\uparrow} \pm c_{k\downarrow}^* c_{k'\downarrow}   \psi_f)  ^2 \rangle_{Av}$	$\frac{1}{2} \left( 1 - \frac{(\varepsilon + \varepsilon_s)(\varepsilon' + \varepsilon_s) \mp \Delta^2}{EE'} \right) \times$ $(1 - f_{k+q\uparrow})(1 - f_{k'+q\uparrow})$	$\frac{1}{2} \left( 1 - \frac{(\varepsilon + \varepsilon_s)(\varepsilon' + \varepsilon_s) \mp \Delta^2}{EE'} \right) \times$ $(1 - f_{k+q\uparrow})(1 - f_{-k'+q\downarrow})$	$\frac{1}{2} \left( 1 - \frac{(\varepsilon + \varepsilon_s)(\varepsilon' + \varepsilon_s) \mp \Delta^2}{EE'} \right) \times$ $(1 - f_{-k+q\downarrow})(1 -$ $f_{k'+q\uparrow})$	$\frac{1}{2} \left( 1 - \frac{(\varepsilon + \varepsilon_s)(\varepsilon' + \varepsilon_s) \mp \Delta^2}{EE'} \right) \times$ $(1 - f_{-k+q\downarrow})(1 -$ $f_{-k'+q\downarrow})$
$W_i$ - $W_j$	$E_{k+q^+} + E_{k'+q^+}$	$E_{k+q^+} + E_{k'+q^+}$	$E_{k+q^+} + E_{k'+q^+}$	$E_{k+q^+} + E_{k'+q^+}$
$\langle  (\psi_f   c_{k'\uparrow}^* c_{k\uparrow} \pm c_{k\downarrow}^* c_{k'\downarrow}   \psi_f)  ^2 \rangle_{Av}$	$\frac{1}{2} \left( 1 - \frac{(\varepsilon + \varepsilon_s)(\varepsilon' + \varepsilon_s) \mp \Delta^2}{EE'} \right) \times$ $f_{k+q\uparrow} f_{k'+q\uparrow}$	$\frac{1}{2} \left( 1 - \frac{(\varepsilon + \varepsilon_s)(\varepsilon' + \varepsilon_s) \mp \Delta^2}{EE'} \right) \times$ $f_{k+q\uparrow} f_{-k'+q\downarrow}$	$\frac{1}{2} \left( 1 - \frac{(\varepsilon + \varepsilon_s)(\varepsilon' + \varepsilon_s) \mp \Delta^2}{EE'} \right) \times$ $f_{-k+q\downarrow} f_{k'+q\uparrow}$	$\frac{1}{2} \left( 1 - \frac{(\varepsilon + \varepsilon_s)(\varepsilon' + \varepsilon_s) \mp \Delta^2}{EE'} \right) \times$ $f_{-k+q\downarrow} f_{-k'+q\downarrow}$
$\frac{1}{8} \left( 1 + \frac{(\varepsilon + \varepsilon_s)(\varepsilon' + \varepsilon_s) \mp \Delta^2}{EE'} \right) \left( \frac{f_{k'+q\uparrow} - f_{k+q\uparrow}}{E_{k+q\uparrow} - E_{k'+q\uparrow}} + \frac{f_{-k'+q\downarrow} - f_{k+q\uparrow}}{E_{k+q\uparrow} - E_{-k'+q\downarrow}} + \frac{f_{k'+q\uparrow} - f_{-k+q\downarrow}}{E_{-k+q\downarrow} - E_{k'+q\uparrow}} + \frac{f_{-k'+q\downarrow} - f_{-k+q\downarrow}}{E_{-k+q\downarrow} - E_{-k'+q\downarrow}} \right) + \frac{1}{8} \left( 1 - \frac{(\varepsilon + \varepsilon_s)(\varepsilon' + \varepsilon_s) \mp \Delta^2}{EE'} \right) \left( \frac{1 - f_{k'+q\uparrow} - f_{k+q\uparrow}}{E_{k+q\uparrow} + E_{k'+q\uparrow}} + \frac{1 - f_{-k'+q\downarrow} - f_{k+q\uparrow}}{E_{k+q\uparrow} + E_{-k'+q\downarrow}} + \frac{1 - f_{k'+q\uparrow} - f_{-k+q\downarrow}}{E_{-k+q\downarrow} + E_{k'+q\uparrow}} + \frac{1 - f_{-k'+q\downarrow} - f_{-k+q\downarrow}}{E_{-k+q\downarrow} + E_{-k'+q\downarrow}} \right)$				
<p>Considering the integration from -1 to 1 for <math>x</math> and -1 to 1 for <math>x'</math>, the above expression can be replaced by,</p>				
$\frac{1}{2} \left( 1 + \frac{(\varepsilon + \varepsilon_s)(\varepsilon' + \varepsilon_s) \mp \Delta^2}{EE'} \right) \frac{f_{k'+q\uparrow} - f_{k+q\uparrow}}{E_{k+q\uparrow} - E_{k'+q\uparrow}} + \frac{1}{2} \left( 1 - \frac{(\varepsilon + \varepsilon_s)(\varepsilon' + \varepsilon_s) \mp \Delta^2}{EE'} \right) \frac{1 - f_{k'+q\uparrow} - f_{k+q\uparrow}}{E_{k+q\uparrow} + E_{k'+q\uparrow}}$				

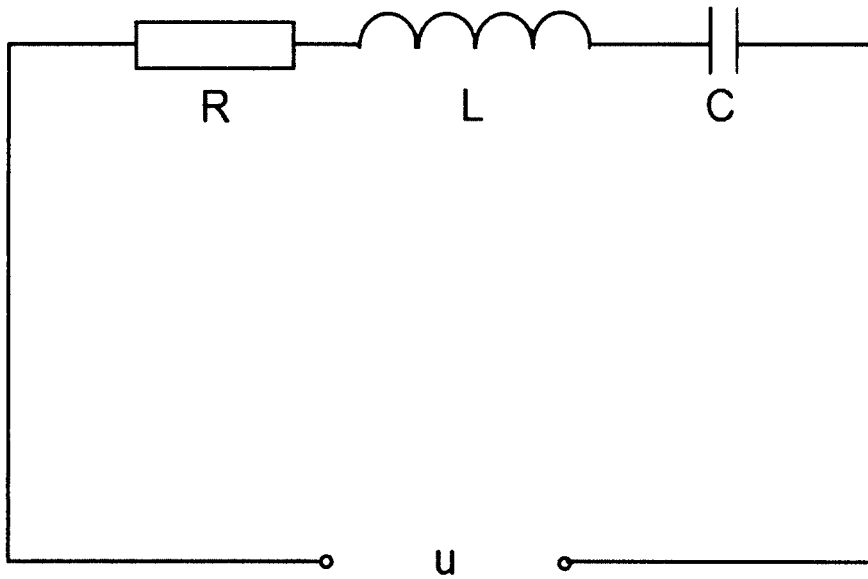


Figure 2.1. RLC series circuit.

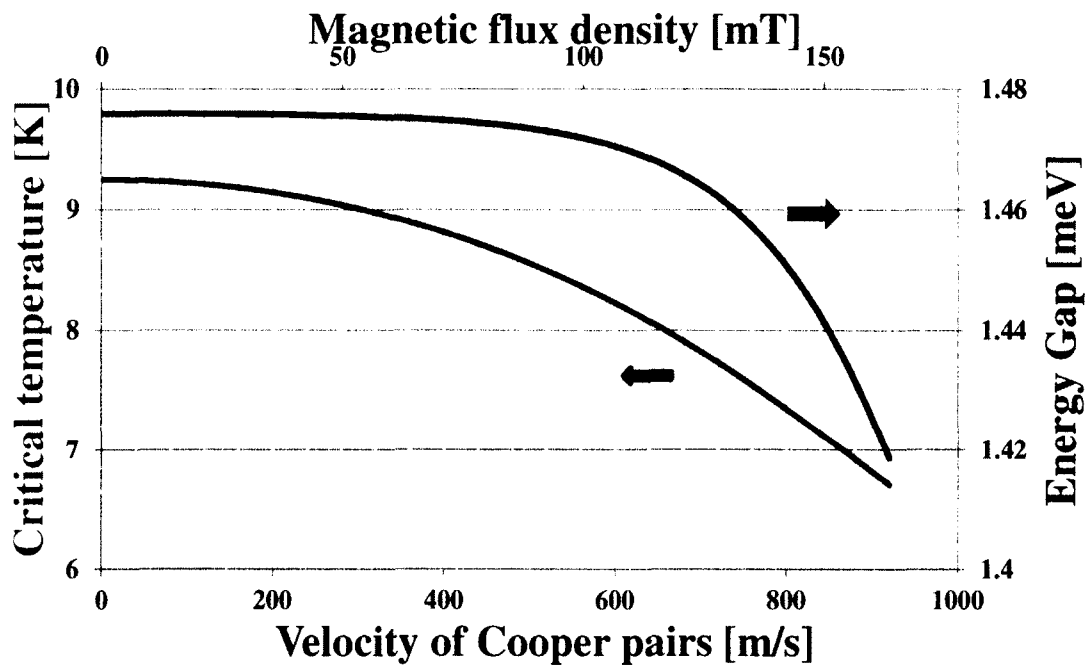


Figure 2.2. Energy gap at 2 K and critical temperature versus Cooper pair velocity with parameters set for Nb. The energy gap at zero Cooper pair velocity is 1.476 meV.

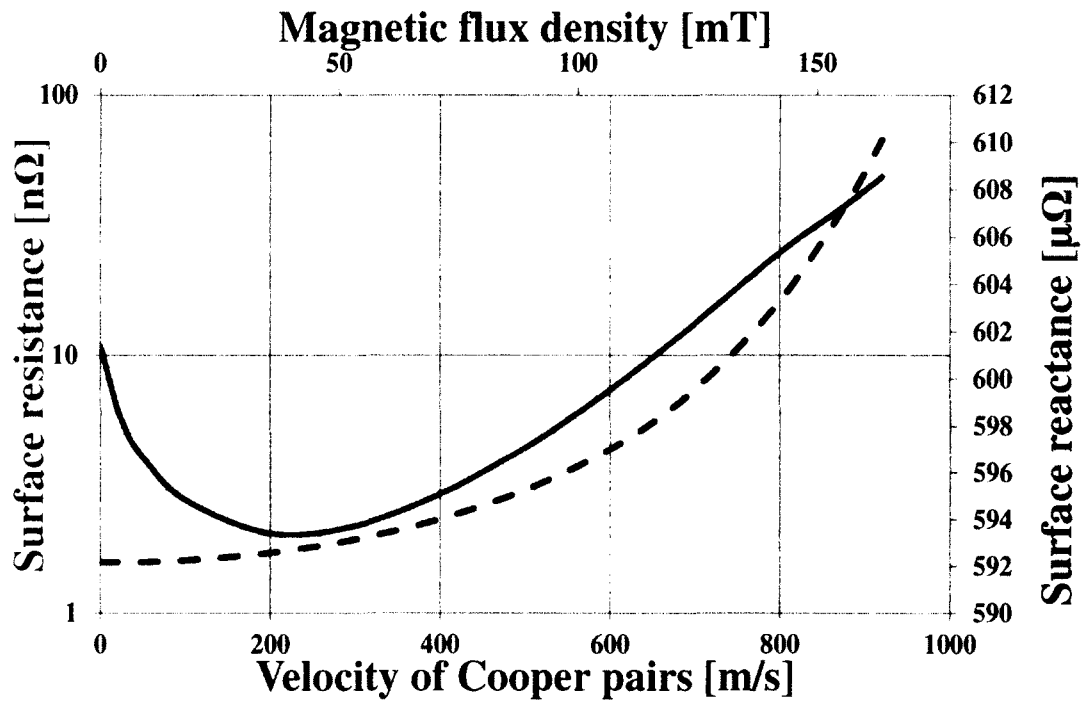


Figure 2.3. Surface resistance (red line) and reactance (blue dotted line) versus Cooper pair velocity for Nb at 2 K and 1.5 GHz.

## **CHAPTER 3**

### **SRF Surface Impedance Measurement Techniques**

#### **3.1. Brief Review**

In order to measure the surface impedance of a sample surface, it is necessary to make the sample a part of a resonant structure. Such a sample could be a rod [27, 28], a flat disk [27, 29-40] or just a small piece [27, 41, 42] inserted into the cavity inner surface. The cavity is then excited in a particular mode with the resonant frequency and  $Q$  easily measurable, allowing one to calculate the surface impedance in a straightforward way [27, 30, 33, 35-37, 40, 43-45] based on average losses and differential measurements with calibrated samples. Another way to measure the surface impedance with significantly higher resolution is to use a power compensation technique that combines calorimetric measurements with RF measurements [31, 34, 41, 42] which will be introduced in detail in Chapter 4.

#### **3.2. Choice of Cavity Geometry**

Cylindrically symmetric cavities operating in a  $TE_{0xx}$  mode are commonly chosen as the resonant circuits. [27, 28, 35-37, 40, 43-45] In such a cavity with these

modes the electric field lines are simple self-closing rings around the resonator axis and electric field lines vanish on cavity walls as well as on the sample, if positioned at the lateral end of the cavity. Moreover, in the ideal geometry, no RF current crosses the joint between the sample and the cavity and, with no surface-normal electric fields, electronic problems such as multipacting and heating due to dark current may be avoided.

For simple cavity geometries, these  $TE_{0xx}$  cavities can only be used to measure large-sized samples while maintaining suitably low resonance frequencies.

Other attempts with more complicated geometries, including the “triaxial” cavity [31], “quadrupole mode resonator” [41, 42], “mushroom cavity” [38, 39] and sapphire loaded SIC cavity [34] have been made, trying to overcome the limitation of simple TE mode cavities. Table 3.1 shows a comparison of these three systems.

Triaxial cavity starts from deformed coaxial line structure with 35 mm in length, 8 mm in inner diameter and the outer diameter shrinks from 44 mm to 18 mm, the sample has been put on the 18 mm open end. The whole cavity is put in a 100 mm diameter and 50 mm long cavity to minimize the resonance outside the cone structure. This structure could confine magnetic field to the center portion of the sample at 1.5 GHz while keeping the sample size small, with 25.4 mm diameter. However issues with multipacting effects were prevalent and limit the maximum magnetic field on the sample to be lower than 25 mT.

The quadrupole mode resonator use a 210 mm diameter and 351 mm long cylinder, and puts a four wire transmission line built from niobium rods in the cavity



center, the bottom end of the rods are bent to form half rings of 25mm radius, this structure is used to focus RF power onto the sample that is placed below the half rings. The quadrupole resonator uses comparably large samples, with a diameter of 7.5 cm. The resonance frequency is 400 MHz, it could be multiplied to 800 MHz and 1200 MHz. This approach exposes the sample's rectangular edge to 6.7% of the maximum RF magnetic field experienced on the sample. The shape of the sample is complicated in order to shield the calorimetric components from RF field, which creates some challenges for coordinating with other instruments and facilities used in sample preparation and characterization.

In a cylindrically symmetric cavity operating in a  $TE_{0xx}$  mode with sample placed at one open end, a higher ratio of diameter/length is preferred to confine magnetic field on the sample. However this setup will also produce high magnetic field at the end opposite to the sample. By deforming the shape of this end, the highest magnetic field could be shifted and averaged. The mushroom cavity and its upgrade version use  $TE_{013}$  like modes. Three  $TE_{011}$  modes have been stacked together and the top plate has been reshaped to a mushroom structure, so that the magnetic field could be averaged on a larger surface area. The peak magnetic field on the sample is 2.5 times of the peak magnetic field on the cavity wall. This mushroom cavity is constructed out of copper so that pulsed RF power could be conducted into the cavity and the loaded Q will not degrade that much until the sample reaches its critical field. The drawback of using copper cavity is that the Q of the whole setup is

mainly determined by the copper cavity, it's not sensitive to the contribution from the superconducting sample.

In the SIC system a sample is located at the open end of a cylindrical sapphire-loaded cavity. With two choke joints surrounding the cavity, the RF fields are confined within the center of the sample and the samples is physically, and thus thermally, separated from the rest of the cavity. The sample is placed on a holder with a controlled thermal conduction path to the liquid helium bath. The detailed description of SIC system will be in Chapter 4.

Compared to other designs, the SIC system inherits the merits of TE structure cavities and offers a good solution to the size issue while maintaining the resonant frequency relatively low. The unique design of the SIC system guarantees controlled RF field within the center of the sample, which simplifies the sample and sample holder structure and ensures the success of the RF-calorimetric combination measurement. The sample edges and the joint between sample and sample holder are shielded from high RF fields, therefore anomalous heating from vortex entry at edges is avoided.

### **3.3. Choice of Measuring Technique**

Surface impedance  $Z_s$  includes two parts, the real part is the surface resistance  $R_s$  and the imaginary part is the surface reactance  $X_s$ .

A simple way to measure the surface resistance is to measure the Q change with a reference sample and the sample to be measured.

The total loss in the resonance system is a sum of the loss of different parts:

$$P_t = \sum_i P_i$$

The Q of each part is defined as:  $Q_i = \frac{\omega U}{P_i}$

The Q of the resonance system is  $\frac{1}{Q_t} = \sum_i \frac{1}{Q_i}$

These Q values are strongly dependent on the surface resistance. While in the simulation, one can assume that the surface resistance is uniform inside the resonance system, noted as  $R_u$ , the filling factor and geometry factor of each part can be defined as:  $\eta_i = \frac{Q_t}{Q_i}$  and  $G_i = Q_i R_u$ . These two parameters are geometry dependent and are independent of surface resistance, both of them can be obtained from numerical RF simulation. The geometry factor of the resonance system is  $G = \sum_i G_i$ .

With the reference sample, the Q of the whole system is noted as  $Q_1$  and reference sample's Q is noted as  $Q_r$ . With the sample to be measured, the Q of the whole system is noted as  $Q_2$  and the sample's Q is noted as  $Q_s$ . Since the other portions of the system are the same during these two measurements, we have:

$$\frac{1}{Q_1} - \frac{1}{Q_r} = \frac{1}{Q_2} - \frac{1}{Q_s}$$

Normally the reference sample uses the same material as the cavity, so that filling factor of the sample is  $\eta = \frac{Q_1}{Q_r} = \frac{G}{G_r}$ , where  $G_r$  is the geometry factor of the sample, and  $Q_s = \frac{G_r}{R_s}$ ,  $R_s$  is the surface resistance of the sample, so that,

$$R_s = \frac{G}{\eta} \left( \frac{1}{Q_2} - \frac{1}{Q_1} \right) + \frac{G}{Q_1}$$

The measuring error of R can be represented as,

$$\Delta R_s = \sqrt{\left(\frac{G \Delta Q_2}{\eta Q_2^2}\right)^2 + \left[G \left(1 - \frac{1}{\eta}\right) \frac{\Delta Q_1}{Q_1^2}\right]^2}$$

Assume we have a copper cavity with  $Q_1$  at  $2 \times 10^5$ , geometry factor is 300, filling factor of the sample is 40%, and the sample's surface resistance is much small than the surface resistance of copper, then  $Q_2$  should be  $5 \times 10^5$ . Typically the Q's measurement error will be about 5%, from the above equation one can get that  $\Delta R_s$  should be 0.14 m $\Omega$ . That's why Q measurement with copper cavity is not preferred for SRF samples. While the cavity made of niobium has a  $Q_1$  at  $2 \times 10^8$ , and  $\Delta R_s$  would be improved to 140 n $\Omega$ .

Another way to measure the surface resistance with a significantly higher resolution is a power compensation technique, its detail is described in Chapter 4.

The above two methods are not sufficient for investigating localized effects that will cause non uniform temperature distribution on the sample. Temperature mapping system could be a supplemental system to investigate the non-uniform RF loss mechanism on the sample [26]. In this system, carbon Allen-Bradley resistors with 100  $\Omega$ , 5% accuracy and 1/8 W at room temperature have been used as the thermometers. Each resistor has been placed into a G-10 housing that filled with stycast 2850 FT epoxy to thermally isolate it from liquid helium, GE-varnish 7031 that are 50% diluted with a mixture of toluene and ethyl alcohol is used to electrically isolate resistor from cavity surface, and apiezon N grease is applied on top of the GE-varnish 7031 to ensure good thermally conductivity between cavity surface and

resistor. The whole thermometer has been mounted on G-10 printed circuit board using spring loaded pin. The spring loaded pin will be compressed from 2.464 cm to 2 cm during the measurement and the pressure applied to the resistor to ensure good thermal conductivity between resistor and cavity surface is about  $10^5$  pa. A total number of 576 thermometers have been applied to single cell CEBAF shape cavities. All thermometers need to be recalibrated during the cool down procedure for every cavity test, because the resistance of each resistor changes after the warm up cool down cycle between 2 K and room temperature.

Temperature mapping system is complex, considering a 7 cell section in a CEBAF shape cavity that is using temperature mapping system, the total number of thermometers used would be 4032, and the wires used to measure the resistance of these thermometers would be 8064. For a 9 cell cavity, more thermometers and wires would be needed. In some cases that detailed temperature information is not required, one may still want to know where the overheating happened first in the cavity that causes cavity to quench, described below, second sound system can meet this requirement [46]. During the RF measurement for a cavity, the cavity is surrounded by superfluid liquid helium. The thermal conductivity of superfluid liquid helium is 30 times that of copper, RF heat on cavity surface will be taken away to the liquid helium surface. With the increase of accelerating gradient in the cavity, more and more RF heat will be produced on the cavity's inner surface, the surface temperature will increase, and in certain local region, temperature would go beyond the critical temperature of Nb and local surface resistance will increase suddenly. Superfluid

liquid helium can no longer take that much power away, cavity's Q will suddenly drop and most of the RF power will reflect back. In this case, the ratio between superfluid helium atoms and normal helium atoms will dramatically decrease and second sound will be produced by the vibration of normal helium atoms. The speed of second sound in superfluid helium is a function of temperature. It's about 20 m/s at 1.8 K. By knowing the time difference between the quench happened, from the sudden change of the reflected or transmitted power, and the second sound detector start to receive signal, one may able to calculate the distance between where the second sound first produced and the location of the second sound detector and by using multiple detectors, the location of the second sound first produced can be determined within centimeter accuracy, comparable to the temperature mapping system.

Table 3.1. Comparison of RF surface characterization systems.

	Triaxial	Quadrupole	Mushroom	SIC
Frequency [GHz]	1.5	0.4/0.8/1.2	11.4	7.4
Sample size [cm <sup>2</sup> ]	5	44	20	20
RF sampled area <sup>1</sup> [cm <sup>2</sup> ]	1.5	6.9	7.5	0.8
B <sub>max</sub> achieved[mT]	25 <sup>2</sup>	50	400	14 <sup>3</sup>
Bpk/sqrt(U)[mT/sqrt(J)]	848.8	357.6	271	359.3
Sample geometry	Round disk	Cylinder	Round disk	Round disk

<sup>1</sup>sample area with  $B > 80\%B_{\max}$

<sup>2</sup>limited by multipacting effect

<sup>3</sup>limited by 22 watt power source

## **CHAPTER 4**

# **SRF Surface Impedance Characterization System – RF Portion**

### **4.1. Introduction**

The SIC system is designed to measure the low temperature RF impedance of superconducting material samples, small enough to be accommodated in commercial surface characterization instrument, surface treatment facilities, and laboratory-based thin film deposition equipment. The apparatus consists of two major parts which come together at the sample under test. The RF portion shapes and controls the field presented to the sample surface. The calorimeter portion provides a means of measuring the RF power dissipation on the sample. The original design of the JLab SIC system was covered by [15, 29, 47, 48].

The SIC system is based on a cylindrical polycrystalline niobium cavity with 2 cm inner diameter, shown in Figure 4.1. A HEMEX® sapphire rod from Crystal Systems is inserted into the cavity to lower the resonant frequency of this size cavity



to 7.4 GHz in the TE<sub>011</sub> mode. Two adjustable loop couplers are located above the cavity, and their external quality factors may be varied from 10<sup>6</sup> to 10<sup>10</sup> for this mode. The sapphire is tightly held from the top, and its bottom surface is set to be coplanar with the bottom of the cavity. The sample is located at the open end of the cavity and is thermally isolated from the bottom plane of the cavity cylinder and sapphire, being separated from them by a 0.02 cm gap. Two RF choke joints with a 1 cm depth are used at the bottom of the cavity to minimize the RF power leakage. This system provides well-controlled RF fields within the central 0.8 cm<sup>2</sup> area of samples with 5 cm in diameter.

## 4.2. Calculation on Simplified Model

In a simplified model without gap between the cavity/sapphire and the sample, shown in Figure 4.2, field distribution of TE<sub>011</sub> mode can be calculated from Maxwell equations.

$$\nabla \cdot \vec{D} = 0 \quad (\text{a})$$

$$\nabla \cdot \vec{B} = 0 \quad (\text{b})$$

$$\nabla \times \vec{E} = i\omega\vec{B} \quad (\text{c})$$

$$\nabla \times \vec{H} = -i\omega\vec{D} \quad (\text{d})$$

$$\text{With } \vec{D} = \epsilon\vec{E} \text{ and } \vec{B} = \mu\vec{H}$$

The boundary condition is  $\vec{n} \cdot \vec{H} = 0$  and interface conditions are:

$$\vec{e}_\rho \cdot \vec{D}_A = \vec{e}_\rho \cdot \vec{D}_B \quad \vec{e}_\rho \cdot \vec{B}_A = \vec{e}_\rho \cdot \vec{B}_B \quad \vec{e}_\rho \times \vec{E}_A = \vec{e}_\rho \times \vec{E}_B \quad \vec{e}_\rho \times \vec{H}_A = \vec{e}_\rho \times \vec{H}_B$$

For vacuum  $\varepsilon = \varepsilon_0$ , and for sapphire  $\varepsilon = \varepsilon_0 \begin{bmatrix} \varepsilon_r & 0 & 0 \\ 0 & \varepsilon_r & 0 \\ 0 & 0 & \varepsilon_z \end{bmatrix}$ , with  $\varepsilon_r = 9.3$  and

$$\varepsilon_z = 11.5.$$

For TE mode,  $E_z = 0$ . Since the dielectric constant will only affect equation  $\vec{D} = \varepsilon \vec{E}$ , we do not have to consider the anisotropy of dielectric constant for TE mode.

For a traveling wave in z direction,  $\vec{E}$  and  $\vec{B}$  can be written as:

$$\vec{E} = \nabla \times \nabla \times (W \vec{e}_z) \quad \vec{B} = -i\omega\mu\varepsilon \nabla \times (W \vec{e}_z)$$

Where W is the hertz vector.

Maxwell equations become,

$$\nabla^2 W + k_0^2 \varepsilon' W = 0$$

With  $k_0 = \sqrt{\mu_0 \varepsilon_0} \omega = \frac{2\pi f}{c}$ , c is the speed of light, and  $\varepsilon' = \begin{cases} \varepsilon_r, & 0 \leq \rho \leq a \\ 1, & a \leq \rho \leq R \end{cases}$

Variable separation for W:

$$W(\rho, \varphi, z) = D(\rho)\Phi(\varphi)Z(z)$$

For standing wave,  $Z(z) = \sin(\frac{p\pi}{L} z)$  with  $h = \frac{p\pi}{L}$

$$\frac{d^2\Phi}{d\varphi^2} = -m^2\Phi \quad \Rightarrow \quad \Phi(\varphi) = \cos(m\varphi)$$

$$\frac{d^2D}{d\rho^2} + \frac{1}{\rho} \frac{dD}{d\rho} + \left( k_0^2 \varepsilon' - h^2 - \frac{m^2}{\rho^2} \right) D = 0$$

$k_A = \sqrt{k_0^2 \varepsilon_r - h^2}$ ,  $k_B = \sqrt{k_0^2 - h^2}$  are the wave numbers in sapphire and

under vacuum, separately.

$$\text{Solution } D = \begin{cases} J_m(k_A \rho), & 0 \leq \rho \leq a \\ A_1 J_m(k_B \rho) + A_2 N_m(k_B \rho), & a \leq \rho \leq R \end{cases}$$

$$\text{So } D' = \frac{dD}{d\rho} = \begin{cases} k_A J_m'(k_A \rho), & 0 \leq \rho \leq a \\ A_1 k_B J_m'(k_B \rho) + A_2 k_B N_m'(k_B \rho), & a \leq \rho \leq R \end{cases}$$

$$W = D \cos(m\varphi) \sin\left(\frac{p\pi}{L} z\right) \quad \frac{\partial W}{\partial z} = \frac{p\pi}{L} D \cos(m\varphi) \cos\left(\frac{p\pi}{L} z\right)$$

From (h) the electromagnetic field distribution of TE mode can be calculated

$$\begin{cases} H_\rho = \frac{p\pi}{L} D' \cos(m\varphi) \cos\left(\frac{p\pi}{L} z\right) \\ H_\varphi = -\frac{p\pi}{\rho L} m D \sin(m\varphi) \cos\left(\frac{p\pi}{L} z\right) \\ H_z = D \cos(m\varphi) \sin\left(\frac{p\pi}{L} z\right) \left[ k_0^2 \epsilon' - \left(\frac{p\pi}{L}\right)^2 \right] \\ E_\rho = -i\omega\mu_0 \frac{m}{\rho} D \sin(m\varphi) \sin\left(\frac{p\pi}{L} z\right) \\ E_\varphi = -i\omega\mu_0 D' \cos(m\varphi) \sin\left(\frac{p\pi}{L} z\right) \end{cases}$$

$D$  and  $D'$  can be determined by applying the boundary conditions of  $\text{TE}_{mnp}$ :

$W|_{z=0,L} = 0$ , the above expression is already satisfied.

$$\left. \frac{\partial W}{\partial \rho} \right|_{\rho=R} = 0 \quad \Rightarrow \quad A_1 J_m'(k_B R) + A_2 N_m'(k_B R) = 0$$

Electromagnetic field distribution should be continuous on the vacuum/sapphire interface,

$$\epsilon_r m J_m(k_A a) = m A_1 J_m(k_B a) + m A_2 N_m(k_B a)$$

$$k_A J_m'(k_A a) = A_1 k_B J_m'(k_B a) + A_2 k_B N_m'(k_B a)$$

$$m J_m(k_A a) = m A_1 J_m(k_B a) + m A_2 N_m(k_B a)$$

$$k_A^2 J_m(k_A a) = k_B^2 A_1 J_m(k_B a) + k_B^2 A_2 N_m(k_B a)$$

For  $\text{TE}_{0np}$  mode,  $A_1$  and  $A_2$  are determined from:

$$A_1 = -\frac{k_A J_0'(k_A a) N_0'(k_B R)}{k_B N_0'(k_B a) J_0'(k_B R) - J_0'(k_B a) N_0'(k_B R)}$$

$$A_2 = \frac{k_A J_0'(k_A a) J_0'(k_B R)}{k_B N_0'(k_B a) J_0'(k_B R) - J_0'(k_B a) N_0'(k_B R)}$$

and  $k_A$  and  $k_B$  can be calculated from the below two equations:

$$k_B = \sqrt{\frac{k_A^2}{\epsilon_r} + \left(\frac{p\pi}{L}\right)^2 \left(\frac{1}{\epsilon_r} - 1\right)}$$

$$\begin{aligned} k_A J_0(k_A a) [N_0'(k_B a) J_0'(k_B R) - J_0'(k_B a) N_0'(k_B R)] \\ = k_B J_0'(k_A a) [N_0(k_B a) J_0'(k_B R) - J_0(k_B a) N_0'(k_B R)] \end{aligned}$$

$$\text{Resonant frequency of this mode is } f = \frac{c}{2\pi\sqrt{\epsilon_r}} \sqrt{k_A^2 + \left(\frac{p\pi}{L}\right)^2}.$$

With the dimension above, the resonant frequency of TE011 mode is determined to be 7.617GHz.

The field distribution is shown in Figure 4.3.

### 4.3. SuperFish Simulation

SuperFish program has been used to do 2-D electromagnetic simulation on SIC RF system with choke joints and gap between the cavity and the sample. The SuperFish code with gap at 0.1 mm is attached in Appendix D.

Using this code, the maximum magnetic fields on the sample under different gap for 2<sup>nd</sup> generation cavity with 0.06 inch cap are calculated and plotted in Figure 4.4.

### 4.4. RF Couplers

Two H-field loop couplers are used in SIC system, they are mechanically adjustable from outside while the cavity is in the Dewar. By changing the couplers' position, their external Q will be changed. In Figure 4.5 we show the 2 K experimental results of couplers' external Q versus their positions.

The couplers are symmetrically located near the sapphire rod, which leads to cross talk during room temperature measurements and even during 2 K measurements because the loaded Q is now typically  $10^7$ . Theoretically cross talk will diminish [49] if we can push loaded Q higher.

The inner conducting material of the couplers is stainless steel, and the outer conductor is made of Cu, with Teflon (dielectric constant at 2.1) between them. The surface resistance of stainless steel at 7.5 GHz is around  $0.1 \Omega$  [18]. The coupler is made of a standard  $50 \Omega$  cable with 3.2 mm inner diameter of outer conductor. Assuming the inner and outer conductors are all stainless steel, the voltage attenuation of this cable should be

$$\alpha = \frac{1}{2} \left[ \frac{R_S}{\eta \ln \frac{b}{a}} \left( \frac{1}{a} + \frac{1}{b} \right) \right] = \frac{1}{2} \left[ \frac{0.1}{377/\sqrt{2.1} \times \ln 3.2} \left( \frac{1}{0.001} + \frac{1}{0.0032} \right) \right] = 0.2 \text{ (1/m)}$$

The length of the couplers is normally less than 0.1 m, so the power loss should be less than  $1 - e^{-2 \times 0.2 \times L} = 0.04$ , that is less than 0.2 dB. Considering that the inner conductor is Ag-plated stainless steel and outer conductor is Cu, the loss on coupler is much less than 0.2 dB.

## 4.5. Sapphire

Sapphire is a key component in the SIC system, it can not only reduce the  $TE_{011}$  frequency from 19.8GHz to 7.4GHz, but also focuses RF field in the sample plate region instead of cavity wall region. MathCAD simulation shows that the power loss ratio of sample plate/total can increase from 1.2% to 8.3% by adopting sapphire.

With a sapphire rod inserted into the  $TE_{011}$  cavity, the  $TE_{011}$  mode will propagate along the sapphire and leak from the top end of the sapphire. Figure 4.6 is the simulation result (by Haipeng Wang using HFSS) of the radiation loss external  $Q$  with different sapphire rod lengths. The blue curve shows the calculated result, which is limited by the calculation accuracy and shows a lower limitation of  $10^4(A/m)^2$ . The red curve shows the linear fitting that can avoid calculating limitation. The previous design with a 63.754mm sapphire rod will limit the loaded  $Q$  to  $2.34 \times 10^7$ . With the present design of 105.87mm (114mm in length with 8.13mm inside Nb cap, sealed with indium between Nb cap and cavity neck), radiation loss external  $Q$  is  $1.6 \times 10^{22}$ , quite negligible comparing with our desired loaded  $Q$  ( $10^8$  to  $10^9$ ).

Initially the sapphire rod was brazed onto a Nb cap, which also caused significant RF loss on it, this design has been changed to the current one with sapphire clamped onto a Nb cap, shown as component A in Figure 4.1.

The sapphire has been cleaned with the following procedure before it has been put into the cavity [50]. All operations must be conducted in a chemical hood while wearing suitable personal protective equipment.

1. Create Nitric acid solution (1:3 =  $HNO_3:H_2O$  )
2. Place sapphire in the container holding the solution and place that container in an ultrasonic cleaner for 5 minutes
3. Remove from cleaner and heat until boiling using hot plate or other method available. Once boiling is achieved, stop heating and let cool to room temperature. Wait at least 20 minutes.

4. Rinse twice with deionized water
5. Rinse with Acetone
6. Ultrasonicate for two minutes in Acetone
7. Rinse with Isopropanol
8. Ultrasonicate for two minutes in Isopropanol
9. Rinse with Ethanol (200 proof)
10. Ultrasonicate for two minutes in Ethanol
11. Keep in ethanol until ready to assemble.

While simulating the SIC system with sapphire, the c-axis crystal orientation of sapphire is set to be coincident with the axis of cylindrical Nb cavity. The actual c-axis will deviate from the physical axis of sapphire rod with a maximum  $0.5^\circ$  angle. While mounting the sapphire, there is a possibility that the sapphire's physical axis will not be coincident with the axis of Nb cavity. There is an angle between the c-axis of sapphire and the axis of cylindrical Nb cavity, marked as  $\alpha$  in Figure 4.7. The MicroWave Studio simulation results show that with 0.2 mm gap between sample and cavity, the quality factor of  $TE_{011}$  mode drops from  $1.2 \times 10^{14}$  with  $\alpha = 0$  degree to  $3.13 \times 10^{11}$  with  $\alpha = 1$  degree, both are much higher than the quality factor dominated by the surface resistance of Nb, indicating that the tilting effect of crystal orientation is negligible in the SIC system.

## **4.6. Choke Joints**

In order to prevent RF power leakage from the gap between sample plate and cavity, two choke joints are used. The choke joints are designed for 7.4 GHz, with  $\lambda/4$  (about 1 cm) in depth. The inner choke has an inner diameter of 25.4 mm and an outer diameter of 31.75 mm, the second choke has an inner diameter of 38.1 mm and an outer diameter of 44.45 mm.

#### **4.7. TE<sub>011</sub> Mode Identification**

SIC system uses an “open gap” design to separate the sample plate from the Nb cavity, so that we can measure rf induced heat accurately, this also gives us benefit on TE<sub>011</sub> mode identification. By tuning the gap between cavity and sample plate, the resonant frequency can be tuned. Based on MAFIA simulation (by Haipeng Wang), MWS simulation (by Frank Marhauser) and Superfish simulation, we get the value of tuning sensitivity as 20 Hz/nm. Figure 4.8 shows the simulation and experimental (room temperature and 4 K) results of tuning sensitivity of TE<sub>011</sub> mode. They are in good agreement, given confidence that the particular resonant mode at 7.4 GHz is the TE<sub>011</sub> mode.

#### **4.8. RF Control Circuit**

The RF control circuit for the SIC system is shown in Figure 4.9. More details are shown in Appendix E. It uses a voltage controlled oscillator (VCO) configured in a phase locked loop (PLL) scheme. A double balance mixer is used to compare the RF phase of a signal from the VCO with the transmitted signal from the cavity. The output voltage from the IF port of the double balance mixer is directly related to the



difference between VCO output frequency and cavity resonant frequency. This output voltage is then used to tune the VCO and force it follow the cavity resonant frequency. This RF control circuit can work either in CW mode or in pulsed mode, controlled by the RF pin diode switch.

With certain DC voltage, VCO will give us a resonant rf power:

$$V_{vco}(t) = V_0 \sin(\omega t)$$

This signal will be sent into the cavity after passing through a directional coupler, attenuator, pin diode switch and some amplifiers. The signal that we send into the cavity can be showed as below:

$$V_{cavity-input}(t) = k_A V_0 \sin(\omega t)$$

$k_A$  is the amplitude changed by those components that the signal passes through.

One can treat the cavity as an LRC circuit and get the output signal from the cavity [51]:

$$V_{cavity-output}(t) = \frac{k_A V_0}{\sqrt{1 + \tan^2 \psi}} \sin(\omega t + \psi) \text{ with } \tan \psi = 2Q_L \frac{\Delta f}{f} \text{ while } \Delta f \ll f ,$$

here  $f = \frac{\omega}{2\pi}$ ,  $\Delta f = f_0 - f$  and  $f_0$  is the characteristic frequency of cavity. We

should notice due to the pressure change in the Dewar the  $f_0$  will have small fluctuation during the low temperature test.

The output signal will pass through an amplifier and a directional coupler and then input into the RF port of a mixer:

$$V_{RF}(t) = k_B V_{cavity-output}(t) = \frac{k_A k_B V_0}{\sqrt{1 + \tan^2 \psi}} \sin(\omega t + \psi)$$

$k_B$  is the amplitude changed by those components that the signal passes through.

The output from VCO will pass through two directional couplers and a phase shifter, then it will be sent into the LO port of a mixer:

$$V_{LO}(t) = k_C V_0 \sin(\omega t + \phi)$$

$k_C$  is the amplitude changed by those components that the signal passes through and  $\phi$  is the phase changed by the phase shifter.

A) DC output from mixer

When we mix these two signals in a double balanced mixer, the DC component (after a low pass filter) of the output should be:

$$V_{out} = \frac{k_m V_0^2}{\sqrt{1 + \tan^2 \psi}} \cos(\psi - \phi) = \frac{k_m V_0^2}{1 + \tan^2 \psi} (\cos \phi + \tan \psi \sin \phi)$$

Where  $k_m = k_A \times k_B \times k_C \times k_D$ ,  $k_D$  is the amplitude change of the diodes in the double balanced mixer with per volt unit.

If  $\Delta f$  is small, even smaller comparing with  $f_{FWHM}$ , that is

$$\Delta f \ll \frac{f}{2Q_L} = \frac{f_{FWHM}}{2}, \text{ which also means } \tan \psi \ll 1, \text{ we get:}$$

$$V_{out} = k_m V_0^2 (\cos \phi + \tan \psi \sin \phi) = k_m V_0^2 (\cos \phi + 2 \frac{\Delta f}{f_{FWHM}} \sin \phi)$$

Which indicates that the DC output of the mixer is proportional to the difference between cavity resonant frequency and VCO output frequency.

We should also notice this will not always be true since  $\Delta f$  may be comparable to or even larger than  $f_{FWHM}$  while VCO output frequency  $f$  is close to cavity resonant frequency  $f_0$ .

B) Equilibrium status, mixer output voltage, frequency difference and tuning sensitivity

The tuning voltage of VCO can be calculated by set  $\phi = \frac{\pi}{2}$ . Physically this could be achieved by tuning the phase shifter adjacent to VCO. We have,

$$V_{tune} = \frac{kV_0^2 \tan \psi}{1 + \tan^2 \psi} + V_{DC}$$

Here  $V_{DC}$  is the DC offset,  $k = k_m \times k_E$  and  $k_E$  is the amplitude change by those components that the signal passes through from the mixer DC output to VCO DC input. So we can get,

$$f_{VCO} = \frac{kV_0^2 \tan \psi}{1 + \tan^2 \psi} g_V + f_{DC}$$

Where  $g_V$  is the tuning sensitivity of VCO,  $f_{DC}$  is the center frequency induced by  $V_{DC}$ . Since it is equilibrium status, we have  $f_{VCO} = f$ , so we can get:

$$4(f - f_{DC})\Delta f^2 - 2kV_0^2 g_V f_{FWHM} \Delta f + f_{FWHM}^2 \frac{f - f_{DC}}{f} = 0$$

$$\text{So } \Delta f = f_{FWHM} \frac{kV_0^2 g_V \pm \sqrt{k^2 V_0^4 g_V^2 - 4 \frac{(f - f_{DC})^2}{f}}}{4(f - f_{DC})}$$

$$\text{and } g_v = \frac{f_{VCO} - f_{DC}}{V_{tune} - V_{DC}} = \frac{f - f_{DC}}{V_{tune} - V_{DC}} = \frac{f - f_{DC}}{\left( \frac{kV_0^2 \tan \psi}{1 + \tan^2 \psi} \right)} = \frac{(f - f_{DC})(f_{FWHM}^2 + 4\Delta f^2)}{2kV_0^2 f_{FWHM} \Delta f}$$

C) Determine tuning sensitivity

$$g_v = \frac{(f - f_{DC})(f_{FWHM}^2 + 4\Delta f^2)}{2kV_0^2 f_{FWHM} \Delta f}$$

1)  $V_0$  is in volts range, determined by VCO output power (design value 11dBm, typical value 13dBm).

2)  $f - f_{DC}$  should be between  $\sqrt{2}f_{FWHM}$  and  $\Delta f$  (or  $\Delta f$  to  $-\sqrt{2}f_{FWHM}$  if  $\Delta f < 0$ )

3)  $f_{FWHM}$  is in 10Hz range while  $Q_0$  is  $10^9$  and in kHz range while  $Q_0$  is  $10^7$ .

4) Assume that  $S_{21}$  is Gaussian distribution, in this case we will not consider crosstalk issue.

We know that Gaussian distribution function is

$$E = E_0 \exp\left(-\frac{(f - f_0)^2}{2\sigma^2}\right)$$

$$\text{While } E = E_0/2, f_{FWHM} = f_0/Q_0, \text{ from where we can get } \sigma = \frac{f_0}{2\sqrt{2 \ln 2} Q_0}$$

In order to let the amplitude of cavity output contains  $\Delta f$  information, and assume in  $E > E_0/10$  range the signal could be separated from noise level, we have

$$E = E_0 \exp\left(-\frac{(f - f_0)^2}{2\sigma^2}\right) > \frac{E_0}{10}$$

$$\text{So } \Delta f = f_{FWHM} \sqrt{\frac{\ln 10}{\ln 2}} = 1.82 f_{FWHM}$$

However it is not always true,  $\Delta f$  could be much more than  $f_{FWHM}$ . In this case, the amplitude of cavity output is small, but the phase change still contains  $\Delta f$  information.

$$5) k = k_m \times k_E = k_A \times k_B \times k_C \times k_D \times k_E$$

$k_A$  corresponds to 19 dB gain or 32 dB gain, which means  $k_A=8.9$  or 39.8

$k_B$  corresponds to 29.8 dB gain, which means  $k_B=30.9$

$k_C$  corresponds to -20.7 dB gain, which means  $k_C=0.09$

$k_D$  corresponds to the conversion loss of the mixer, which is about 5 dB, we have  $k_D = 0.56$ .

$k_E$  equals to 1, 2, 5 or 10, depending on the range we want to choose to amplify the DC voltage from mixer.

So  $k$  could be one of the following design values: 13.86, 27.72, 69.30, 138.61, 61.98, 123.97, 309.91, 619.83.

From the design values above, we get that  $g_v$  is about 0.008 to 360 Hz/V

## 4.9. Summary

Cylindrically symmetric cavity operating in a  $TE_{011}$  mode is chosen as the resonant circuit for the SIC RF system. In such a cavity with this mode, the electric field lines are simple self-closing rings around the resonator axis and electric field lines vanish on cavity walls as well as on the sample, if positioned at the lateral end of the cavity. Moreover, in the ideal geometry, no RF current crosses the joint between

the sample and the cavity and, with no surface-normal electric fields, electronic problems such as multipacting and heating due to dark current may be avoided. Compared to other designs, the SIC system inherits the merits of TE structure cavities and offers a good solution on the size issue while maintaining the resonant frequency relatively low. And the unique design of the SIC system guarantees controlled RF field within the center of the sample, which simplifies the sample and sample holder structure and ensures the success of the RF-calorimetric combination measurement. The sample edges and the joint between sample and sample holder are shielded from high RF fields, therefore anomalous heating from vortex entry at edges is avoided.

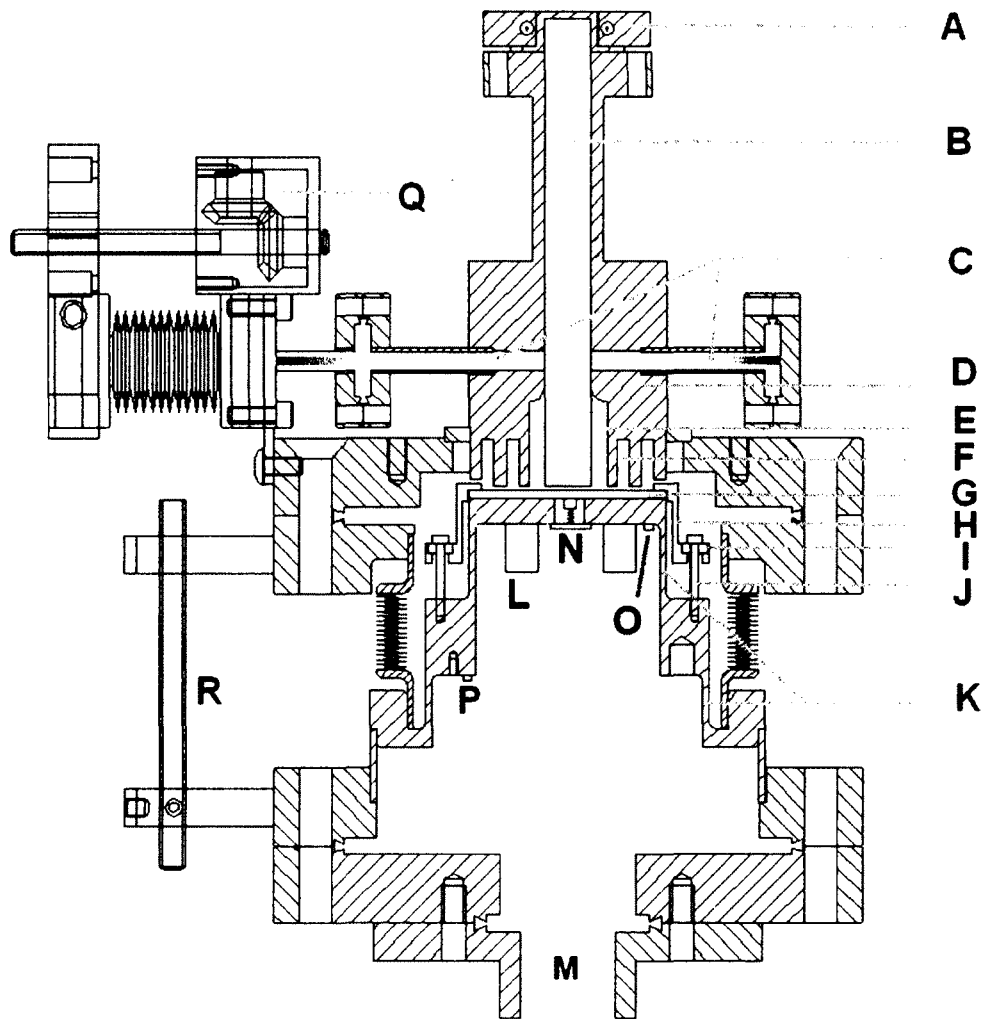


Figure 4.1. SIC system overview. A. Cap for sapphire rod, B. Sapphire rod, C. RF coupler, D. Nb cavity body, E. TE011 cavity, F. Double choke joints, G. Sample on top of copper sample holder, H. Stainless steel sample clamp, I. G-10 washer (x6), J. Aluminium bolt (x6), K. Upper and lower thermal insulators, L. Ring heater, M. Port for vacuum and wires. (Vacuum port of the cavity is not shown), N. Thermal sensor mounted on spring, O&P. Thermal sensor, Q. Coupler tuning mechanism, R. Distance tuning mechanism (x3).

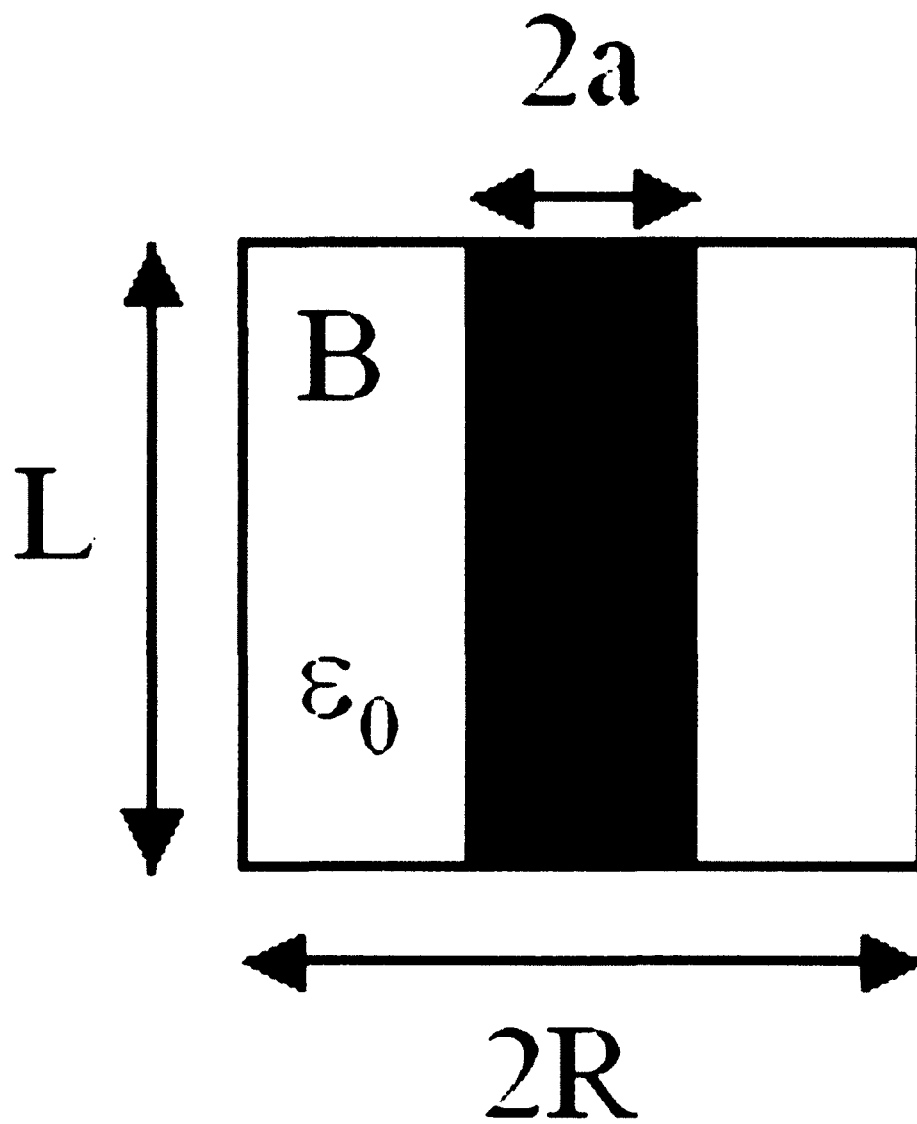


Figure 4.2. Simplified model of the SIC system with blue color section sapphire and white color section vacuum.



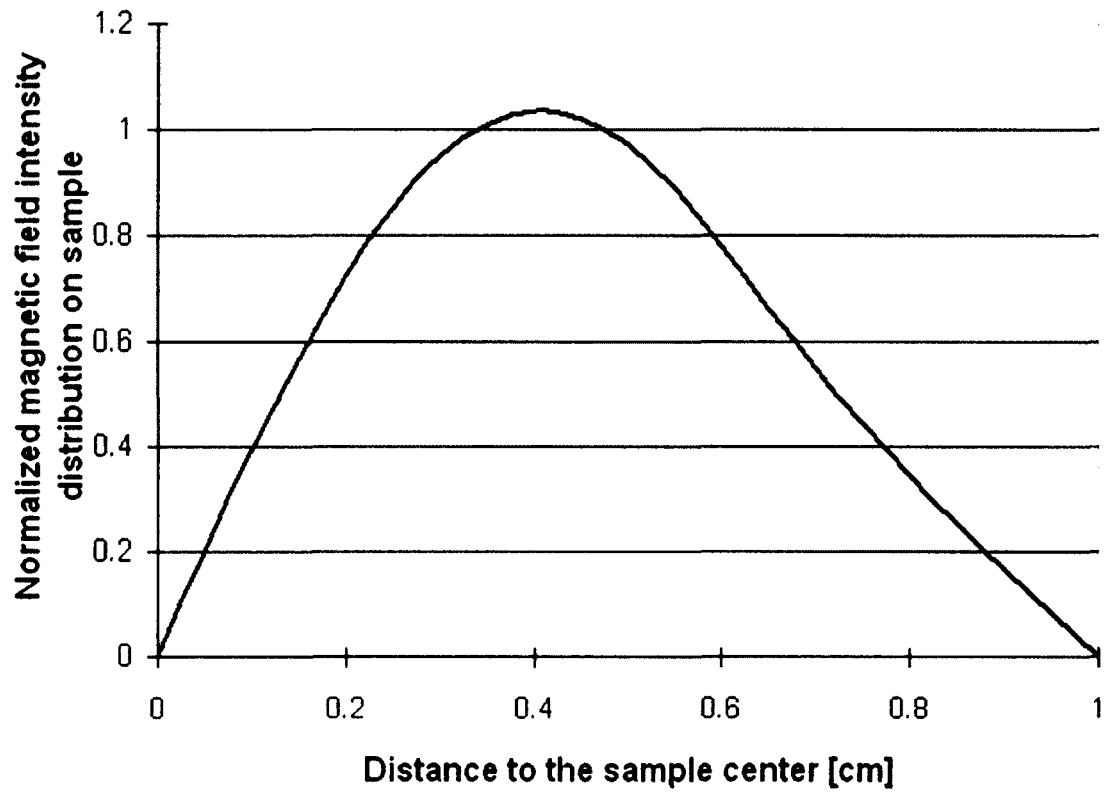


Figure 4.3. Magnetic field intensity distribution on the sample surface, normalized to the peak magnetic field intensity on the cavity.

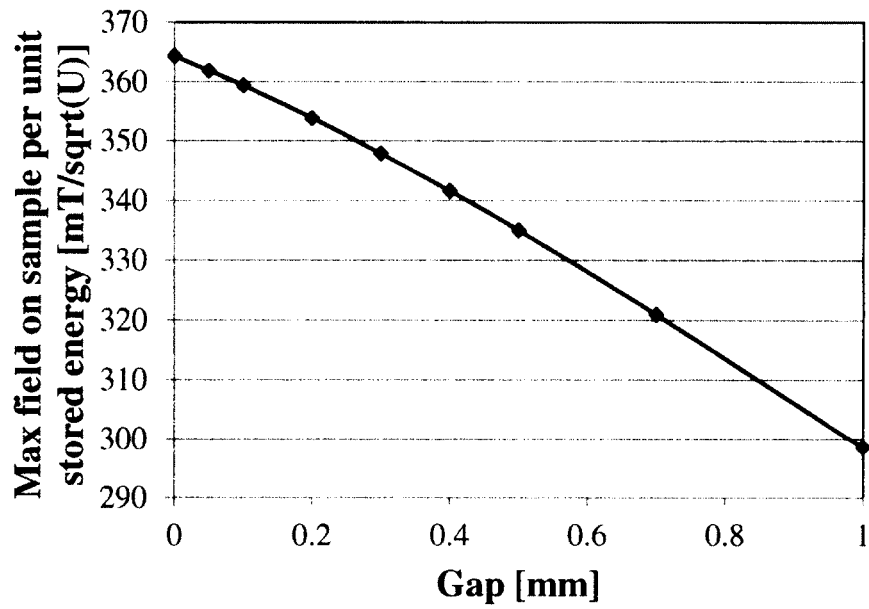


Figure 4.4. Maximum magnetic fields on the sample per stored energy under different gap condition for 2<sup>nd</sup> generation cavity with 0.06 inch cap, based on SuperFish 2D simulation.

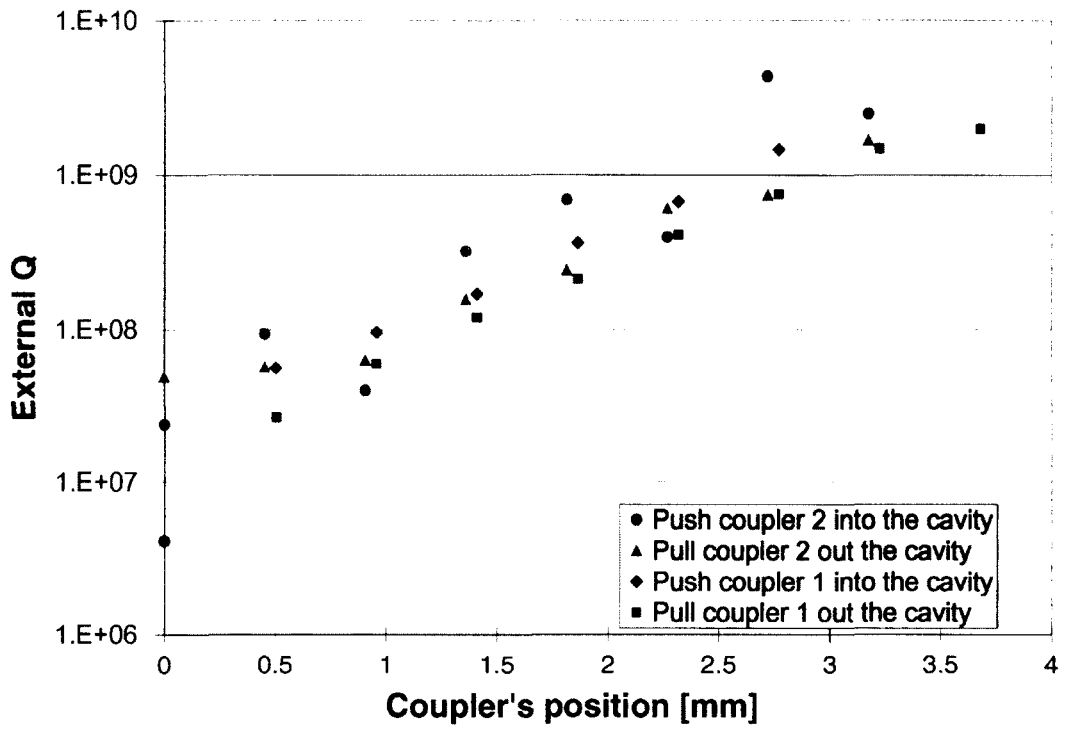


Figure 4.5. Couplers' external Q versus position.

Sapphire Rod Length Calculation to the Radiation Loss External Q in SIC Cavity

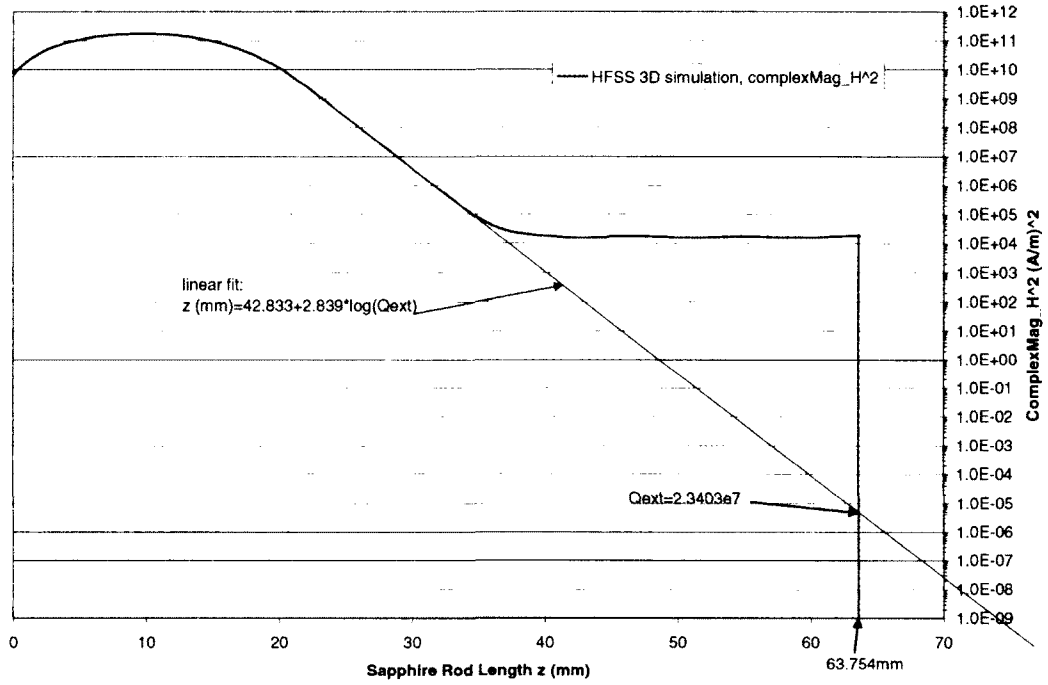


Figure 4.6. Sapphire rod length calculation to the radiation loss external Q in SIC cavity.

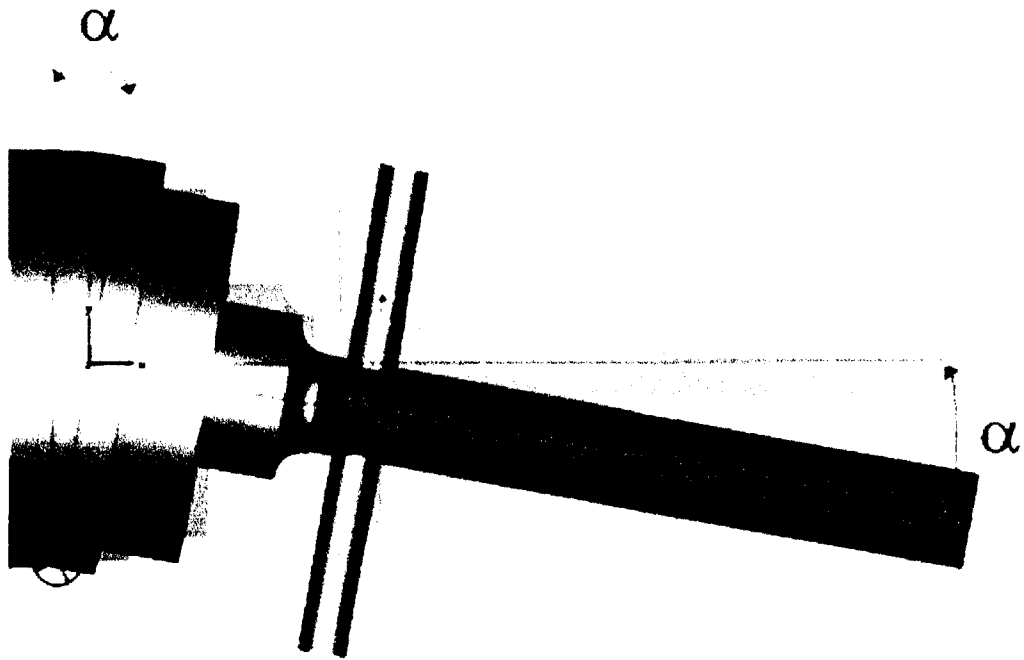


Figure 4.7. Misalignment of sapphire's physical axis to the axis of Nb cavity, here  $\alpha = 10$  degrees is illustrated for visibility only.

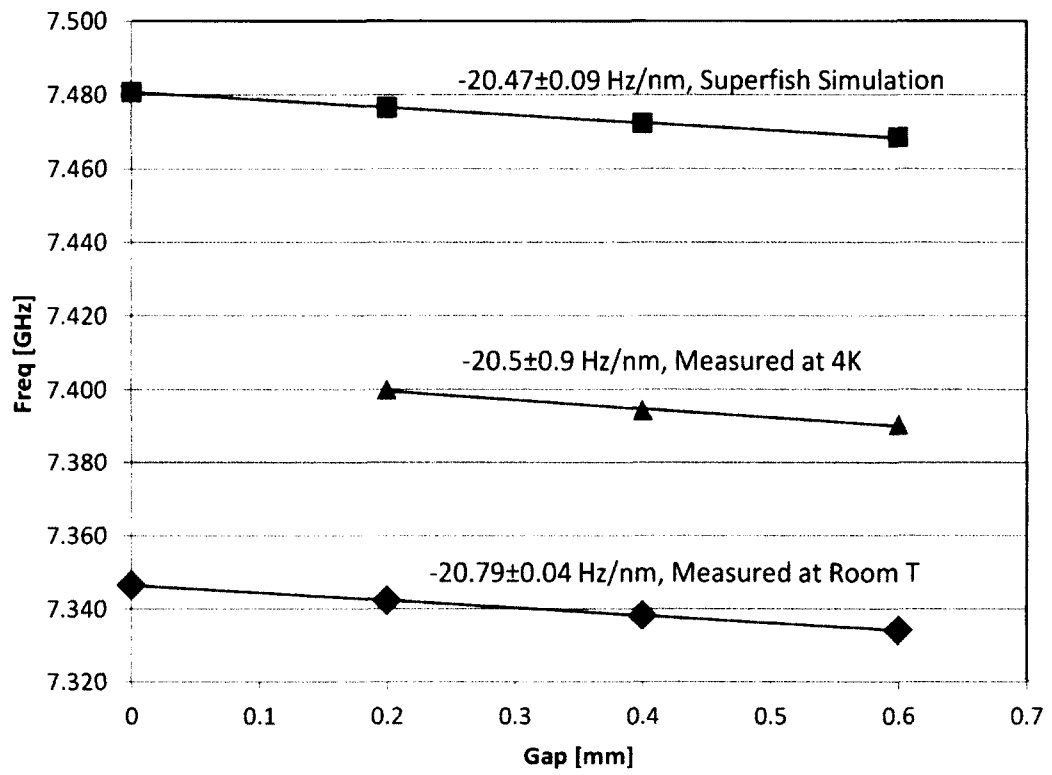


Figure 4.8. Tuning sensitivity of TE<sub>011</sub> mode: simulation, room temperature and 4 K measurement.

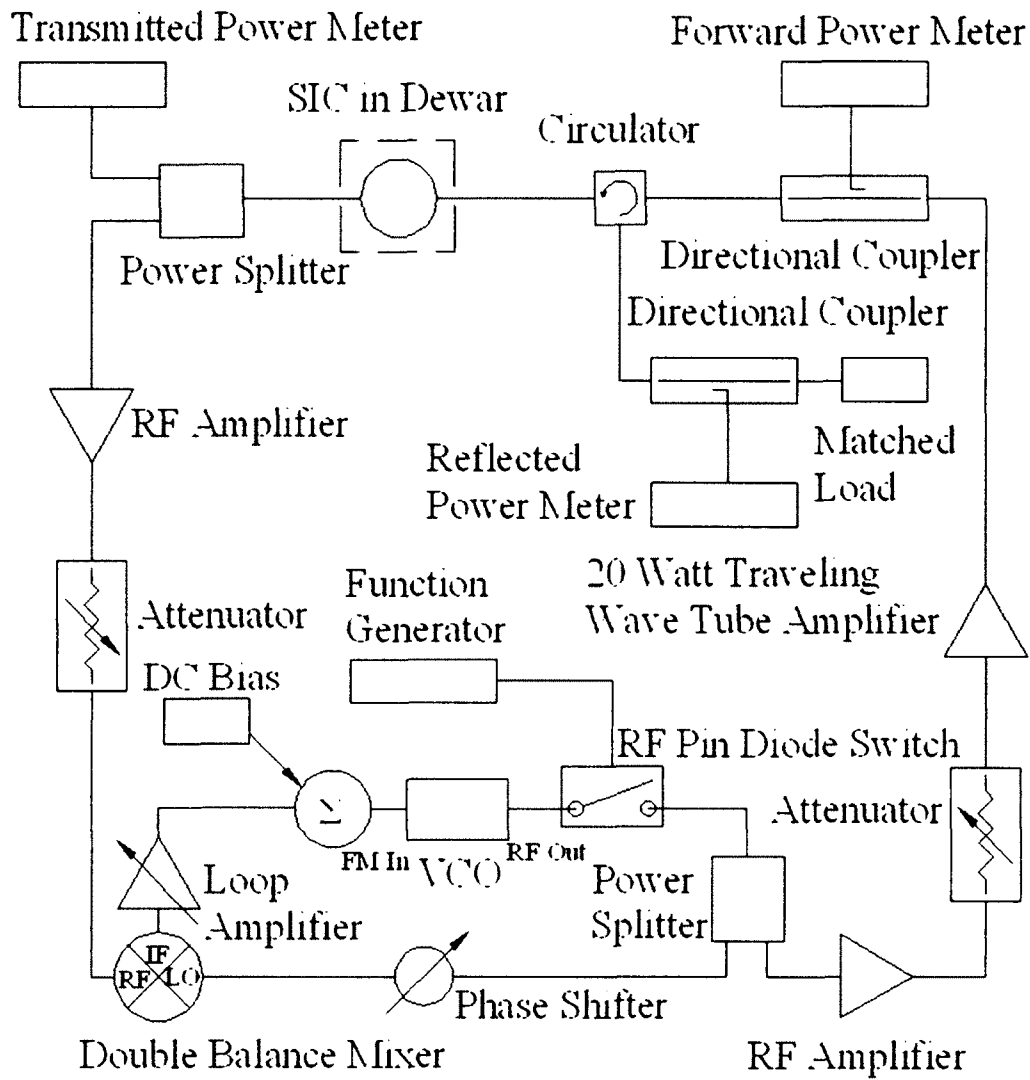


Figure 4.9. RF control circuit for SIC system.

## **CHAPTER 5**

# **SRF Surface Impedance Characterization System – Calorimeter Portion**

### **5. 1. Introduction**

Low temperature calorimeters are normally used to measure the chemical thermodynamic properties of molecular systems [52] and to measure the specific heat of different materials [53], dealing with heat power in mW range. In this paper, two calorimeters that cover the whole thermal range of interest for SRF materials, dealing with peak power from  $\mu\text{W}$  to more than one hundred W with sample temperature up to 40 K, will be described in detail. A new method, based on a power compensation technique to measure the induced heat will be introduced. Thermal response of these two calorimeters under CW operation will be simulated based on 1-D thermal simulation and compared with calibration experiments. The operating range will be determined based on both CW operation and pulsed mode operation analysis, and will be compared with the power range requested by SRF measurements. Factors that may affect measurement accuracy will be analyzed, and the power measurement accuracy



will be determined. Finally, sample temperature uniformity will be simulated based on a 3-D model, and the temperature measurement accuracy will be determined based on the simulation. All simulations and experiments were performed under equilibrium conditions with liquid helium bath temperature at  $2.00 \pm 0.01$  K.

## **5. 2. Description of Apparatus**

The SIC system, shown in Figure 4.1, consists of two major parts which come together at the sample under test. The RF portion shapes and controls the field presented to the sample surface. The calorimeter portion provides mechanical support to the sample and provides a controlled thermal conduction path from the sample to the liquid helium bath to offer a means of measuring the RF power dissipation on the sample. The design of the RF portion has been described elsewhere [15, 47, 48].

Heat generated by the RF field on the sample G or applied by a DC heater on the copper sample holder below sample G can be conducted away to the bath only via a stainless steel 304A/OFHC copper thermal path (K in Figure 4.1), an OFHC copper ring, followed by another stainless steel 304A/OFHC copper thermal path K. The calorimeter version with stainless steel 304A insulators is suitable for high precision low power measurements, and the one with OFHC copper insulators is the high power version. Each calorimeter portion of the SIC system was brazed together with 35/65 Au/Cu alloy at  $1030$  °C and then welded to a 6 inch Conflat™ flange. Two Lakeshore Cernox® thermal sensors are used in the high power version, with one mounted on the back corner of the copper sample holder (O in Figure 4.1) and the

other mounted on a spring-loaded pin to directly measure the temperature on the back center area of the sample G (N in Figure 4.1). For high precision version, only one Lakeshore Cernox® thermal sensor, mounted on the back corner of the copper sample holder (O in Figure 4.1) is used. In the following paragraphs, if not specified, high power version is used as an example. To extend it to high precision version application, sensor O is used to function as both sensor O and sensor N in high power version.

The sample temperature is feedback-controlled by a 50  $\Omega$  ring heater (L in Figure 4.1) and sensor O. Two stainless steel spring-clips are screwed on the back of the sample holder to hold the heater L tightly to the sample holder. Apiezon® N grease is applied between the back surface of sample holder and heater L/sensor O, and also between sample G and sample holder/sensor N (for high power version only), to ensure good thermal contact. The cavity interior and calorimeter space are both evacuated. The cavity is otherwise immersed in 2 K liquid helium during normal operation. This configuration allows the sample temperature to be controlled independently of the cavity, ensuring the temperature-dependent properties of the Nb cavity and sapphire are not confused with temperature-dependent properties of the sample, and also enabling impedance characterization of higher- $T_c$  materials.

Sample G is clamped onto the sample holder using a stainless steel cap (H in Figure 4.1) with 6 aluminum bolts (J in Figure 4.1) and 1.7 N-m torque on each of them. The thermal contraction  $(L_{293}-L_0)/L_{239}$  of aluminum is 0.00415, larger than that of copper (0.00326) or stainless steel (0.00296), which assures good thermal contact

between sample G and sample holder while cooling down from room temperature to 2 K. G-10 washers (I in Figure 4.1) are used to thermally separate aluminum bolts J from the stainless steel cap H so that thermal leak from the stainless steel cap H to the bath is minimized.

## 5.3. Measurement Method and Operating Range

### 5.3.1. Measurement Method

RF surface impedance may be calculated using the following expression,

$$Z_s = \frac{P_{rf}}{kB_{pk}^2} + i\omega\mu_0\left(\lambda_{ref} + \frac{f - f_{ref}}{M}\right) \quad (1)$$

The real part of  $Z_s$  is the surface resistance, and the imaginary part is the surface reactance.  $k$  and  $M$  are geometry-dependent coefficients which can be determined with RF simulation, and  $\omega$  is the resonant circular frequency.  $B_{pk}$  can be derived from RF measurements. To measure the RF induced heat  $P_{rf}$  under a certain sample temperature  $T$  condition, RF power is applied to the RF coupler (component C in Figure 4.1) and field is resonantly built up inside the Nb cavity (component D in Figure 4.1). RF induced heat  $P_{rf}$  is generated on the sample surface. The sample temperature is feedback-controlled by heater L and Sensor N with temperature set point at  $T$  using Lakeshore™ temperature controller 332. While under equilibrium, the voltage and current from heater  $V_{heater}$   $I_{heater}$  and sample holder temperature  $T_{holder}$  are measured using two Keithley® 2000 multimeters and a Lakeshore™ temperature controller 332. Next, with RF off, the sample holder temperature is feedback-controlled by heater L and sensor O with temperature set point at  $T_{holder}$ . While under equilibrium,

the voltage and current from heater  $V_{heater2}$   $I_{heater2}$  are measured and RF induced heat is calculated from the power difference:  $P_{rf} = V_{heater2} \times I_{heater2} - V_{heater1} \times I_{heater1}$ . This is so called power compensation technique. The surface reactance is calculated from the dependence of the RF resonant frequency on sample temperature while cavity temperature remains constant.

### 5.3.2. Thermal Path Simulations and Measurements

The calorimeter portion of the SIC system can be modeled as a simple 1-D system, shown in Figure 5.1.

The temperature on the sample holder may be calculated from:

$$\int_{T_{bath}}^{T_{holder}} k(T) dT = \int_0^{L_1} \frac{P}{S_1} dx + \int_0^{L_2} \frac{P}{S_2} dx \quad (2)$$

$T_{bath}$  is the liquid helium bath temperature.  $T_{holder}$  is the equilibrium temperature of the sample holder.  $k(T)$  is the thermal conductivity of the thermal insulator, which can be found from reference [54].  $L_1$  and  $L_2$  are the lengths, and  $S_1$  and  $S_2$  are the cross section area of the upper and lower thermal insulators shown as K in Figure 4.1.  $P$  is the sum of heat generated by the RF field on the sample G ( $P_{rf}$ ) and applied on the DC heater L ( $P_{heater}$ ).

Using this model, the calculated  $T_{holder}$  under different  $P_{rf}+P_{heater}$  for both high power and high precision versions are plotted as red dots on Figure 5.2 and Figure 5.3, respectively.

Calibration experiments were performed using a 50 mm diameter, 3 mm thick Nb disk sample with heater and sensor attached to the top surface, the area normally

exposed to RF field, with heater right in the center and sensor 1 cm away from the center. Power was separately applied to the heater on the sample and to heater L. The temperature of the sample holder was measured from sensor O. The results for the high power version are shown in Figure 5.2 and for the high precision version are shown in Figure 5.3.

### 5.3.3. Pulsed Mode Operation

In both high precision and high power calorimeters, pulsed mode RF operation is preferred for high field measurements to reduce the average RF induced heat on the sample. DC heater power compensation is then used to measure the average RF induced heat. For the high precision calorimeter, working in pulsed mode is essential since the continuous wave mode is operationally limited to less than 4 mT magnetic flux at 2.2 K for BCS-limited Nb with bath temperature at 2 K because the high thermal impedance of the stainless steel pushes the sample temperature up with less than 1 mW of RF heating.

Presently, the RF time constant of the  $TE_{011}$  cavity is 0.2 ms. In pulsed mode, the time length of RF “on” ( $t_1$ ) should be long enough to allow the field to be built up. The field can reach 95% of its maximum within 0.6 ms. A 2 ms (or more) time length is chosen for RF “on” to ensure the field reaches maximum and keep it for another 1.4 ms. The thermal time constants of both calorimeter systems are more than 10 s. The time length of RF “off” ( $t_2$ ) for pulsed mode operation must be short enough to keep the sample temperature adequately stable. We use  $t_2 < 0.2$  s to ensure that the temperature difference between sample and bath is adequately stable to be used for

average heat flow measurements. The duty factor ( $D_t = t_1/(t_1+t_2)$ ) of the SIC system in pulsed mode could then be 1% to 100%.

With a square wave transistor–transistor logic (TTL) control signal, the forward RF power will also be square wave modulated, but the stored energy will have exponentially rising and falling edges. The RF induced heat is proportional to the transmitted power, assuming linear losses. Since  $t_1, t_2 \gg \tau$ , the average RF induced heat over one duty cycle  $P_{rf-ave}$  will be:

$$P_{rf-ave} = \frac{\int_0^{t_1} P_{rf-max} (1 - e^{-t/\tau}) dt + \int_{t_1}^{t_1+t_2} P_{rf-max} e^{-t/\tau} dt}{t_1 + t_2} \approx P_{rf-max} \cdot D_t \quad (3)$$

The average RF induced heat can be calculated from the maximum RF induced heat times the duty factor. Surface resistance may then be calculated from:

$$R_s = \frac{P_{rf-max} \cdot D_t}{kB_{pk}^2} \quad (4)$$

While in CW mode,  $D_t = 1$  and the above equation becomes the real part of equation (1).

### 5.3.4. Operating Range

The sample temperature, starting at a temperature slightly higher than the 2 K liquid helium bath temperature at 2.1 K and may be raised arbitrarily to 10 K or 40 K to measure Nb samples or samples with higher critical temperature like MgB<sub>2</sub>. Using Nb as an example, with  $10^{-7}$ – $10^{-3} \Omega$  surface resistance under RF magnetic field at 0.5~200 mT, the RF induced heat ranges from 0.1 mW to 22 W. The power range requested by SRF sample characterization is plotted in Figure 5.4 using dotted lines.

Based on the experimental results in Figure 5.2 and Figure 5.3, and the analysis on pulsed mode operation, the operation range for both version calorimeters are also determined and plotted in Figure 5.4.

With a helium bath temperature of 2.00 K, the heat needed for sample temperature increase to 2.10 K is 0.17 mW for the high precision calorimeter. With 0.1 mW RF induced heat, 0.07 mW power is required from heater L to compensate the power required for sample holder temperature increase to 2.10 K for the high precision calorimeter. With a 30 mW CW power, or 1% duty factor pulsed mode with a 3 W peak power, the sample temperature of high precision version would go up to 10 K. For high power calorimeter, a 0.15 W average power is needed for sample temperature increase to 2.50 K, with a temperature increase of 5 mK at the sample holder. With the pulsed mode operation of RF system, the maximum RF induced heat may be as high as 15 W at 2.50 K for the high power version with 1% duty factor to cover measurements under high magnetic fields and low sample temperatures. With a 22 W average power, sample temperature for the high power version will go up to 24 K. Similar analysis could be done for liquid helium bath at 1.8 K and for other SRF materials, with the conclusion that these two calorimeter systems cover the whole thermal range of interest for SRF materials.

#### **5. 4. Power Measurement Accuracy Analysis**

- Thermal leak from instrumentation wires

Some power may flow out to the liquid helium bath via unintentional paths like the wires for heater and sensors.

For both heater and sensors, four-wire sensing is used to precisely measure the resistance and power. Wires for heaters with  $1.5 \times 10^{-3} \text{ cm}^2$  cross section area, and for sensors with  $4 \times 10^{-4} \text{ cm}^2$  are used, with the same length at 40 cm. Considering the thermal conductivity of 30 RRR Cu at less than 0.1 Watt/cm/K [54], the total thermal conductance of wires is 15  $\mu\text{Watt/K}$ .

The designed thermal path consists of two rings, one with 4.7 cm inner diameter, 5.1 cm outer diameter and 2.2 cm in height, and another with 7.0 cm inner diameter, 7.3 cm outer diameter and 1.4 cm in height. The total thermal conductance of the thermal path is 1.5 mW/K for high precision version and 2.96 Watt/K for high power version, more than 100 times the thermal conductance of all wires. The thermal conduction loss from wires is negligible.

- Thermal leak from radiation

The thermal radiation from the sample, assuming it is perfect black body, is  $P = \sigma AT^4$ .  $\sigma$  is Stefan-Boltzmann constant,  $A$  is the sample surface area.

Even in the extreme condition of 40 K sample temperature operation, thermal radiation is only about  $3 \times 10^{-4}$  Watt for both high precision version and high power version. The thermal radiation is less than 0.1% of the RF induced/heat power required for the sample to stay at the same temperature condition, which is calculated to be 0.73 Watt for high precision version based on the method above. For high



power version, this percentage is extremely small. The thermal radiation leak can be ignored in both versions.

- Additional heat from thermal sensors

The drive current for the thermal sensors induces a small amount of heat. These current are  $1\ \mu\text{A}$  and  $100\ \mu\text{A}$  for Cernox® cx-1050 ( $\sim 10000\ \Omega$  at 2 K) and cx-1010 ( $\sim 200\ \Omega$  at 2 K) sensors. The power thus generated is in tens of nW range for cx-1050 and in several  $\mu\text{W}$  range for cx-1010. The driving power of thermal sensors is thus negligible compared with the RF induced power.

- Control and measurement accuracy on heater power

The control accuracy of power source in Lakeshore™ temperature controller 332 is better than  $1\ \mu\text{W}$  [55]. The measurement accuracy on heater voltage and current is better than 0.1 mV and 0.01 mA [56]. The control and measurement accuracy on heater power is thus better than 1%.

- Experimental results on power accuracy

The power measurement error of this power compensation technique may be estimated based on the results of the calibration experiments in Figure 5.2 and Figure 5.3. With constant temperature on sensor O, this relative error is the difference between the power from heater L and from the heater on sample, divided by the power from heater L. The calibration experiments indicate this error to be within 2.7% for high power version with sample temperature up to 24 K and within 1.2% for high precision version with sample temperature up to 10 K. This accuracy is comparable to

the low temperature calorimeters for specific heat measurement, which normally give errors from 1% to 6% [53].

## **5. 5. Temperature Measurement Accuracy Analysis**

In our application, the RF induced power is strongly related to the SRF sample temperature, especially the sample temperature in the center area [15]. To evaluate the temperature uniformity on the sample surface, the thermal contact resistance between the sample and sample holder has been experimentally characterized and applied to an ANSYS<sup>TM</sup> model. The temperature distribution on sample surface was then modeled for both calorimeter versions. Based on the simulation results, the temperature differences between the area that exposed to high magnetic flux density on sample top surface and the point that the sample temperature has been measured have been evaluated to get the temperature measurement accuracy.

### **5.5.1. Thermal Contact Resistance Between Sample and Sample Holder**

As discussed above, thermal contact resistance between sample and sample holder (E in Figure 4.1) does not affect the power compensation measurement. However, this resistance will affect the temperature distribution on the sample under different heat flow conditions. This resistance is affected by the pressure applied on sample and sample holder, and also some other effects such as surface roughness of the sample and sample holder, the interstitial material applied between them, and

potential surface deformation during cool down. In our case, a 1.7 N-m torque has been applied to each aluminum bolt to get repeatable 8900 N total force on sample and  $4.4 \times 10^6$  Pa pressure between sample and sample holder for every test. The resistance was further lowered with Apiezon® N grease applied and additional pressure from the contraction of aluminum bolts during cool down. Its value was estimated based on the experimental results from the high power calorimeter, shown in Figure 5.2, which shows the temperature on the top surface of the sample, on the bottom surface of the sample (Sensor N), and on the bottom of sample holder (Sensor O) while applying different heater power on the sample top surface. The temperature difference between sensor N and O allows one to calculate the thermal contact resistance between the sample and the sample holder under the conditions mentioned above.

Figure 5.5 shows the observed thermal contact resistance  $R$  versus temperature  $T$ . The results are fitted with the function  $1/R = 4.44 \times 10^5 \times T - 5.08 \times 10^5$  with  $R$  in cm-cm-K/W and  $T$  in K.

### **5.5.2. Power Distribution on Sample**

In the SIC system, the RF power dissipation is confined within the central 2 cm dia. area of the sample. Based on the RF simulation using Microwave Studio™ [11], the normalized RF induced power distribution on sample is plotted in Figure 5.6, assuming uniform RF surface resistance on sample. The high power region, with power density higher than 60% of the maximum value on the sample, has an area of  $0.8 \text{ cm}^2$ .

### 5.5.3. Temperature Distribution on Sample

An ANSYS™ model, shown in Figure 5.7, has been constructed to simulate the temperature distribution on the sample, using the cryogenic thermal conductivity data of Nb, OFHC Cu and Stainless Steel 304A from reference [54] and the thermal conductivity data of the interlayer between sample and sample holder from above.

The initial temperature applied on this model is 2.000 K, which is our customary liquid helium bath temperature. The temperature on the bottom ring of this model has been set to be constant at 2.000 K since it is exposed to liquid helium, while the rest of the surface area on this model is under vacuum. The heat flux distribution plotted in Figure 5.6 has been applied to a center portion of the sample top surface with 2 cm in diameter, which is the area that exposed to RF field.

The simulation results of the temperature distribution on the sample surface for the high precision and high power versions are shown in Figure 5.8. In the high precision version within the high power dissipation region shown in Figure 5.6, the temperature variation is less than 10 mK under 30 mW RF power and 9.112 K peak sample temperature. For the high power version calorimeter the temperature distribution is less uniform. Within the high power dissipation region, the temperature variation is within 0.4 K under 2.2 W RF power and 7.25 K peak sample temperature. With a smaller RF power of 0.03 W, the peak sample temperature is 2.26 K, with a 10 mK temperature variation in the same region. The simulation result for the high power version calorimeter deviates from the experimental result (line 1) shown in Figure 5.2 within 1 K since in the simulation the power distribution condition differs

from that in the experiment. Simulating a uniform power distribution on the central 2 cm dia. area yields results quite close to the calibration test measurements.

#### **5.5.4. Temperature Measurement Accuracy**

For the high precision version, the sample temperature is measured from sensor O. Figure 5.9 shows the measurement error of the sample temperature under different equilibrium sample temperatures. This error is calculated from the temperature difference between sample top surface and sample holder for the high precision version while power was separately applied to the heater on the sample top surface and heater L, shown in Figure 5.3. From Figure 5.9 one observes that the temperature difference between sample top surface and sample holder bottom surface, is within the accuracy of Lakeshore Cernox® sensor at  $\pm 5$  mK [57]. Based on the above ANSYS™ simulation, the temperature of the bottom of sample holder, measured from sensor O, is 30 mK lower than the highest temperature on sample top surface at 9.112 K with 30 mW power. A similar simulation with 0.1 mW power and 2.195 K sample top surface temperature yields a temperature difference of only 4 mK. The temperature measurement accuracy ranges from 5 mK to 30 mK with sample temperature ranges from 2.2 K to 9.1 K.

For the high power version, the sample temperature is measured directly from the back center of the sample. This measured temperature is lower than the highest temperature on the sample top surface, with a value at 0.03 K and 0.18 K for highest temperature on the sample top surface at 2.26 K and 7.25 K, with the assumption that

all 0.03 W power and 2.2 W power, respectively, come from the sample top surface. This measurement error is caused by the relatively low thermal conductivity of Nb comparing with that of Cu, the material for thermal impedance in high power version. In the case that part of the power comes from the heater L,  $V_{heaterL}$  and  $I_{heaterL}$  in the power compensation measurement are not zero, this error is reduced. Further simulation with surface resistance varying with sample temperature gives an error additional to the above analysis within 10 mK for the high power version calorimeter with 2.2 W power.

## 5. 6. Summary

A power compensation technique has been established to measure RF induced power on 5 cm disk samples and applied to the high precision version and the high power version calorimeters for the SIC system in JLab to cover the whole thermal range of interest for SRF materials. Within this range, the error in power compensation measurement is less than 1.2% and 2.7% for the high precision and high power versions, respectively. The error in temperature measurement ranges from 5 mK to 30 mK, with sample temperature ranges from 2.2 K to 9.1 K for the high precision version, and ranges from 0.03 K to 0.18 K, with sample temperature ranges from 2.26 K to 7.25 K for the high power version. Ansys<sup>TM</sup> simulation shows a uniform temperature distribution on the high precision version, with 10 mK maximum temperature difference in the high power region for peak sample temperature at 9.1 K, and a reduced uniformity for the high power version, with this

value at 0.4 K for peak sample temperature at 7.25 K. All above measurements and simulations are done with liquid helium bath temperature at 2.00 K. Both versions have the ability to accept bulk superconductors and thin film superconducting samples with a variety of substrate materials such as Al, Al<sub>2</sub>O<sub>3</sub>, Cu, MgO, Nb and Si.

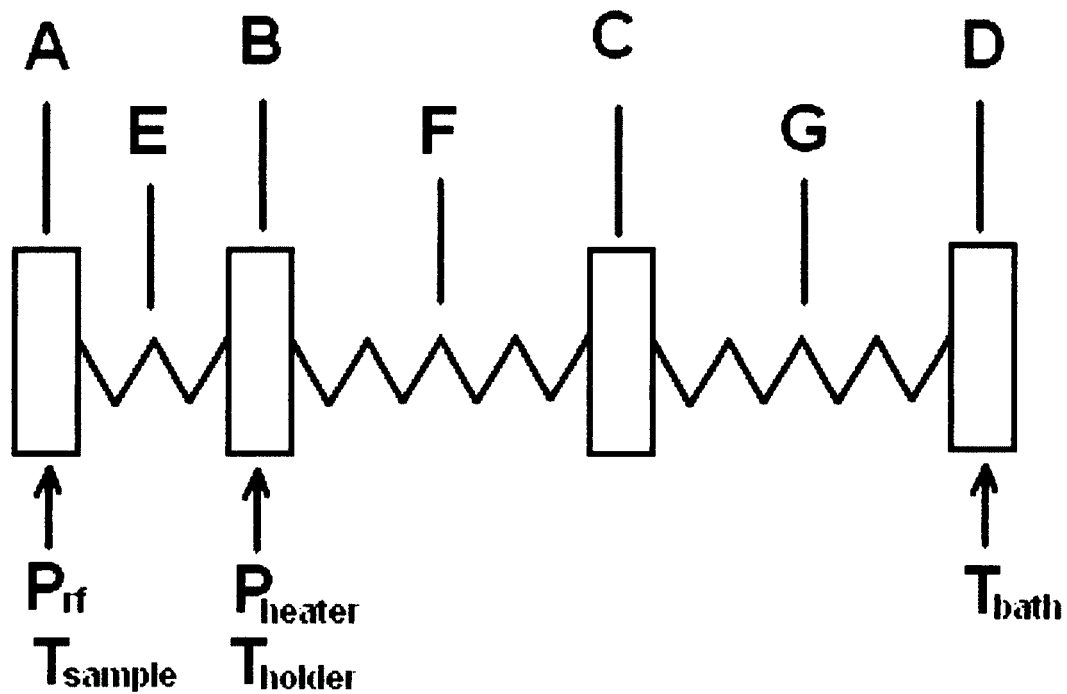


Figure 5.1. Simplified thermal model of calorimeter system. A. Sample, B. Sample Holder, C. OFHC copper ring, D. Liquid helium bath, E. Thermal contact impedance between sample and sample holder, F. Thermal impedance of the upper insulator, G. Thermal impedance of the lower insulator.



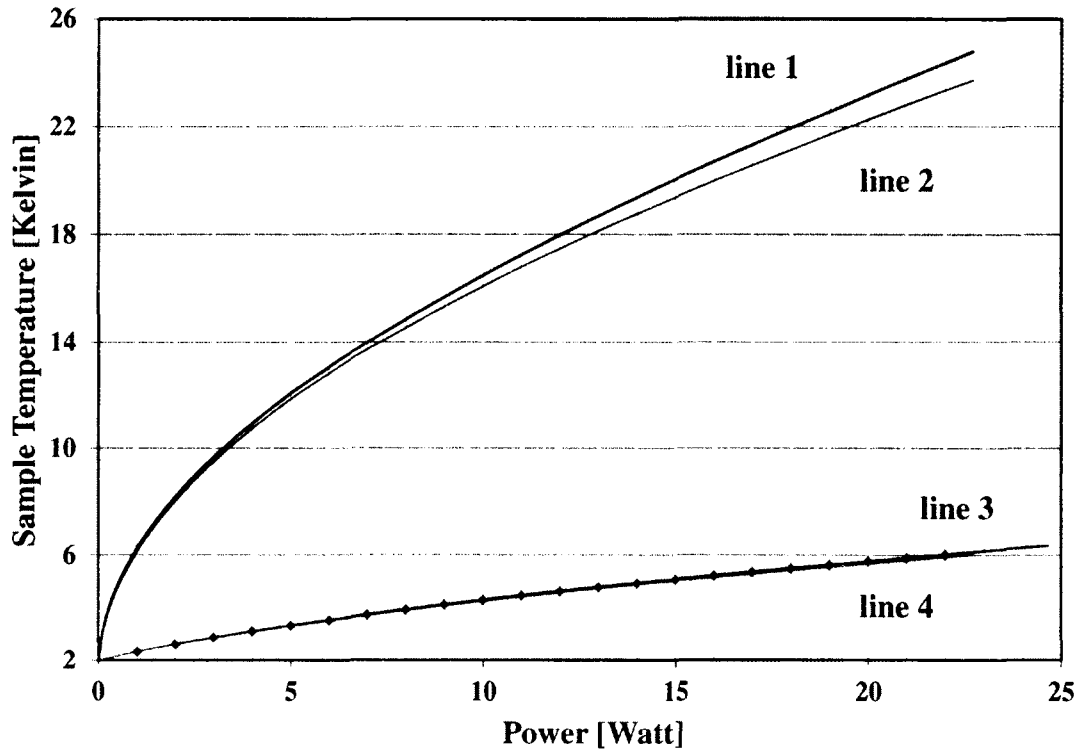


Figure 5.2. For the high power calorimeter, temperature on the top surface of sample (line 1), on sensor N (line 2) and on sensor O (line 3) shown in Figure 4.1 as a function of heater power on the top surface of sample, with temperature on sensor O (line 4, shorter than line 3) as a function of heater power from heater L. Red dots show the calculation results based on the 1-D model.

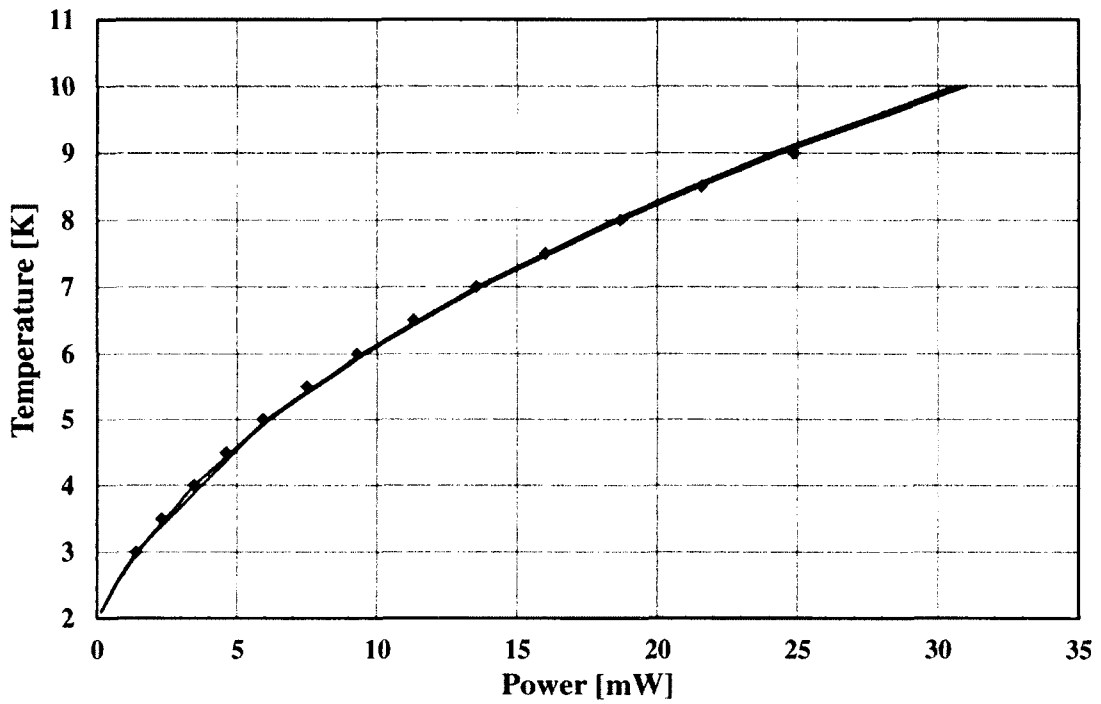


Figure 5.3. For the high precision calorimeter, temperature on the top surface of sample (green line), on sensor O shown Figure 4.1 as a function of heater power on the top surface of sample (orange line), with temperature on sensor O as a function of heater power from heater L (blue line). The above three lines are overlapped together. Red dots show the calculation results based on the 1-D model.

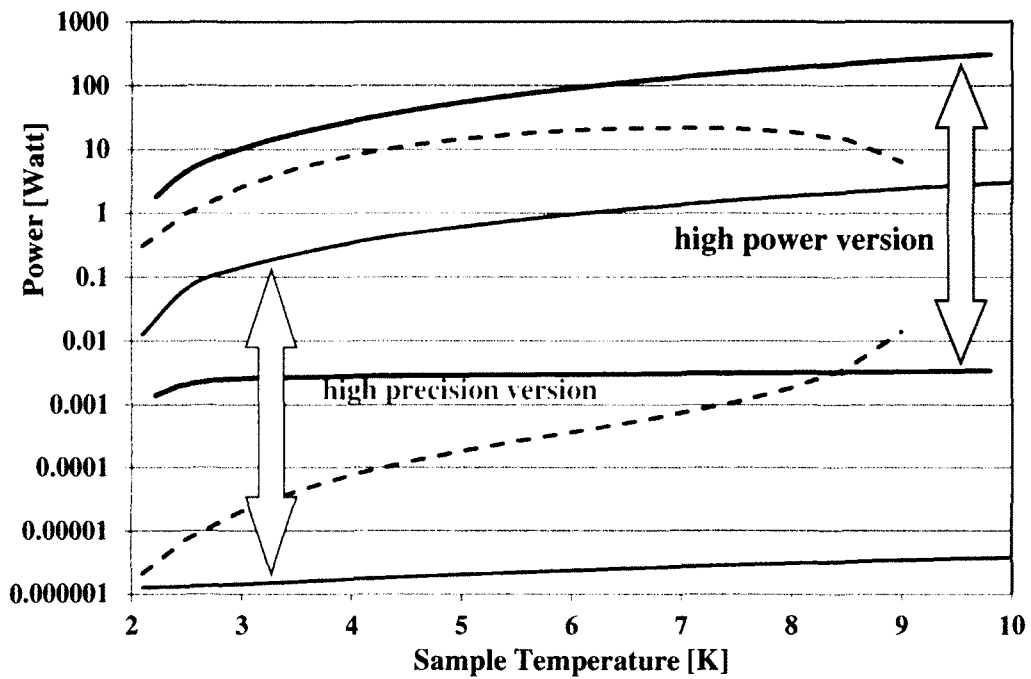


Figure 5.4. Power range requested by SRF sample characterization as a function of sample temperature (blue dotted line). Power range for high precision (red) and high power (black) version calorimeters as a function of sample temperature.

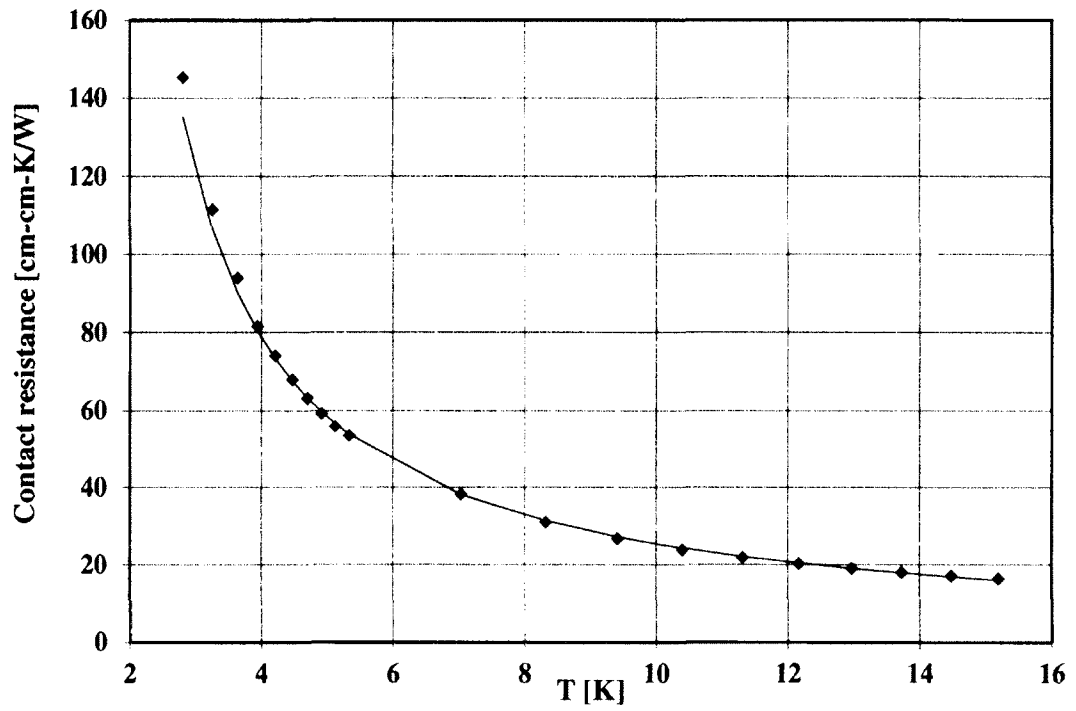


Figure 5.5. Thermal contact resistance between sample and sample holder (red dots). Blue line is the fitting.

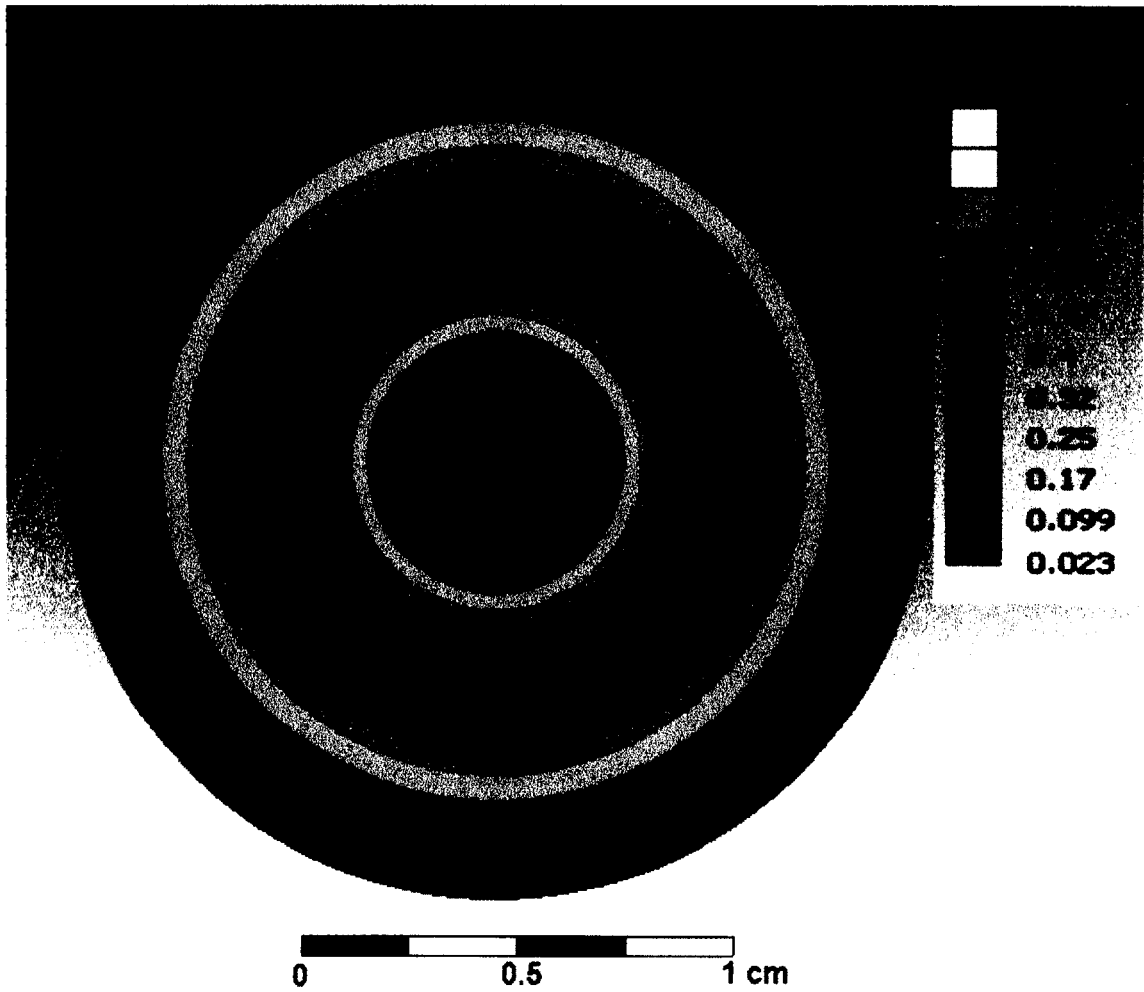


Figure 5.6. RF induced heat distribution on sample.



Figure 5.7. Ansys™ model of calorimeter system with materials: ■ (dark blue) Nb, ■ (orange) Cu, ■ (gray) Stainless steel/Cu for high precision/high power version, ■ (purple) Interlayer between the sample and the sample holder.

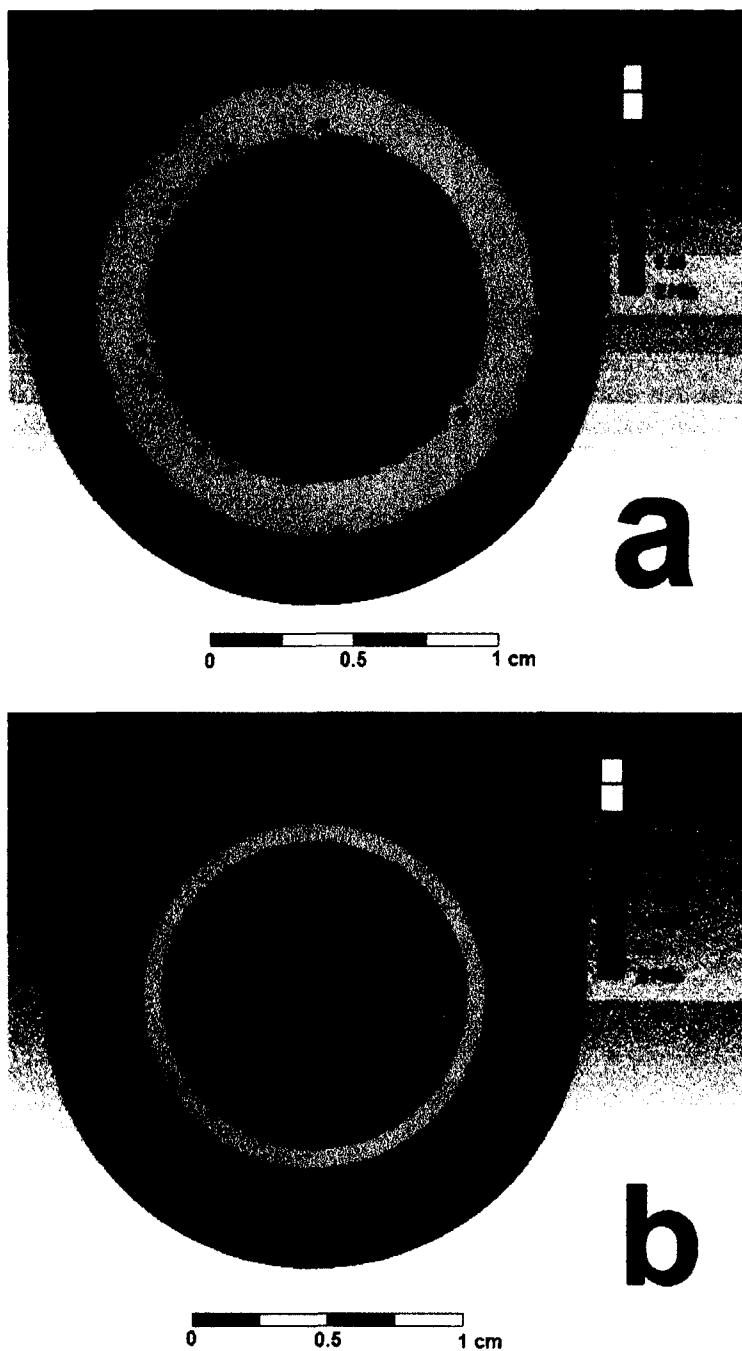


Figure 5.8. Temperature distribution on the 2 cm dia. center area of sample top surface for (a) high precision calorimeter with 30 mW power and (b) high power calorimeter with 2.2 W power, both powers are applied to RF-exposed central area.

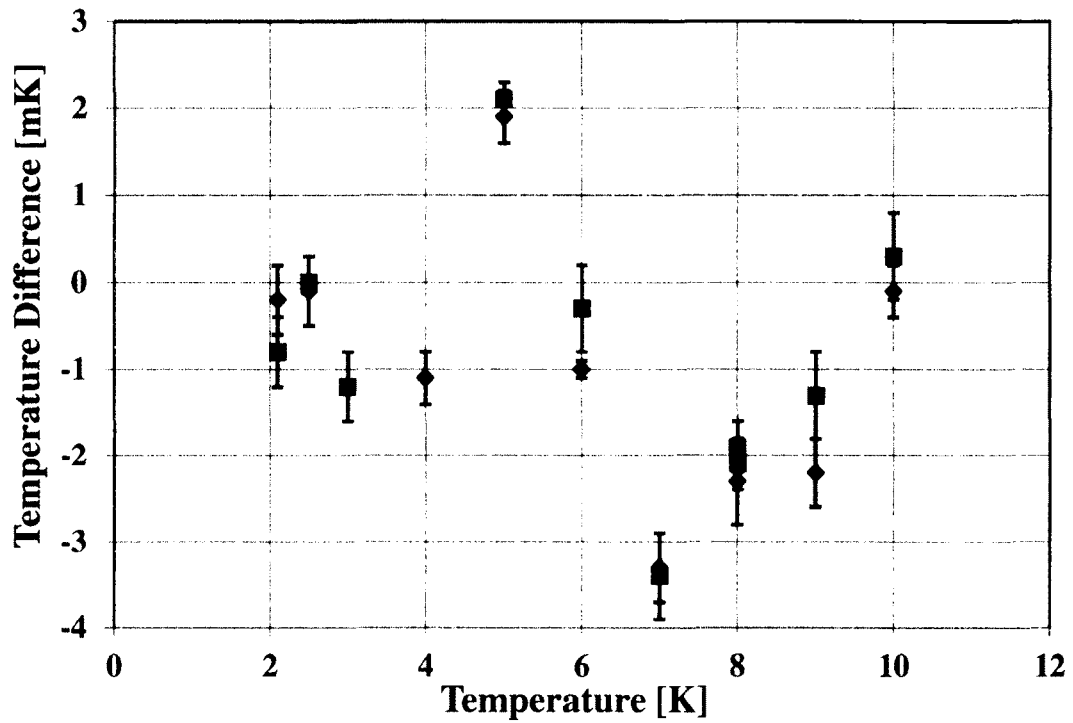


Figure 5.9. Temperature difference between sensor N in Figure 4.1 and the sensor on top of sample G versus temperature on top of sample G, with power on heater L (blue dots) and with power on the heater on sample (read dots) for high precision version calorimeter system.



## CHAPTER 6

# SRF Surface Impedance Characterization System - Data Acquisition and Analysis

### 6.1. Surface Impedance Characterization

#### 6.1.1. Calculation

As shown in Chapter 5, the surface impedance can be calculated from equation:

$$Z_s = \frac{P_{rf}}{kB_{pk}^2} + i\omega\mu_0\left(\lambda_{ref} + \frac{f - f_{ref}}{M}\right)$$

The real part is the surface resistance, and the imaginary part is the surface reactance.  $P_{rf}$  is the RF induced heat power,  $k$  and  $M$  are geometry-dependent coefficients, and  $\omega$  is the resonant circular frequency.  $P_{rf}$  is measured using the power compensation technique in Chapter 5.

#### 6.1.2. Surface Resistance

Equation (1) is used to derive the surface resistance:

$$P_{rf} = \frac{1}{2} \int R_s B^2(S) / \mu_0^2 dS \quad (1)$$

$B(S)$  is the magnetic flux density distribution on the sample. In the approximation of uniform  $R_s$  over the sample, this can be rewritten as:

$$P_{rf} = k R_s B_{pk}^2 \quad (2)$$

Where  $k$  is a modal geometry-dependent parameter and

$$k = \frac{1}{2} \int B^2(S) dS / (\mu_0 B_{pk})^2 \quad (3)$$

Under specific steady-state operating conditions, one may determine the resonant stored energy from RF power measurements. The ratio  $B_{pk}$  to  $\sqrt{U}$  is best established by available RF structure modeling codes. Stored energy may be calculated from equation (4):

$$U = 2 \times (P_f \mp \sqrt{P_r \times P_f}) \times \tau \quad (4)$$

$P_f$  is forward power,  $P_r$  is reflected power, with minus/plus for input coupler with under/over coupled,  $\tau$  is the decay time measured from the free decay of transmitted power.

Using Microwave Studio® (MWS) for such a calculation with a 0.01 cm gap between the cavity/sapphire and the sample surface, the values for  $k$  and  $B_{pk}/\text{sqrt}(U)$  given in Table 6.1 were obtained.

### 6.1.3. Surface Reactance

The resonant frequency of the  $TE_{011}$  mode of the cavity can be tuned by adjusting the gap between the cavity/sapphire and the sample. The ratio of the frequency change to the gap length is the mechanical tuning sensitivity  $M$ . The change of surface reactance, as the sample temperature is varied, is proportional to the change of penetration depth, which can be derived from changes of the resonant frequency with all other factors constant. The mechanical tuning sensitivity  $M$  is also used to do  $TE_{011}$  mode verification, the detailed analysis is in Section 4.2.6.

Since the resonant frequency is also sensitive to temperature and pressure changes external to the sample under test, stability is maximized by regulating the helium bath pressure to  $21.5 \pm 0.5$  torr while varying the sample temperature and using less than  $10 \mu\text{W}$  RF power for the reactance measurement.

## **6.2. System Measurement Range, Accuracy and Resolution**

### **6.2.1. System Measurement Range**

The high thermal impedance of stainless steel provides very good sensitivity to the thermal system. Combined with the Cernox® sensors, it enables detection of  $1 \mu\text{W}$  power applied on the sample/sample holder. This high thermal impedance, however, also constrains the stable heat load and thus limits the peak magnetic flux density supportable in CW measurements. In pulsed mode, the duty factor is set to be in 1% to 100% range, as described in 5.3.3. Figure 6.1 shows the projected measurement range of the present SIC system with high precision version calorimeter.

Solid lines show the anticipated conduction-limited operation at equilibrium temperature with bath temperature at 1.8 K. The high power version calorimeter with OFHC copper as the thermal insulator is being commissioned to overcome the conduction limitation and to cover the critical field of Nb from 2 K to 9 K at 7.5 GHz. The measurement range of SIC with high power version calorimeter is shown in Figure 6.2 with bath temperature at 2.0 K.

In order to approach 180 mT in CW mode, it will be necessary to improve the cavity's quality factor to  $10^8$  and use a 200 Watt RF source. A new version Nb cavity is developed, which is fully demountable from other components to enable surface processing that is routinely applied to SRF cavities in order to achieve a better quality factor. The achieved highest quality factor to date has been limited to  $3 \times 10^7$ .

With 22 watt and 300 watt available power from two TWT amplifiers, and assuming the quality factor is  $3 \times 10^7$  under higher field, the cavity has the ability to achieve peak magnetic flux densities up to 32 mT and 97 mT, respectively, without considering the power loss in the cable, shown in Figure 6.1 and Figure 6.2 with dashed lines. BCS resistance[58, 59] and lower critical field[59, 60] of  $\text{MgB}_2$ ,  $\text{Nb}_3\text{Sn}$  and NbN at 7.5 GHz and different temperature are labeled in Figure 6.1 and Figure 6.2 to illustrate potential applications of the SIC system.

### **6.2.2. System measurement accuracy**

From the previous section, the surface resistance can be determined from the expression:

$$R_s = \frac{P_{rf}}{kB_{ph}^2} = \frac{V_2 I_2 - V_1 I_1}{8.2 \times 10^6 (P_f \mp \sqrt{P_f P_r}) \tau} \quad (5)$$

$V_2$  and  $I_2$  are the voltage and current of the heater on the sample holder without RF power applied on the sample, while  $V_1$  and  $I_1$  are those with RF power. Two Keithley® 2000 multimeters are used to measure the voltage and current of heater power. Gigatronix® 8541C RF power meters with 80301A power sensors are used to measure forward, reflected and transmitted power. A Lakeshore® 332 temperature controller is used to control the sample temperature. It reads the temperature from a Cernox® sensor attached on the sample holder then via feedback controls the heater that is also attached on the sample holder. The accuracy of surface resistance measurements depends on the measurement accuracy of each term. Assuming uncorrelated standard errors, then:

$$\begin{aligned} \frac{\Delta R_s}{R_s} &= \frac{\Delta V_2 I_2 + V_2 \Delta I_2 + \Delta V_1 I_1 + V_1 \Delta I_1}{V_2 I_2 - V_1 I_1} \\ &+ \frac{\Delta P_f}{P_f} \frac{P_f \mp \frac{\sqrt{P_f P_r}}{2}}{P_f \mp \sqrt{P_f P_r}} + \frac{\Delta P_r}{2} \left( \frac{1}{\sqrt{P_f P_r} \mp P_r} \right) + \frac{\Delta \tau}{\tau} \end{aligned} \quad (6)$$

As discussed in Chapter 5, for high precision version calorimeter, the error in temperature measurement ranges from 5 mK to 30 mK, with sample temperature ranges from 2.2 K to 9.1 K, and for high power version calorimeter, this error ranges from 0.03 K to 0.18 K, with sample temperature ranges from 2.26 K to 7.25 K. The error in power compensation measurement is less than 1.2% and 2.7% for the high precision and high power versions, respectively. The error of peak RF field measurement, comes from the limited accuracy of RF power meters, is normally

within 5%. The error in surface resistance measurement is estimated to be within 13% for the SIC system with both version calorimeters.

### **6.2.3. System resolution**

With the BCS resistance of Nb at 7.4 GHz and 2 K of about 600 n $\Omega$ , the resolution of surface resistance measurements will be limited mainly by the RF measurements ( $\Delta P_f$  and  $\Delta P_r$ ) to about 5%, which is 30 n $\Omega$ . Using the Cernox® sensors, one can detect a 1 mK temperature variation. From the thermal analysis above, this temperature change typically corresponds to 1  $\mu$ W power change on the sample at 2 K and 6  $\mu$ W at 9 K. For other materials that have a lower BCS resistance than Nb, such as NbN and Nb<sub>3</sub>Sn, the resolution will be limited mainly by the calorimeter. Corresponding surface resistance resolution can be derived from the above formula. In a typical measurement with more than 5 mT applied magnetic flux density, the RF surface resistance resolution will be 1.1 n $\Omega$  at 2 K and 6.6 n $\Omega$  at 9 K. The fluctuation of sample temperature will also change the BCS resistance, within 4% for 10 mK fluctuation at 2 K sample temperature.

## **6.3. Automated LabView Program for Surface Impedance Measurement**

### **6.3.1. Proportional–integral–derivative (PID) Feedback Control on Temperature**

A LakeShore™ 332 temperature controller has been used to precisely control the sample/sample holder temperature. Automated PID with “zone tuning” has been applied to minimize the time needed for the system to stabilize at the setup temperature points. The detailed PID values for different temperature zone with temperature up to 50 K are listed in Table 6.2.

### **6.3.2. Automated LabView™ Program for Surface Reactance Measurement**

A fully automated LabView™ program has been written to get the surface reactance, along with loaded quality factor versus sample temperature, while cavity temperature stays at bath temperature, normally at 2 K. This program communicates with SIC instruments and automatically collect data from LakeShore™ 218 temperature monitor, LakeShore™ 332 temperature controller, two Keithley™ digital multi meters that measure the heaters’ current and voltage on copper plate, separately, and Agilent™ E5071C Network Analyzer with frequency ranges up to 9 GHz. All the data is saved in files formatted in the following way: C:\data\SIC\[yyyy-mm]\SICenvironment[yyyy-mm-dd-hhmm AM/PM].txt. The LakeShore™ 332 temperature controller uses automated PID control with zone tuning mentioned above. The flow chart of this program is shown in Figure 6.3 and the LabView™ front panel is shown in Figure 6.4.

### **6.3.3. Automated LabView™ Program for Surface Resistance Measurement**

This program helps to communicate with SIC instruments and collect data from LakeShore™ 218 temperature monitor, LakeShore™ 332 temperature controller, three Gigatronics™ 8541C single input digital power meters that measure forward, reflected and transmitted power, two Keithley™ digital multi meters that measure the heaters' current and voltage on copper plate, separately, and the Agilent™ E8663D signal generator. The above data is saved in files formatted in the following way: C:\data\SIC\[yyyy-mm]\SICenvironment[yyyy-mm-dd-hhmm AM/PM].txt. The LabView™ front panel is shown in Figure 6.5. Cooperation from Grigory Eremeev was highly appreciated during the development of these two LabView™ programs.

### **6.4. Data Analysis Based on BCS Surface Impedance Fitting**

A surface impedance fitting program was developed based on G. Ciovati's BCS surface resistance and reactance program SuperFit [26]. The graphic user interface of this program is shown in Figure 6.6. It uses one set of micro parameters to fit both surface resistance and surface reactance simultaneously. The input file format for this program is attached in Appendix F.

### **6.5. Measurements on Bulk Nb Samples**



### **6.5.1. Sample Preparation**

In order to test two bulk Nb samples, a 0.2 mm thick polycrystalline and large grain Nb coupons were brazed onto 2 mm thick Cu pieces using 50/50 Cu/Au alloy at 995 °C, and then flattened and etched 20 μm in a 1:1:2 buffered chemical polish (BCP) solution of HF (49% wt), HNO<sub>3</sub> (69% wt), and H<sub>3</sub>PO<sub>4</sub> (85% wt) at room temperature using setup in Figure 6.7. These Nb-on-Cu samples were mounted onto the Cu sample holder using Ga:In:Sn 1:1:1 in volume as the thermo-bonder without using the stainless steel cap.

### **6.5.2. Transition Temperature**

A vector network analyzer was used to measure the sample temperature dependence on the resonance frequency of the cavity, as well as its loaded  $Q$ . A transition temperature of  $9.25 \pm 0.05$  K was measured for the polycrystalline Nb, and  $9.26 \pm 0.01$  K for the large grain Nb sample.

### **6.5.3. Surface Reactance**

From the measurement of the dependence of resonance frequency of the cavity on the sample temperature, one can derive the change of surface reactance versus temperature. Surface reactances of polycrystalline and large grain Nb samples have been measured using the method described above and results are shown in Figure 6.8.

### **6.5.4. Surface Resistance**

Surface resistances of polycrystalline and large grain Nb samples have been measured using the method described in 6.1.2, with peak fields between 0.7 mT and 2.3 mT . Results are shown in Figure 6.9. Surface resistance measured here includes BCS resistance and residual resistance.

Measurement under pulsed mode with peak fields higher than 2.3 mT has also been performed. The results are shown in Figure 6.10.  $R_s$  measurements with peak surface magnetic field of up to 14 mT were obtained. This was limited by the available RF power source (22 watts).

### **6.5.5. Fitting Results**

Using SuperFit 2.0, least-squares multi-parameter fits with  $T_c$  fixed at 9.25 K for polycrystalline Nb and at 9.26 K for large grain Nb, and the BCS resistance portion of this fit are also shown in Figure 6.8 and Figure 6.9.

For the large grain Nb sample brazed on Cu substrate with  $T_c = 9.26$  K, the suggested parameters are  $\Delta/kT_c = 1.84$ , London penetration depth = 36 nm, coherence length = 33 nm, mean free path = 256 nm, penetration depth at 0 K = 45 nm and residual resistance =  $1.5 \mu\Omega$ .

For the polycrystalline Nb sample brazed on Cu substrate with  $T_c = 9.25$  K, the suggested parameters are  $\Delta/kT_c = 1.85$ , London penetration depth = 49 nm, Coherence length = 40 nm, mean free path = 397 nm and residual resistance =  $3.3 \mu\Omega$ .

One expects the surface resistance at 7.4 GHz of typical bulk niobium to be dominated by BCS to temperatures as low as 2 K. The fit for this data suggests a residual resistance as high as  $3.3 \mu\Omega$  and  $1.5 \mu\Omega$  for polycrystalline and large grain Nb, respectively, higher than expected. The high residual resistance may come from the complex procedure of the sample preparation described above.

Table 6.1. Key Parameters to Derive Surface Impedance

<b>Tuning Sensitivity <math>M</math> [Hz/nm]</b>	$k \left[ \frac{W}{\Omega T^2} \right]$	$\frac{B_{T*}}{\sqrt{U}} \left[ \frac{T}{\sqrt{J}} \right]$
-20	$3.7 \times 10^7$	0.359

Table 6.2. PID values for different temperature zone with temperature up to 50 K.

<b>Temperature Zone [K]</b>	<b>P</b>	<b>I</b>	<b>D</b>	<b>Power range</b>
< 2.3	0.2	20	100	Low
2.3~3.4	1.0	50	100	Low
3.4~9.9	5.0	50	100	Low
9.9~14.9	10.0	50	100	Low
14.9~19.9	20.0	50	100	Low
19.9~36.9	6.0	20	100	Medium
36.9~50	8.0	20	100	Medium

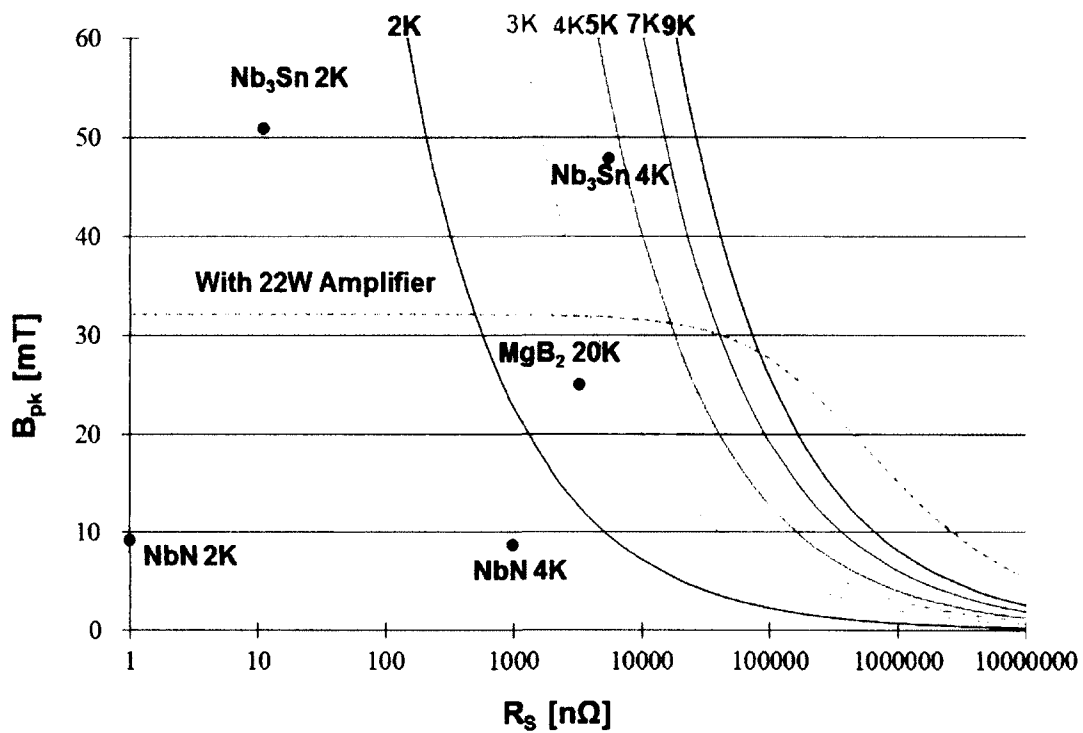


Figure 6.1. Measurement capability range of the SIC system. BCS resistance and lower critical field of MgB<sub>2</sub>, Nb<sub>3</sub>Sn and NbN at 7.5 GHz and different temperature are noted.

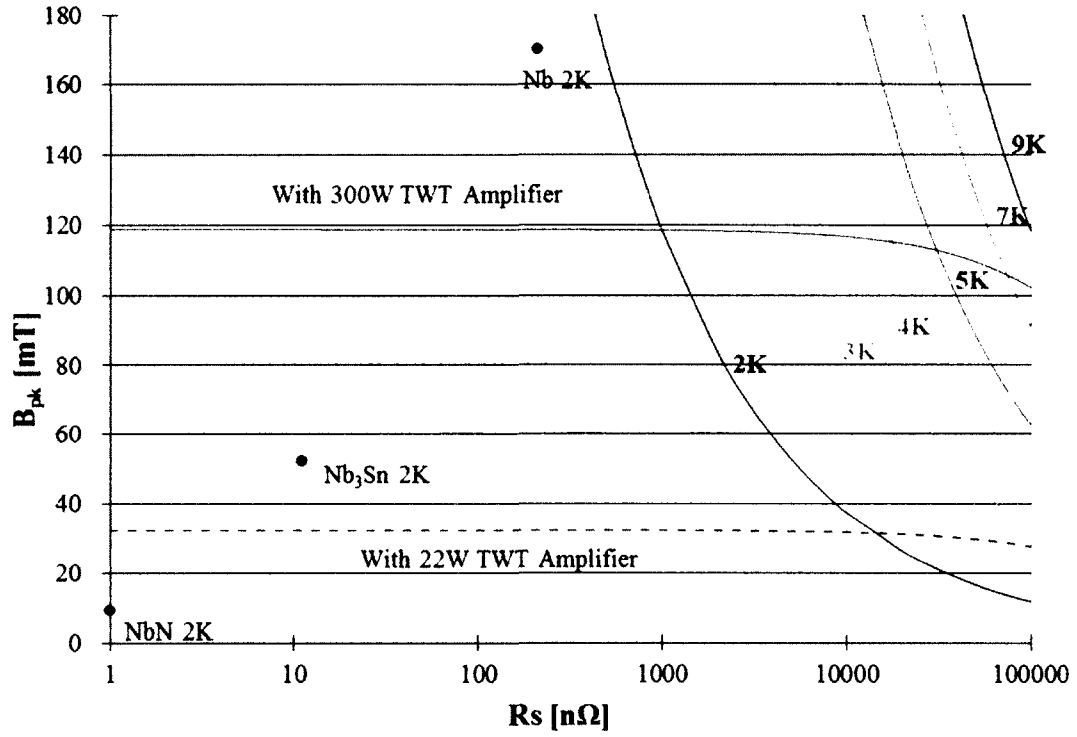


Figure 6.2. Measurement capability range of the SIC system. Materials of potential interest, power limits for two TWT amplifiers are noted.

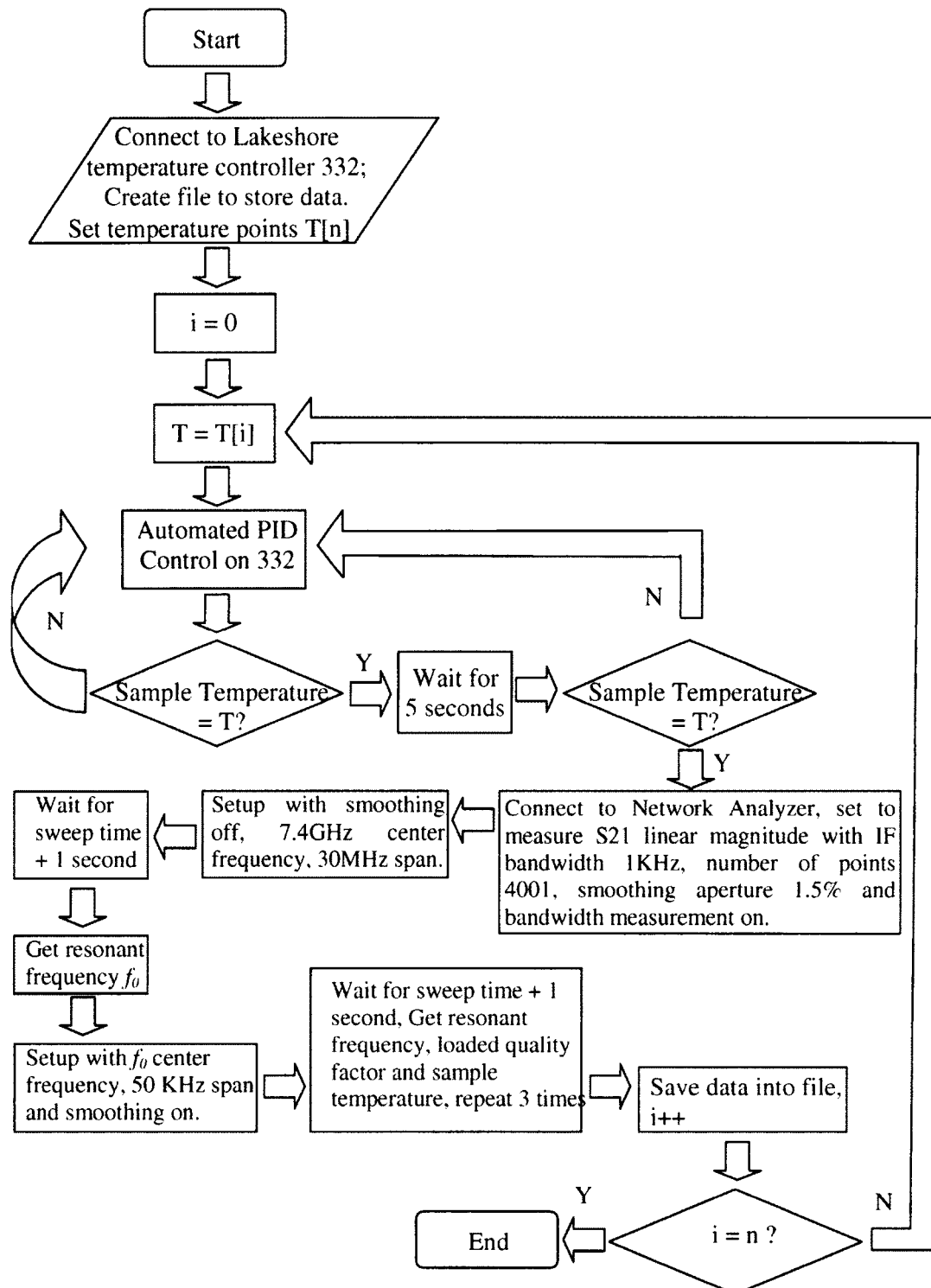


Figure 6.3. Surface reactance measurement flow chart.



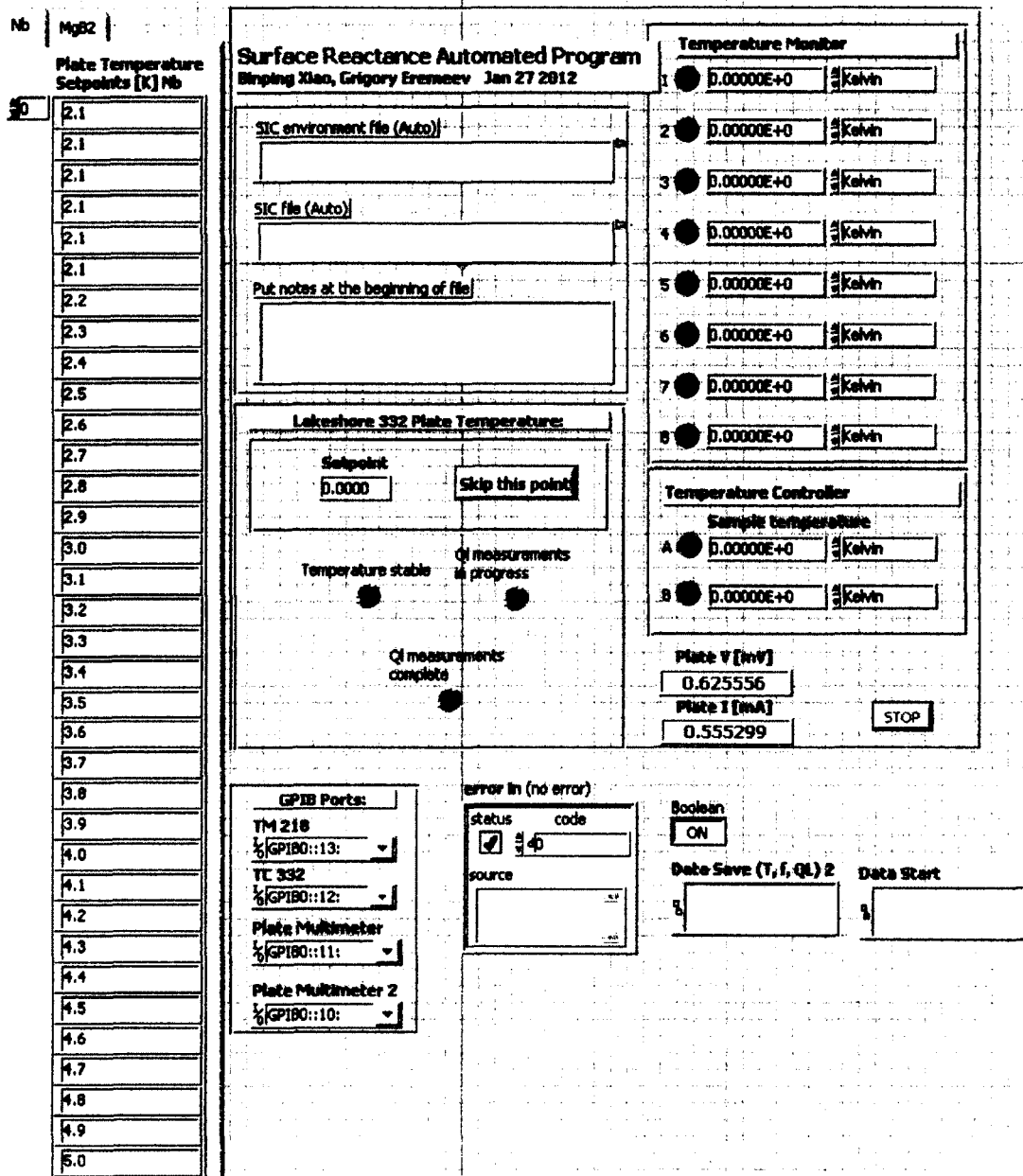


Figure 6.4. Surface reactance measurement LabView™ front panel.

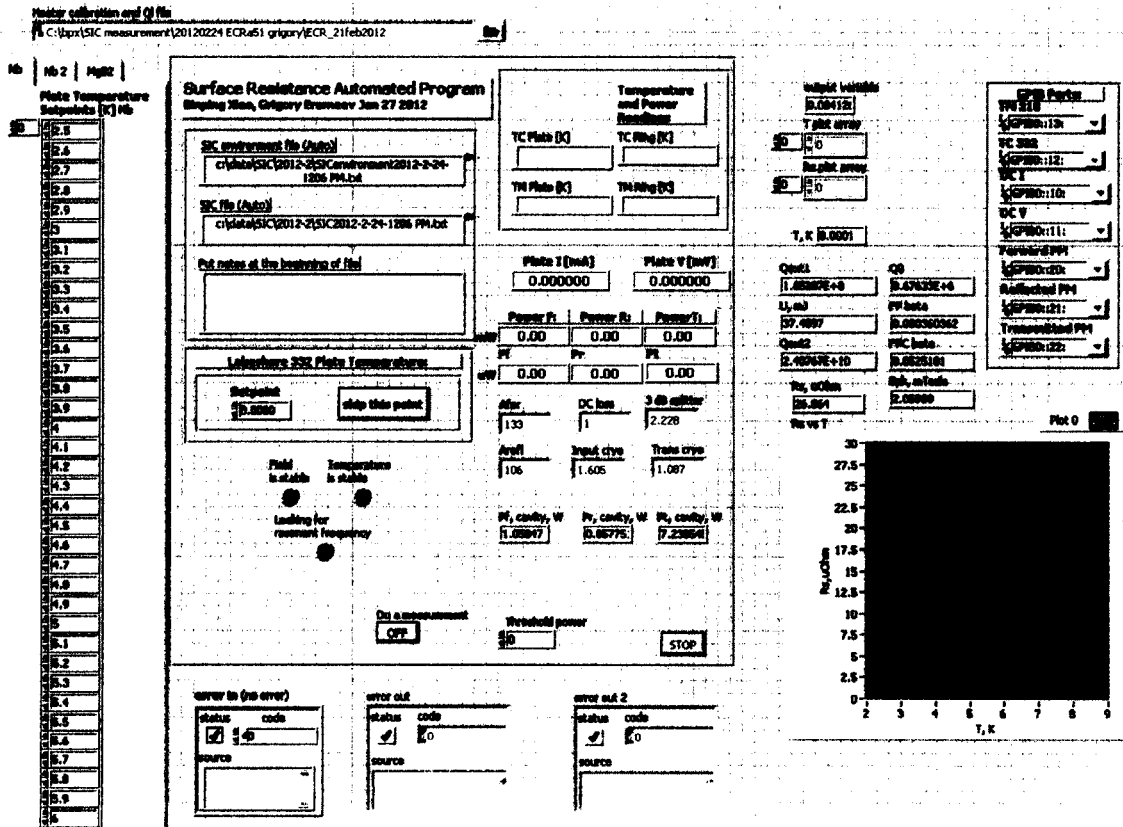


Figure 6.5. Surface resistance measurement LabView™ front panel.

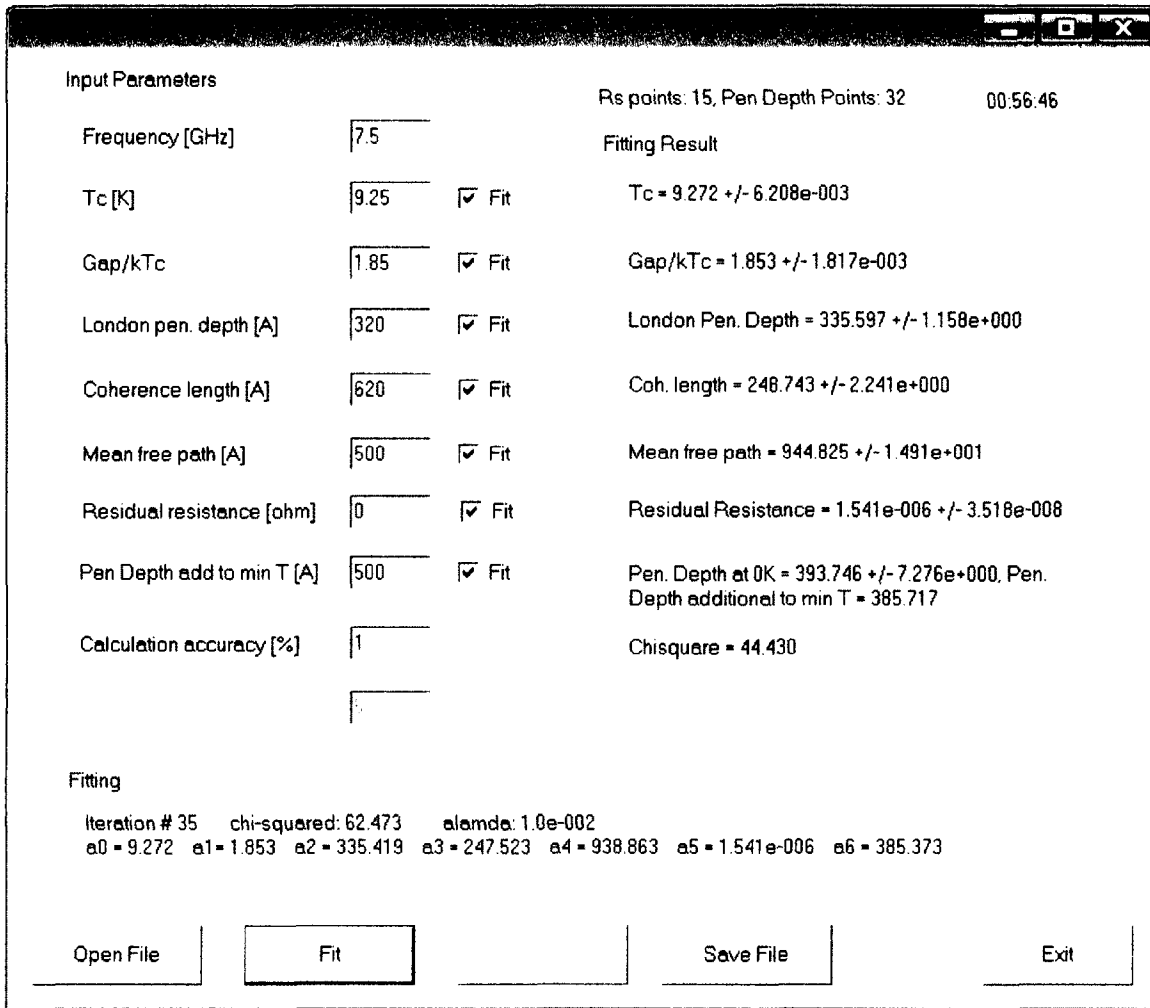


Figure 6.6. Graphic user interface of BCS surface impedance fitting program SuperFit2.0, revised from code SuperFit developed by G. Ciovati.

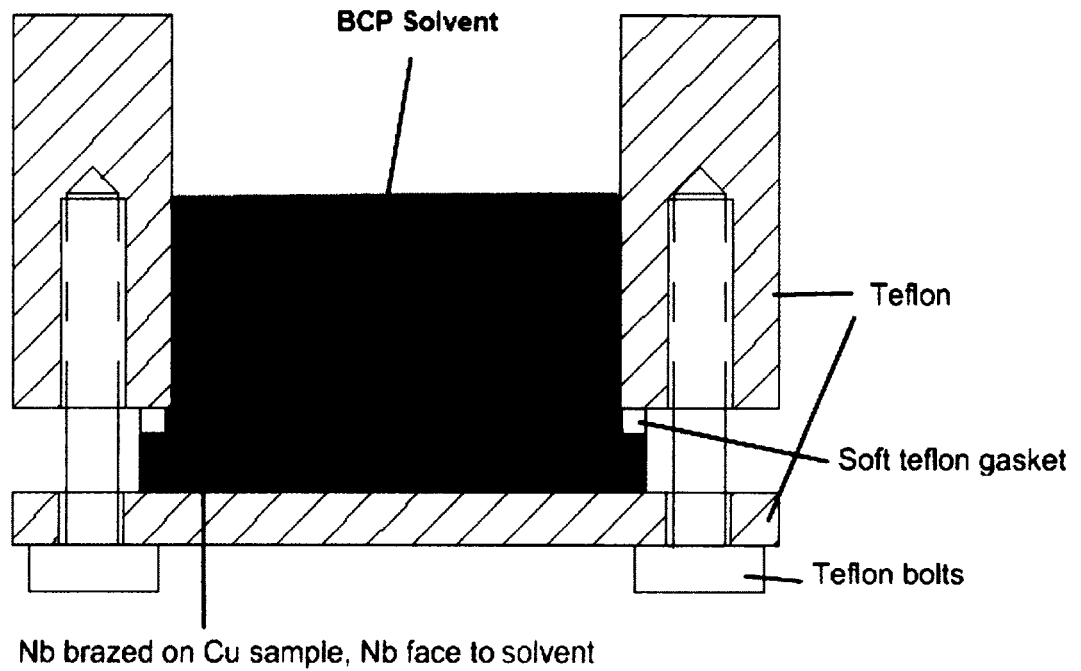


Figure 6.7. Setup for 1:1:2 buffered chemical polish (BCP) solution of HF (49% wt), HNO<sub>3</sub> (69% wt), and H<sub>3</sub>PO<sub>4</sub> (85% wt) on bulk Nb braze on Cu substrate.

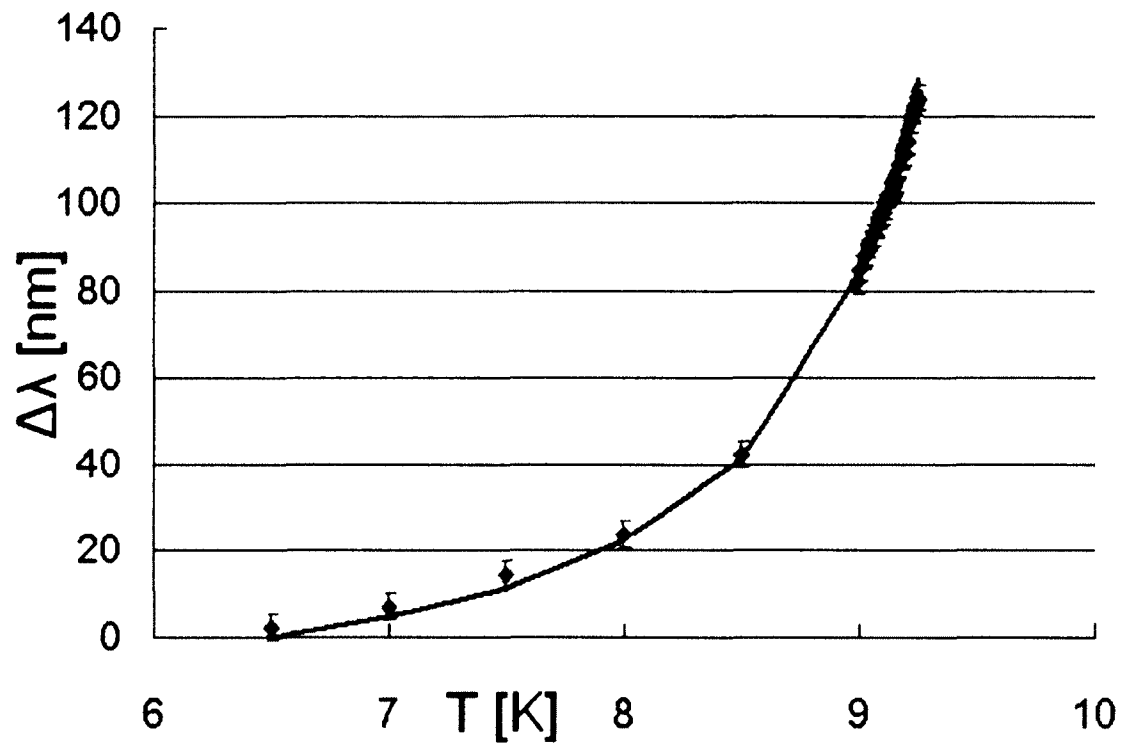


Figure 6.8. Penetration depth change versus sample temperature for a large grain bulk Nb sample brazed on a Cu substrate, solid line shows the BCS fit result.

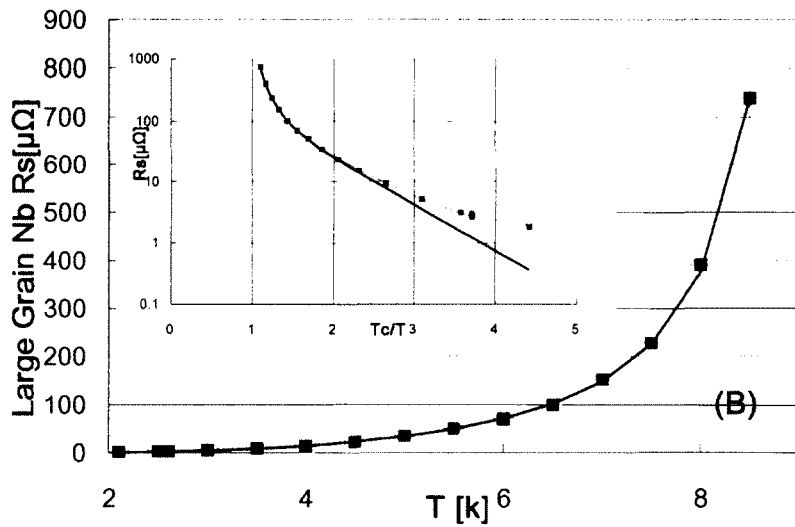
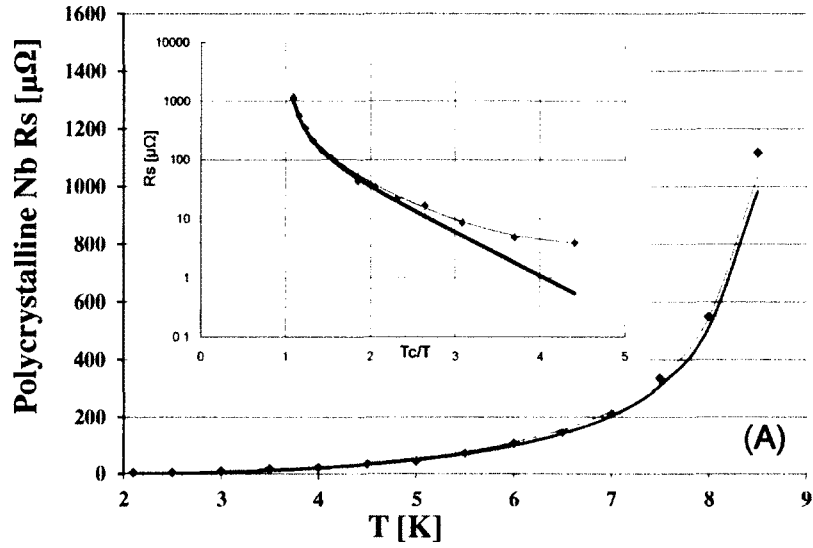


Figure 6.9. Surface resistance changes with sample temperature for polycrystalline (A) and large grain (B) Nb brazed on Cu substrate. ■ (red) Measured  $R_s$ , — (red) Theoretical value with BCS fit results. — (blue) BCS resistance.

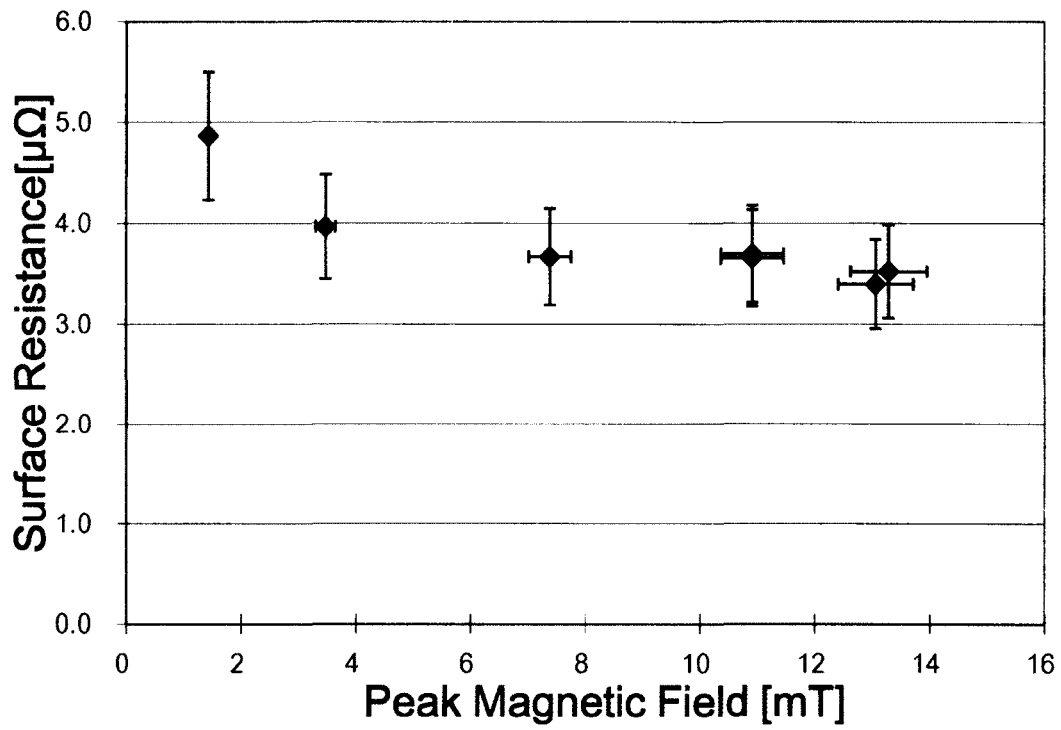


Figure 6.10. Surface resistance versus peak RF magnetic field at 2.5 K for a large grain bulk Nb sample brazed onto a Cu substrate.

## **CHAPTER 7**

# **SRF Surface Impedance Characterization on MgB<sub>2</sub> Thin Films**

### **7.1. Introduction**

SRF accelerating cavities for particle accelerators made from bulk niobium (Nb) materials are the state-of-art facilities for exploring frontier physics. The maximum accelerating gradient of Nb SRF resonant cavities has been pushed to 52 MV/m for a single-cell cavity with quality factor higher than  $10^{10}$  at 1.3 GHz and 2 K temperature [61], approaching the theoretical limit of Nb. Superconductors with surface resistance lower than, and superheating critical field higher than, those of Nb are of great interest for SRF applications. Magnesium diboride (MgB<sub>2</sub>), discovered to be a superconductor by Nagamatsu et al in 2001 [62], is under investigation for possible future use in SRF applications.

MgB<sub>2</sub> is a binary compound that contains hexagonal boron (B) layers separated by close-packed magnesium (Mg) layers. It has a high critical temperature,  $T_c$ , around



~39-40 K [63], nearly twice as high as the next highest binary superconductor's  $T_c$  (Nb<sub>3</sub>Ge at 23 K), which suggests possible applications at temperatures higher than 2 K, the current typical operation temperature of Nb cavities. MgB<sub>2</sub> has two energy gaps, with a  $\pi$ -band at 2.3 meV and a  $\sigma$ -band at 7.1 meV [64]. At a temperature much lower than its critical temperature, the BCS surface resistance  $R_s \sim (A\omega^2/T)\exp(-\Delta/k_bT)$  is dominated by the  $\pi$ -band, with  $A$  a material parameters-dependent coefficient. The BCS surface resistance of MgB<sub>2</sub> could potentially be much lower than that of Nb considering that Nb's energy gap is 1.5 meV. The coherence length of MgB<sub>2</sub> is about 5 nm. Experiments reveal that the grain boundaries of MgB<sub>2</sub> do exhibit suppression of supercurrent density [65, 66] in DC applications. However, in SRF applications, a MgB<sub>2</sub> film with large grain size is preferred because grain boundaries in the film could cause strong pinning, which would lead to high field Q drop [67]. RF penetration depth is 100~200 nm at temperatures below 5 K in applications in the GHz range. To shield most of the applied RF field, a film with several hundred nm thickness is preferred, which makes quality control harder. Compared to Nb, MgB<sub>2</sub> has a smaller lower critical field  $H_{c1}$  and a larger upper critical field  $H_{c2}$ , which are determined by its penetration depth and coherence length, respectively. The superheating critical field of MgB<sub>2</sub>, calculated from  $H_{sh} = 0.75\sqrt{H_{c1}H_{c2}}$  [17, 68], is 170~1000 mT depending on the field's direction [63], which suggests that it might be possible to achieve 200 MV/m gradient [69]. MgB<sub>2</sub> is also an attractive choice for multilayer film coatings to benefit from the lower surface resistance, which was proposed by Gurevich [70].

While past research has largely focused on polycrystalline MgB<sub>2</sub> [71], this study was initiated to reveal a relationship between thickness and SRF performance of single crystal MgB<sub>2</sub>. High quality MgB<sub>2</sub> films were grown epitaxially on C-plane sapphire substrates, Al<sub>2</sub>O<sub>3</sub>(0001), with a HPCVD technique [72, 73] and was characterized by EBSD with Pole Figures (PFs) for microstructure. We conducted a novel surface impedance characterization [15, 48] for films with 200 nm and 350 nm thickness. The SIC testing of SRF properties was set at 7.4 GHz, under different temperatures and applied fields with higher resolution than previous works [74-76].

## **7.2. Experimental details**

The principles of the HPCVD system were described in reference [72, 73]. The system has been modified to accommodate 5 cm substrate for potential SRF application. The system was pumped down below 10<sup>-2</sup> Torr. Then UHP hydrogen was introduced to flush the system. Deposition was conducted in a hydrogen atmosphere of 40 Torr to prevent oxidation. The substrate, along with Mg pellets placed nearby on the substrate heater, was heated to 750 °C, when the Mg pellets melted and a high Mg vapor pressure was generated near the substrate. A flow of 40 sccm diborane gas mixture (5% concentration in hydrogen) was then introduced. Diborane decomposed in the hot space near the substrate heater to provide active B atoms, which reacted with Mg vapor to form MgB<sub>2</sub> and deposit on the substrate. The growth rate is measured by etching step on the film with concentrated Hydrogen Chloride acid. A

Veeco dektak 150 surface profiler is used. The thicknesses are  $200\pm 15$  nm and  $350\pm 30$  nm for 4 min and 7 min deposition time, respectively.

Three 5 cm dia. samples have been fabricated for SRF property characterization, with two at 200 nm thickness (labeled as MgB<sub>2</sub>-200-I and MgB<sub>2</sub>-200-II) and one at 350 nm thickness (labeled as MgB<sub>2</sub>-350). Small samples with  $1\times 1$  cm<sup>2</sup> size and 350 nm thickness have been fabricated for surface characterization. Typical 5 cm dia. MgB<sub>2</sub> films grown under similar deposition conditions show a RMS surface roughness of 10 nm [77].

In previous studies [72, 73], XRD Bragg-Brentano survey ( $\theta$ - $2\theta$  scan), and  $\varphi$ -scan on the MgB<sub>2</sub> {1,1,-2,0} crystals plane were conducted to reveal the films' microstructure. Those XRD survey suggested that the MgB<sub>2</sub> films had epitaxially grown on SiC or C-plane sapphire crystals. The epitaxial relationship complies with crystallographic relationship: MgB<sub>2</sub>(0001)// SiC(0001) or Al<sub>2</sub>O<sub>3</sub>(0001).

Besides utilizing XRD, which probes a depth of about one micron, Electron backscattering diffraction (EBSD) technique was used in this work to investigate microstructure of the films' topmost layer, in depth of 40 nm, to ensure that the collected information comes from the MgB<sub>2</sub> film only and contains no information from substrate. The EBSD system applied in this study that made by EDAX-TSL™ company is installed on an Amray™ SEM. The EBSD setup is equipped with TSL-OIM™ software to acquire and index the crystallographic orientations. Principles of the EBSD technique may be found in Ref. [78]. Utilizing EBSD to characterize MgB<sub>2</sub> crystallites has not been previously reported. Since there is no such phase entry in the

OIM Data Collection™ 5.0, we established a new entry of MgB<sub>2</sub> by defining the crystal structure as P6/mmm space symmetry group, with the lattice constants  $a = 0.32$  nm and  $c = 0.39$  nm.

### 7.3. Surface characterization

Figure 7.1 is the EBSD data for a MgB<sub>2</sub>/C-plane sapphire film. The EBSD survey area of  $150 \times 150 \mu\text{m}^2$  with a  $5 \mu\text{m}$  e-beam step has an average Confident Index (CI) of 0.55. The [Min, Max] CI of the survey is [0.086, 0.74]. The average Image Quality (IQ) of the survey is 997. The IQ, being close to a well-ordered bulk metallic sample after annealing/chemical polishing, indicates that the film's crystal quality is high. Grayscale of the map is rendered by the CI of OIM™, with a grayscale rendering of the CI range [0.1, 0.743]. The entire survey area is rendered in red, which means every pixel is in the (0001) orientation. A hexagon in the figure represents the oriented real lattice.

For three largely-separated survey areas, the average crystallographic misorientation of each survey area is  $<0.3^\circ$ . The misorientation angle is a conventional parameter to gauge the crystal quality of a grain. Subgrains, strain, polygonizations, or other microstructure defects will lead to a larger misorientation angle. A misorientation  $<0.3^\circ$  in an area of  $150 \times 150 \mu\text{m}^2$  suggests the film is of reasonably good grain quality for SRF applications. Fig 1 c&d are PFs representative of the measurements of all survey areas. The PFs are exactly the same for all three survey areas. The converging of the PFs, along with misorientation plots and IPF

figures, all indicates the absence of grain boundaries ( $>0.3^\circ$ ) in the  $\text{MgB}_2$  film. In addition to using EBSD to deduce the stereographic projection PFs, XRD PF measurements were also conducted to visualize the film's reciprocal lattice space and to study the crystal textures in a larger area ( $\sim 3 \text{ mm}^2$ ). XRD measurements were conducted on X'Pert PRO MRD<sup>TM</sup> machine, being made by Philips<sup>TM</sup> (now Panalytical<sup>TM</sup>). For XRD Pole Figure (crystalline texture) measurement, it was setup as point focus. The incident side (X-ray source) was applied a crossed-slits collimator. The detector side was equipped a parallel-plate collimate. Both EBSD and XRD PFs are consistent, demonstrating the  $\text{MgB}_2$  are single crystal epitaxial films with a grain size only limited by substrate dimension at  $1 \times 1 \text{ cm}^2$ , following the epitaxial relationship  $\text{MgB}_2(0001) // \text{Al}_2\text{O}_3(0001)$ .

EDX and SEM have been placed to examine the chemical composition and surface morphology of the films. On SEM/EDX elemental analysis of B and Mg, the detector made by EDAX<sup>TM</sup> Company utilizes Super Ultra-Thin Window (Super UTW) technology, being configurable for light-element analysis down to Beryllium. The EDX analyzer is DPP-FR type. Quantitative technique of B and Mg atomic concentration ratios were referred to Birajdar and Eibl's work [79, 80]. The atomic percentage ratios of Mg vs B is approximately 1:2 with a  $\pm 10\%$  error. The film's outer most surface has a fairly flat but unique growth topography, which has been reported in Ref. [72].

#### **7.4. Surface impedance characterization**

The MgB<sub>2</sub> sample has been put at the open end of a TE<sub>011</sub> cylindrical Nb cavity with a sapphire rod inside, described in [15, 48]. The system provides a resonant field at 7.4 GHz. The cavity body, from which the sample is thermally isolated, is surrounded by liquid helium during the test, which differs from the previous measurements [74-76] by making the RF effect on sample the only contribution to the induced heat and resonance frequency change. Heat can be conducted from the sample only via the calorimeter. The effective surface impedance of the sample can be derived by directly substituting heater heat for RF heat under controlled RF field and temperature conditions. This system could detect as low as 1 μW power applied on the sample/sample holder, enabling the resolution of surface resistance as low as 1.2 nΩ at 5 mT peak magnetic field.

The effective surface impedance can be calculated from formula:

$$Z_s = \frac{E_z}{H_y} = \frac{P_{rf}}{\frac{1}{2} \int H^2(S) dS} + i\omega\mu_0\lambda = \frac{P_{rf}}{kB_{pk}^2} + i\omega\mu_0\left(\lambda_{ref} + \frac{f - f_{ref}}{M}\right)$$

$$\text{with } k = \frac{1}{2} \int B^2(S) dS / (\mu_0 B_{pk})^2$$

The real part is the effective surface resistance and imaginary part is the effective surface reactance.  $P_{rf}$  is the RF induced heat,  $B(S)$  is the magnetic field distribution on the sample,  $M$  is the tuning sensitivity that represents the ratio between frequency change and penetration depth change.  $k$  and  $M$  are geometry dependent coefficients and  $\omega$  is the resonant circular frequency. The RF induced heat is calculated from the difference between the power from the heater required to keep a constant sample

temperature without RF fields in the cavity and the power from the heater required to keep the sample's equilibrium temperature unchanged when RF fields are present, so called power compensation technique. The change of effective surface reactance is proportional to the change of effective penetration depth. It can be derived from changes of the resonant frequency of the TE<sub>011</sub> mode versus sample temperature.

The transition temperature can be measured from the loaded quality factor change while changing the sample temperature. The transition temperatures of MgB<sub>2</sub>-200-I and MgB<sub>2</sub>-200-II are both at 39.3±0.2 K, while that of MgB<sub>2</sub>-350 is at 39.5±0.2 K.

The penetration depth  $\lambda_s$  is derived from the effective penetration depth using  $\lambda_{eff} = \coth(d/\lambda_s)$  [81] with  $d$  the film thickness. The results are plotted in Figure 7.2. The measurement errors of penetration depth and sample temperature are 5% and 0.01 K, respectively. Theoretical value based on BCS theory [20] and Mattis-Bardeen's anomalous skin effect of a superconductor [21] is calculated using a code SRIMP, written by Halbritter [19]. The suggested parameters  $\hbar v_F/kT_c = 1.08$ , London penetration depth = 180 nm, coherence length = 6 nm, mean free path = 38 nm have been achieved using a fitting code written by Ciovati [26].

Figure 7.3 shows the effective surface resistance of the samples at 7.4 GHz, measured at temperatures between 2.1 K and 40 K, with peak fields between 0.6 mT and 3.7 mT. The surface resistance of a large grain Nb sample with 1:1:2 buffered chemical polish (BCP) solution of HF (49% wt), HNO<sub>3</sub> (69% wt), and H<sub>3</sub>PO<sub>4</sub> (85% wt) at room temperature [82], measured using the same apparatus, is plotted as a

reference. At temperatures above 4 K, the MgB<sub>2</sub>-350 sample has a lower surface resistance than Nb. At 2.2 K, the effective surface resistance decreased from 20  $\mu\Omega$  to 9  $\mu\Omega$  with the film thickness increase from 200 nm to 350 nm. The lowest effective surface resistance measured is  $9\pm 2 \mu\Omega$  at 2.2 K, which is consistent with the previous best reported results [76, 83, 84] using the  $f^2$  rule for normalization [76, 84], with much smaller systematic errors. We note that the 350 nm sample is less than two penetration depths thick at low temperatures and much less at higher temperatures. This must be taken into account when interpreting the effective surface resistance with respect to a BCS model. The microstructural defects or impurities revealed by XRD might explain why the samples' SRF performance < 4 K is not yet better than that of a near-perfect single crystal bulk Nb. XRD Bragg-Brentano survey ( $\theta/2\theta$  scan) found  $\Delta\theta$  of Full Width of Half Maximum (FWHM) at (0001) diffraction peak is 0.25°. XRD Rocking Curve measurement of (0001) diffraction peak reported its misorientation angle  $\sim 0.5^\circ$ . These measurements suggested that the crystal quality of the MgB<sub>2</sub> epitaxial films still have large room to be improved. For the MgB<sub>2</sub>-350 sample, the effective surface resistance versus magnetic field was measured with fields up to 10 mT at 3 K sample temperature. Results are shown in Figure 7.4. Effective surface resistance increased from 10  $\mu\Omega$  to 35  $\mu\Omega$  with increased fields from 0.5 mT to 10 mT. In Table 7.1, the difference in fabrication conditions and measurement results are summarized.

## 7.5. Conclusion



In conclusion, MgB<sub>2</sub> films on 5 cm sapphire disks have been fabricated using the HPCVD technique. EBSD and XRD PFs revealed that these films are single crystal. Surface impedance measurements at 7.4 GHz showed a decreasing effective surface resistance with increasing film thickness, with the lowest value at  $9\pm 2 \mu\Omega$  at 2.2 K. The 350 nm sample exhibited a lower surface resistance than Nb at temperatures above 4 K, and MgB<sub>2</sub>'s effective surface resistance at 3 K increased 3.5 times with increased fields from 0.5 mT to 10 mT. These non-linear losses clearly merit further investigation. Development of MgB<sub>2</sub> for SRF application will continue. Since the RF field only penetrates a few penetration depths into a superconductor, a coating of MgB<sub>2</sub> of several hundred nanometers on the inside surface of a metal cavity is sufficient for SRF cavity performances. HPCVD is a suitable technique for this purpose because it is adaptable to coating curved surfaces.

Table 7.1. Summary of difference in fabrication conditions and measurement results for MgB<sub>2</sub> samples.

	Deposition time [min]	Thickness [nm]	T <sub>c</sub> [K]	Rs at 2.2 K [μΩ]	Penetration depth change from 2.3 K to 35 K [nm]
MgB <sub>2</sub> -200-I	4	200±15	39.3 ± 0.2	26±6	360±20
MgB <sub>2</sub> -200-II	4	200±15		20±5	
MgB <sub>2</sub> -350	7	350±30	39.5 ± 0.2	9±2	373±20

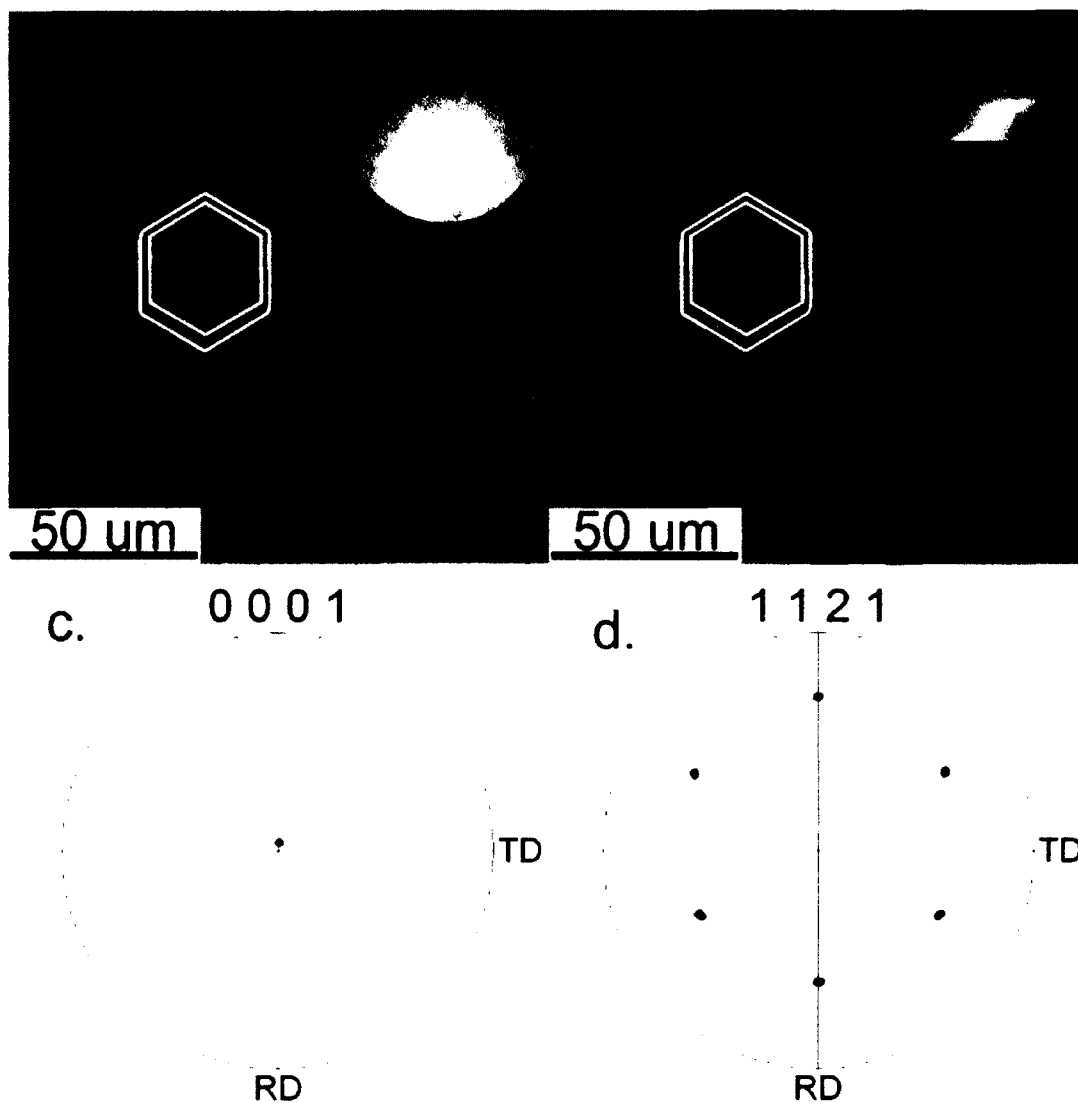


Figure 7.1. Electron backscattering diffraction (EBSD) results of a  $\text{MgB}_2$  film on C-plane sapphire. a). a scanning electron micrograph (SEM) of a survey area, the inset at top-right is a representative Kikuchi diffraction image, which shows clear diffraction bands. b). a color-coded inverse pole figure (IPF) of the same area, the inset at top-right is the color-coded crystallographic legend. c). and d). are the PFs being deduced from the EBSD survey in (0001) and (1,1,-2,1) representations respectively.

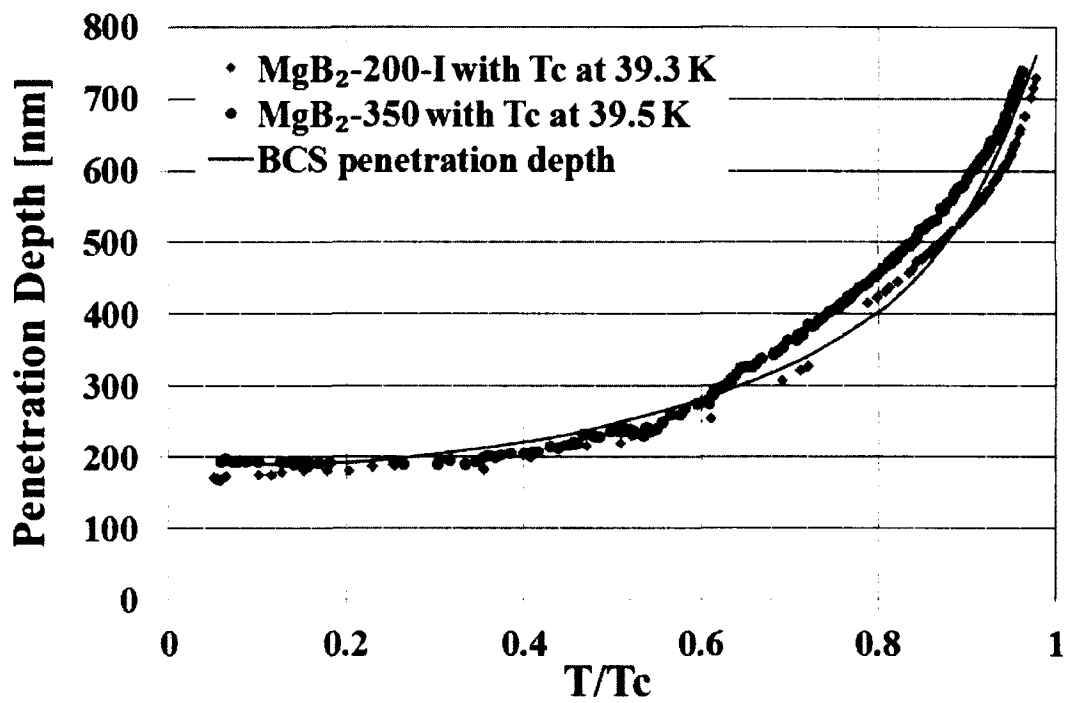


Figure 7.2. ◆ (blue) MgB<sub>2</sub>-200-I with T<sub>c</sub> at 39.3 K • (green) MgB<sub>2</sub>-350 with T<sub>c</sub> at 39.5 K Penetration depth versus sample temperature of MgB<sub>2</sub> on sapphire substrate – BCS penetration depth.

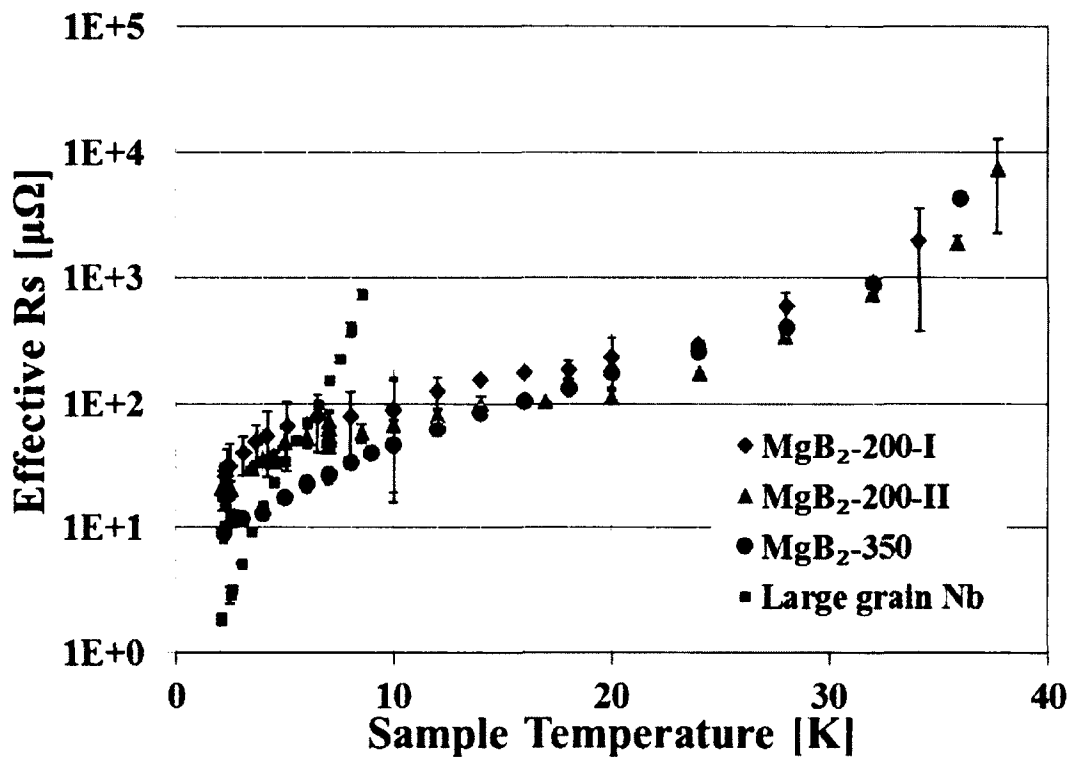


Figure 7.3.  $\blacklozenge$  (blue) MgB<sub>2</sub>-200-I  $\blacktriangle$  (red) MgB<sub>2</sub>-200-II  $\bullet$  (green) MgB<sub>2</sub>-350  
 Effective surface resistance versus sample temperature of MgB<sub>2</sub> on sapphire substrate  
 $\blacksquare$  (purple) Surface resistance versus sample temperature of large grain Nb sample.

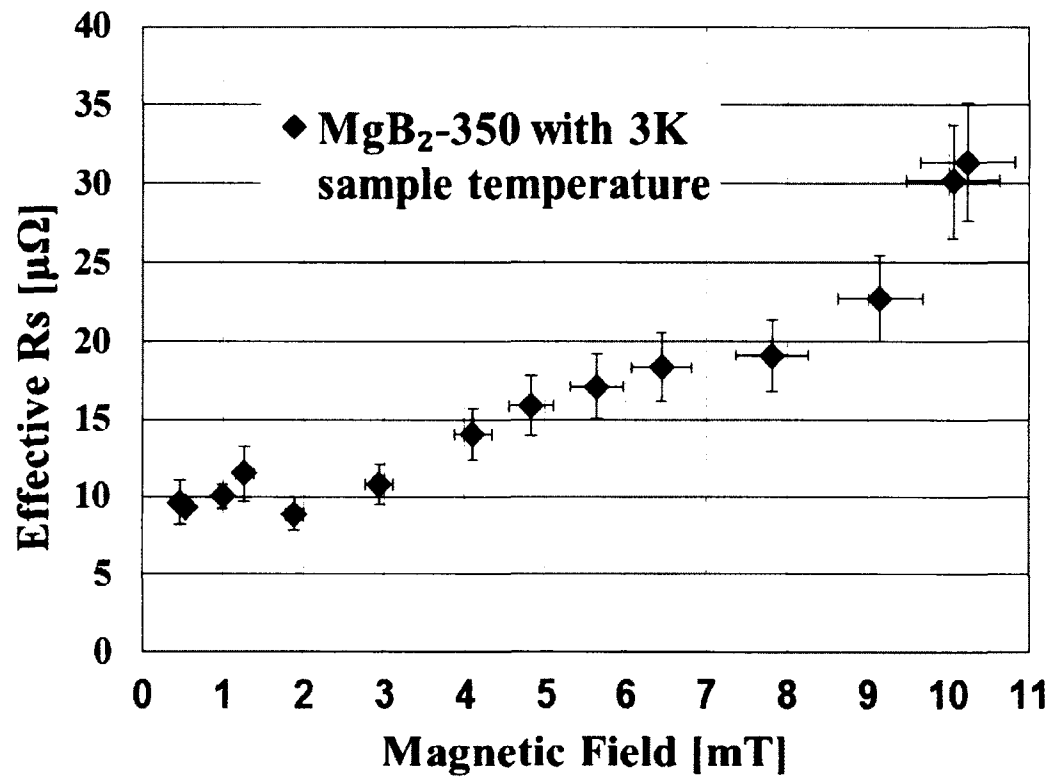


Figure 7.4. Effective surface resistance of MgB<sub>2</sub>-350 versus magnetic field at 3 K sample temperature.

## Appendix A

Math proof from equation (24) to (27) in Chapter 2.

$L(\omega, \varepsilon, \varepsilon', x, x')$

$$\begin{aligned}
 &= \frac{1}{4} \left( 1 + \frac{(\varepsilon + \varepsilon_s)(\varepsilon' + \varepsilon_s) + \Delta^2}{E_k E_{k'}} \right) \left( \frac{1}{E_{k+q\uparrow} - E_{k'+q\uparrow} + \hbar(\omega - iS)} \right. \\
 &+ \left. \frac{1}{E_{k+q\uparrow} - E_{k'+q\uparrow} - \hbar(\omega - iS)} \right) \left( \frac{f(E_{k'+q\uparrow}) + f(E_{-k'+q\downarrow})}{2} \right. \\
 &- \left. \frac{f(E_{k+q\uparrow}) + f(E_{-k+q\downarrow})}{2} \right) \\
 &+ \frac{1}{4} \left( 1 - \frac{(\varepsilon + \varepsilon_s)(\varepsilon' + \varepsilon_s) + \Delta^2}{E_k E_{k'}} \right) \left( \frac{1}{E_{k+q\uparrow} + E_{k'+q\uparrow} + \hbar(\omega - iS)} \right. \\
 &+ \left. \frac{1}{E_{k+q\uparrow} + E_{k'+q\uparrow} - \hbar(\omega - iS)} \right) \left( 1 - \frac{f(E_{k'+q\uparrow}) + f(E_{-k'+q\downarrow})}{2} \right. \\
 &- \left. \frac{f(E_{k+q\uparrow}) + f(E_{-k+q\downarrow})}{2} \right)
 \end{aligned}$$

Since the integration for  $x$  and  $x'$  are both from -1 to 1,  $L$  can be rewritten into,

$$\begin{aligned}
& L(\omega, \varepsilon, \varepsilon', x, x') \times \cos(\varepsilon' - \varepsilon) \\
&= \left[ \frac{1}{4} \left( 1 + \frac{(\varepsilon + \varepsilon_s)(\varepsilon' + \varepsilon_s) + \Delta^2}{E_k E_{k'}} \right) \left( \frac{1}{E_{k+q\uparrow} - E_{k'+q\uparrow} + \hbar(\omega - iS)} \right. \right. \\
&+ \left. \frac{1}{E_{k+q\uparrow} - E_{k'+q\uparrow} - \hbar(\omega - iS)} \right) \left( \frac{f(E_{k'+q\uparrow}) + f(E_{-k'+q\downarrow})}{2} \right. \\
&- \left. \left. \frac{f(E_{k+q\uparrow}) + f(E_{-k+q\downarrow})}{2} \right) \right. \\
&+ \left. \frac{1}{4} \left( 1 - \frac{(\varepsilon + \varepsilon_s)(\varepsilon' + \varepsilon_s) + \Delta^2}{E_k E_{k'}} \right) \left( \frac{1}{E_{k+q\uparrow} + E_{k'+q\uparrow} + \hbar(\omega - iS)} \right) \right. \\
&+ \left. \frac{1}{E_{k+q\uparrow} + E_{k'+q\uparrow} - \hbar(\omega - iS)} \right) \left( 1 - \frac{f(E_{k'+q\uparrow}) + f(E_{-k'+q\downarrow})}{2} \right. \\
&- \left. \left. \frac{f(E_{k+q\uparrow}) + f(E_{-k+q\downarrow})}{2} \right) \right] \times \cos(\varepsilon' - \varepsilon)
\end{aligned}$$

Define

$$E_+ = E_{k+q\uparrow} - \varepsilon'_{ext} + \hbar(\omega - iS)$$

$$E_- = E_{k+q\uparrow} - \varepsilon'_{ext} - \hbar(\omega - iS)$$

Separate  $L$  into six terms, with the first three parts times 1 and last three parts times the following factor,

$$\frac{(\varepsilon + \varepsilon_s)(\varepsilon' + \varepsilon_s) + \Delta^2}{E_k E_{k'}}$$

(1)

$$\begin{aligned}
& \frac{f(E_{k'+q\uparrow}) + f(E_{-k'+q\downarrow})}{2} \left( \frac{1}{E_{k+q\uparrow} - E_{k'+q\uparrow} + \hbar(\omega - iS)} + \frac{1}{E_{k+q\uparrow} - E_{k'+q\uparrow} - \hbar(\omega - iS)} \right. \\
&- \left. \frac{1}{E_{k+q\uparrow} + E_{k'+q\uparrow} + \hbar(\omega - iS)} - \frac{1}{E_{k+q\uparrow} + E_{k'+q\uparrow} - \hbar(\omega - iS)} \right)
\end{aligned}$$



$$\begin{aligned}
& \xrightarrow{\text{yields}} \frac{f(E_{k+q\uparrow}) + f(E_{-k+q\downarrow})}{2} \left( \frac{1}{E_{k'+q\uparrow} - E_{k+q\uparrow} + \hbar(\omega - is)} \right. \\
& \quad + \frac{1}{E_{k'+q\uparrow} - E_{k+q\uparrow} - \hbar(\omega - is)} - \frac{1}{E_{k+q\uparrow} + E_{k'+q\uparrow} + \hbar(\omega - is)} \\
& \quad \left. - \frac{1}{E_{k+q\uparrow} + E_{k'+q\uparrow} - \hbar(\omega - is)} \right) \\
& = - \frac{f(E_{k+q\uparrow}) + f(E_{-k+q\downarrow})}{2} \left( \frac{1}{E_{k+q\uparrow} - E_{k'+q\uparrow} + \hbar(\omega - is)} \right. \\
& \quad + \frac{1}{E_{k+q\uparrow} - E_{k'+q\uparrow} - \hbar(\omega - is)} + \frac{1}{E_{k+q\uparrow} + E_{k'+q\uparrow} + \hbar(\omega - is)} \\
& \quad \left. + \frac{1}{E_{k+q\uparrow} + E_{k'+q\uparrow} - \hbar(\omega - is)} \right)
\end{aligned}$$

(2)

$$\begin{aligned}
& - \frac{f(E_{k+q\uparrow}) + f(E_{-k+q\downarrow})}{2} \left( \frac{1}{E_{k+q\uparrow} - E_{k'+q\uparrow} + \hbar(\omega - is)} \right. \\
& \quad + \frac{1}{E_{k+q\uparrow} - E_{k'+q\uparrow} - \hbar(\omega - is)} + \frac{1}{E_{k+q\uparrow} + E_{k'+q\uparrow} + \hbar(\omega - is)} \\
& \quad \left. + \frac{1}{E_{k+q\uparrow} + E_{k'+q\uparrow} - \hbar(\omega - is)} \right) \\
& \xrightarrow{\text{yields}} - \frac{f(E_{k+q\uparrow}) + f(E_{-k+q\downarrow})}{2} \left( \frac{1}{E_{k+q\uparrow} - E_{k'+q\uparrow} + \hbar(\omega - is)} \right. \\
& \quad + \frac{1}{E_{k+q\uparrow} - E_{k'+q\uparrow} - \hbar(\omega - is)} + \frac{1}{E_{k+q\uparrow} + E_{-k'+q\downarrow} + \hbar(\omega - is)} \\
& \quad \left. + \frac{1}{E_{k+q\uparrow} + E_{-k'+q\downarrow} - \hbar(\omega - is)} \right)
\end{aligned}$$

$$\begin{aligned}
&= -\frac{f(E_{k+q\uparrow}) + f(E_{-k+q\downarrow})}{2} \left( \frac{1}{E_+ - E'} + \frac{1}{E_- - E'} + \frac{1}{E_+ + E'} + \frac{1}{E_- + E'} \right) \\
&= (f(E_{k+q\uparrow}) + f(E_{-k+q\downarrow})) \left( \frac{E_+}{E'^2 - E_+^2} + \frac{E_-}{E'^2 - E_-^2} \right)
\end{aligned}$$

(3)

$$\begin{aligned}
&\frac{1}{E_{k+q\uparrow} + E_{k'+q\uparrow} + \hbar(\omega - is)} + \frac{1}{E_{k+q\uparrow} + E_{k'+q\uparrow} - \hbar(\omega - is)} \\
&\xrightarrow{\text{yields}} \frac{1}{E_{k+q\uparrow} + E_{-k'+q\downarrow} + \hbar(\omega - is)} + \frac{1}{E_{k+q\uparrow} + E_{-k'+q\downarrow} - \hbar(\omega - is)} \\
&= \frac{1}{E_+ + E'} + \frac{1}{E_- + E'} = \frac{E' - E_+}{E'^2 - E_+^2} + \frac{E' - E_-}{E'^2 - E_-^2} \\
&= \frac{E' + E_+}{E'^2 - E_+^2} + \frac{E' + E_-}{E'^2 - E_-^2} - 2 \left( \frac{E_+}{E'^2 - E_+^2} + \frac{E_-}{E'^2 - E_-^2} \right)
\end{aligned}$$

(4)

$$\begin{aligned}
&\frac{f(E_{k'+q\uparrow}) + f(E_{-k'+q\downarrow})}{2} \left( \frac{1}{E_{k+q\uparrow} - E_{k'+q\uparrow} + \hbar(\omega - is)} + \frac{1}{E_{k+q\uparrow} - E_{k'+q\uparrow} - \hbar(\omega - is)} \right. \\
&\quad \left. + \frac{1}{E_{k+q\uparrow} + E_{k'+q\uparrow} + \hbar(\omega - is)} + \frac{1}{E_{k+q\uparrow} + E_{k'+q\uparrow} - \hbar(\omega - is)} \right) \\
&\xrightarrow{\text{yields}} \frac{f(E_{k+q\uparrow}) + f(E_{-k+q\downarrow})}{2} \left( \frac{1}{E_{k'+q\uparrow} - E_{k+q\uparrow} + \hbar(\omega - is)} \right. \\
&\quad + \frac{1}{E_{k'+q\uparrow} - E_{k+q\uparrow} - \hbar(\omega - is)} + \frac{1}{E_{k+q\uparrow} + E_{k'+q\uparrow} + \hbar(\omega - is)} \\
&\quad \left. + \frac{1}{E_{k+q\uparrow} + E_{k'+q\uparrow} - \hbar(\omega - is)} \right)
\end{aligned}$$

$$\begin{aligned}
&= -\frac{f(E_{k+q\uparrow}) + f(E_{-k+q\downarrow})}{2} \left( \frac{1}{E_{k+q\uparrow} - E_{k'+q\uparrow} + \hbar(\omega - is)} \right. \\
&\quad + \frac{1}{E_{k+q\uparrow} - E_{k'+q\uparrow} - \hbar(\omega - is)} - \frac{1}{E_{k+q\uparrow} + E_{k'+q\uparrow} + \hbar(\omega - is)} \\
&\quad \left. - \frac{1}{E_{k+q\uparrow} + E_{k'+q\uparrow} - \hbar(\omega - is)} \right)
\end{aligned}$$

(5)

$$\begin{aligned}
&-\frac{f(E_{k+q\uparrow}) + f(E_{-k+q\downarrow})}{2} \left( \frac{1}{E_{k+q\uparrow} - E_{k'+q\uparrow} + \hbar(\omega - is)} \right. \\
&\quad + \frac{1}{E_{k+q\uparrow} - E_{k'+q\uparrow} - \hbar(\omega - is)} - \frac{1}{E_{k+q\uparrow} + E_{k'+q\uparrow} + \hbar(\omega - is)} \\
&\quad \left. - \frac{1}{E_{k+q\uparrow} + E_{k'+q\uparrow} - \hbar(\omega - is)} \right) \\
&\xrightarrow{\text{yields}} -\frac{f(E_{k+q\uparrow}) + f(E_{-k+q\downarrow})}{2} \left( \frac{1}{E_{k+q\uparrow} - E_{k'+q\uparrow} + \hbar(\omega - is)} \right. \\
&\quad + \frac{1}{E_{k+q\uparrow} - E_{k'+q\uparrow} - \hbar(\omega - is)} - \frac{1}{E_{k+q\uparrow} + E_{-k'+q\downarrow} + \hbar(\omega - is)} \\
&\quad \left. - \frac{1}{E_{k+q\uparrow} + E_{-k'+q\downarrow} - \hbar(\omega - is)} \right) \\
&= -\frac{f(E_{k+q\uparrow}) + f(E_{-k+q\downarrow})}{2} \left( \frac{1}{E_+ - E'} + \frac{1}{E_- - E'} - \frac{1}{E_+ + E'} - \frac{1}{E_- + E'} \right) \\
&= (f(E_{k+q\uparrow}) + f(E_{-k+q\downarrow})) \left( \frac{E'}{E'^2 - E_+^2} + \frac{E'}{E'^2 - E_-^2} \right)
\end{aligned}$$

(6)

$$-\frac{1}{E_{k+q\uparrow} + E_{k'+q\uparrow} + \hbar(\omega - is)} - \frac{1}{E_{k+q\uparrow} + E_{k'+q\uparrow} - \hbar(\omega - is)}$$

$$\begin{aligned}
& \xrightarrow{\text{yields}} -\frac{1}{E_{k+q\uparrow} + E_{-k'+q\downarrow} + \hbar(\omega - is)} - \frac{1}{E_{k+q\uparrow} + E_{-k'+q\downarrow} - \hbar(\omega - is)} \\
& = -\frac{1}{E_+ + E'} - \frac{1}{E_- + E'} = -\frac{E' - E_+}{E'^2 - E_+^2} - \frac{E' - E_-}{E'^2 - E_-^2} \\
& = \frac{E' + E_+}{E'^2 - E_+^2} + \frac{E' + E_-}{E'^2 - E_-^2} - 2 \left( \frac{E'}{E'^2 - E_+^2} + \frac{E'}{E'^2 - E_-^2} \right)
\end{aligned}$$

Here  $\xrightarrow{\text{yields}}$  means (for integration purpose) the term on its left is mathematically the same as the term on its right by switching all components between with ' and without ' since  $\varepsilon$  and  $\varepsilon'$  are symmetric.

Here one may notice (1) = (2) and (4) = (5).

In (2)(3)(5) and (6), the following transformation has been applied,

$$\int_{-1}^1 f(x') dx' = - \int_{x'=-1}^{x'=1} f(x') d(-x') = \int_{-x'=-1}^{-x'=1} f(x') d(-x') = \int_{-1}^1 f(-x') dx'$$

In (3) and (6),

$$\begin{aligned}
& \frac{E' + E_+}{E'^2 - E_+^2} + \frac{E' + E_-}{E'^2 - E_-^2} = \frac{1}{E' - E_+} + \frac{1}{E' - E_-} \\
& = \frac{1}{E_{k'+q\uparrow} - E_{k+q\uparrow} - \hbar(\omega - is)} + \frac{1}{E_{k'+q\uparrow} - E_{k+q\uparrow} + \hbar(\omega - is)}
\end{aligned}$$

Since

$$\begin{aligned}
& \frac{1}{E_{k'+q\uparrow} - E_{k+q\uparrow} - \hbar(\omega - is)} = \frac{-1}{-E_{k'+q\uparrow} + E_{k+q\uparrow} + \hbar(\omega - is)} \\
& \xrightarrow{\text{yields}} \frac{-1}{-E_{k+q\uparrow} + E_{k'+q\uparrow} + \hbar(\omega - is)} = \frac{-1}{E_{k'+q\uparrow} - E_{k+q\uparrow} + \hbar(\omega - is)}
\end{aligned}$$

We have

$$\frac{E' + E_+}{E'^2 - E_+^2} + \frac{E' + E_-}{E'^2 - E_-^2} \xrightarrow{\text{yields}} 0$$

Add all terms together, we have

$$L(\omega, \varepsilon, \varepsilon', x, x')$$

$$= -\frac{1}{2}(1 - f(E_{k+q\uparrow}))$$

$$- f(E_{-k+q\downarrow}) \left\{ \frac{E + \varepsilon_{ext} + \hbar(\omega - iS) - \varepsilon_{ext}' + \frac{(\varepsilon + \varepsilon_s)(\varepsilon' + \varepsilon_s) + \Delta^2}{E}}{E'^2 - [E + \varepsilon_{ext} - \varepsilon_{ext}' + \hbar(\omega - iS)]^2} \right.$$

$$\left. + \frac{E + \varepsilon_{ext} - \hbar(\omega - iS) - \varepsilon_{ext}' + \frac{(\varepsilon + \varepsilon_s)(\varepsilon' + \varepsilon_s) + \Delta^2}{E}}{E'^2 - [E + \varepsilon_{ext} - \varepsilon_{ext}' - \hbar(\omega - iS)]^2} \right\}$$

## Appendix B

Math proof from equations (26)(27) to (28) in Chapter 2.

With  $s$  a small positive real number that finally goes to zero after integration,

$$L(\omega, \varepsilon, \varepsilon', x, x')$$

$$= -\frac{1}{2}(1 - f(E_{k+q\uparrow}))$$

$$- f(E_{-k+q\downarrow}) \left\{ \frac{E + \varepsilon_{ext} + \hbar(\omega - is) - \varepsilon_{ext}' + \frac{(\varepsilon + \varepsilon_s)(\varepsilon' + \varepsilon_s) + \Delta^2}{E}}{E'^2 - [E + \varepsilon_{ext} - \varepsilon_{ext}' + \hbar(\omega - is)]^2} \right.$$

$$\left. + \frac{E + \varepsilon_{ext} - \hbar(\omega - is) - \varepsilon_{ext}' + \frac{(\varepsilon + \varepsilon_s)(\varepsilon' + \varepsilon_s) + \Delta^2}{E}}{E'^2 - [E + \varepsilon_{ext} - \varepsilon_{ext}' - \hbar(\omega - is)]^2} \right\}$$

$$I(\omega, R, T, x, x') = \int_{-\infty}^{\infty} \int_{-\infty}^{\infty} \left[ L(\omega, \varepsilon, \varepsilon', x, x') + \frac{f(\varepsilon) - f(\varepsilon')}{\varepsilon' - \varepsilon} \right] \times \cos[\alpha(\varepsilon - \varepsilon')] d\varepsilon' d\varepsilon$$

The term additional to  $L$  goes to zero after integration, and the integration of  $\varepsilon$  could be changed to,

$$\int_{-\infty}^{\infty} function d\varepsilon = 2 \int_{\Delta}^{\infty} function \times \frac{E}{\varepsilon + \varepsilon_s} dE$$

For the first term of  $L$ ,

$$\int_{\Delta}^{\infty} \int_{-\infty}^{\infty} \left[ -(1 - f(E_{k+q\uparrow})) \right.$$

$$\left. - f(E_{-k+q\downarrow}) \frac{(E(E + \varepsilon_{ext} + \hbar(\omega - is) - \varepsilon_{ext}') + \Delta^2)/(\varepsilon + \varepsilon_s) + (\varepsilon' + \varepsilon_s)}{E'^2 - [E + \varepsilon_{ext} - \varepsilon_{ext}' + \hbar(\omega - is)]^2} \right]$$

$$\times \cos[\alpha(\varepsilon - \varepsilon')] d\varepsilon' dE$$

$$\begin{aligned} &\xrightarrow{\text{yields}} \int_{\Delta}^{\infty} \int_{-\infty}^{\infty} \left[ -(1 - f(E_{k+q\uparrow}) \right. \\ &\left. - f(E_{-k+q\downarrow})) \frac{(E(E - \varepsilon_{ext} + \hbar(\omega - is) + \varepsilon_{ext}') + \Delta^2)/(\varepsilon + \varepsilon_s) + (\varepsilon' + \varepsilon_s)}{E'^2 - [E - \varepsilon_{ext} + \varepsilon_{ext}' + \hbar(\omega - is)]^2} \right] \\ &\times \cos[\alpha(\varepsilon - \varepsilon')] d\varepsilon' dE \end{aligned}$$

Use

$$E_1 = E_a + \varepsilon_{ext} \text{ and } \varepsilon_1 + \varepsilon_s = \sqrt{E_1^2 - \Delta^2}$$

to replace  $E$  and  $\varepsilon$  in the above equation, and define,

$$E_2 = E_a + \varepsilon'_{ext} + \hbar\omega, \varepsilon_2 + \varepsilon_s = \sqrt{E_2^2 - \Delta^2} \text{ and}$$

$$g = \frac{E_1 E_2 + \Delta^2}{(\varepsilon_1 + \varepsilon_s)(\varepsilon_2 + \varepsilon_s)}$$

we have,

$$\begin{aligned} &\int_{\Delta}^{\infty} \int_{-\infty}^{\infty} \left[ -[1 - f(E_1 - \varepsilon_{ext}) - f(E_1 \right. \\ &\left. + \varepsilon_{ext})] \frac{(E_1(E_1 - \varepsilon_{ext} + \hbar(\omega - is) + \varepsilon_{ext}') + \Delta^2)/(\varepsilon_1 + \varepsilon_s) + (\varepsilon' + \varepsilon_s)}{E'^2 - [E_1 - \varepsilon_{ext} + \varepsilon_{ext}' + \hbar(\omega - is)]^2} \right] \\ &\times \cos[\alpha(\varepsilon_1 - \varepsilon')] d\varepsilon' dE_1 \\ &= \int_{\Delta}^{\infty} \int_{-\infty}^{\infty} \left[ -[1 - f(E_1 - \varepsilon_{ext}) - f(E_1 \right. \\ &\left. + \varepsilon_{ext})] \frac{\frac{E_1(E_a + \hbar\omega + \varepsilon_{ext}') + \Delta^2}{(\varepsilon_1 + \varepsilon_s)} + (\varepsilon' + \varepsilon_s) - i\hbar s E_1/(\varepsilon_1 + \varepsilon_s)}{E'^2 - [E_a + \varepsilon_{ext}' + \hbar(\omega - is)]^2} \right] \\ &\times \cos[\alpha(\varepsilon_1 - \varepsilon')] d\varepsilon' dE_1 \end{aligned}$$

$$\begin{aligned}
&= \int_{\Delta}^{\infty} \int_{-\infty}^{\infty} \left[ -[1 - f(E_1 - \varepsilon_{ext}) - f(E_1 \right. \\
&\quad \left. + \varepsilon_{ext})] \frac{\frac{E_1 E_2 + \Delta^2}{(\varepsilon_1 + \varepsilon_s)} + (\varepsilon' + \varepsilon_s) - i\hbar s E_1 / (\varepsilon_1 + \varepsilon_s)}{E'^2 - (E_2 - i\hbar s)^2} \right] \\
&\quad \times \cos[\alpha(\varepsilon_1 - \varepsilon')] d\varepsilon' dE_1 \\
&= \int_{\Delta - \varepsilon_{ext}}^{\infty} \int_{-\infty}^{\infty} \left[ -[1 - f(E_1 - \varepsilon_{ext}) - f(E_1 \right. \\
&\quad \left. + \varepsilon_{ext})] \frac{g(\varepsilon_2 + \varepsilon_s) + (\varepsilon' + \varepsilon_s) - i\hbar s E_1 / (\varepsilon_1 + \varepsilon_s)}{E'^2 - E_2^2 + \hbar^2 s^2 + 2i\hbar s E_2} \right] \\
&\quad \times \cos[\alpha(\varepsilon' - \varepsilon_1)] d\varepsilon' dE_a
\end{aligned}$$

Define

$$\varepsilon_z = \varepsilon' - \varepsilon_1 \text{ and } A = E'^2 - E_2^2 + \hbar^2 s^2$$

Above equation changes to

$$\begin{aligned}
&\int_{\Delta - \varepsilon_{ext}}^{\infty} \int_{-\infty}^{\infty} \left[ -[1 - f(E_1 - \varepsilon_{ext}) - f(E_1 \right. \\
&\quad \left. + \varepsilon_{ext})] \frac{g(\varepsilon_2 + \varepsilon_s) + (\varepsilon' + \varepsilon_s) - i\hbar s E_1 / (\varepsilon_1 + \varepsilon_s)}{A + 2i\hbar s E_2} \right] \\
&\quad \times \cos(\alpha \varepsilon_z) d\varepsilon_z dE_a
\end{aligned}$$

Its real part is



$$\int_{\Delta - \varepsilon_{ext}}^{\infty} \int_{-\infty}^{\infty} \left[ -[1 - f(E_1 - \varepsilon_{ext}) - f(E_1 + \varepsilon_{ext})] \frac{A[g(\varepsilon_2 + \varepsilon_s) + (\varepsilon' + \varepsilon_s)] - 2\hbar^2 s^2 E_1 E_2 / (\varepsilon_1 + \varepsilon_s)}{(A + 2i\hbar s E_2)(A - 2i\hbar s E_2)} \right] \times \cos(\alpha \varepsilon_z) d\varepsilon_z dE_a$$

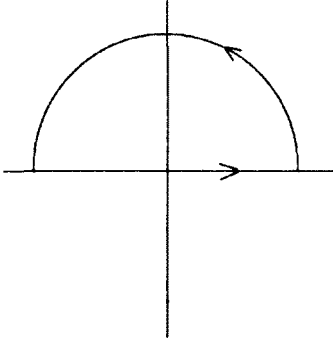
And its imaginary part is

$$\int_{\Delta - \varepsilon_{ext}}^{\infty} \int_{-\infty}^{\infty} \left[ -[1 - f(E_1 - \varepsilon_{ext}) - f(E_1 + \varepsilon_{ext})] \frac{-2i\hbar s E_2 [g(\varepsilon_2 + \varepsilon_s) + (\varepsilon' + \varepsilon_s)] - i\hbar s E_1 A / (\varepsilon_1 + \varepsilon_s)}{(A + 2i\hbar s E_2)(A - 2i\hbar s E_2)} \right] \times \cos(\alpha \varepsilon_z) d\varepsilon_z dE_a$$

One should notice terms  $2\hbar^2 s^2 E_1 E_2 / (\varepsilon_1 + \varepsilon_s)$  and  $i\hbar s E_1 A / (\varepsilon_1 + \varepsilon_s)$  are small and with  $s$  goes to zero, these terms also goes to zero.

In the real part, one can use  $e^{i\alpha \varepsilon_z}$  to replace  $\cos(\alpha \varepsilon_z)$  and choose the real part of final integration. In the imaginary part, do the same thing and choose the imaginary part of final integration.

For the contour integration of  $\varepsilon_z$ , in the complex plane of  $\varepsilon_z$ , we choose a semi-circle integration so that it includes the integration from negative infinite to positive infinite on the real axis. In this integration the poles in the 1<sup>st</sup> and 2<sup>nd</sup> quadrants should be excluded.



Now we evaluate the poles for the above two integrations,

Pole 1 at  $A + 2i\hbar s E_2 = 0$ ,

$$\varepsilon' + \varepsilon_s = \pm \sqrt{E_2^2 - \hbar^2 s^2 - 2i\hbar s E_2 - \Delta^2}$$

The + term makes  $\varepsilon_z$  in 3 or 4 quadrant in its complex plane (the imaginary part of  $\varepsilon_z$  to be negative), so we choose

$$\varepsilon' + \varepsilon_s = -\sqrt{E_2^2 - \hbar^2 s^2 - 2i\hbar s E_2 - \Delta^2} \xrightarrow{s \rightarrow 0} -(\varepsilon_2 + \varepsilon_s)$$

$$\varepsilon_z = \varepsilon' - \varepsilon_1 \xrightarrow{s \rightarrow 0} -(\varepsilon_2 + \varepsilon_s + \varepsilon_1 + \varepsilon_s)$$

Mathematically we have

$$\begin{aligned} & \left( \varepsilon' + \varepsilon_s + \sqrt{E_2^2 - \hbar^2 s^2 - 2i\hbar s E_2 - \Delta^2} \right) \left( \varepsilon' + \varepsilon_s - \sqrt{E_2^2 - \hbar^2 s^2 - 2i\hbar s E_2 - \Delta^2} \right) \\ & = A + 2i\hbar s E_2 \end{aligned}$$

Pole 2 at  $A - 2i\hbar s E_2 = 0$ ,

$$\varepsilon' + \varepsilon_s = \pm \sqrt{E_2^2 - \hbar^2 s^2 + 2i\hbar s E_2 - \Delta^2}$$

The - term makes  $\varepsilon_z$  in 3 or 4 quadrant in its complex plane (the imaginary part of  $\varepsilon_z$  to be negative), so we choose

$$\varepsilon' + \varepsilon_s = \sqrt{E_2^2 - \hbar^2 s^2 + 2i\hbar s E_2 - \Delta^2} \xrightarrow{s \rightarrow 0} \varepsilon_2 + \varepsilon_s$$

$$\varepsilon_z = \varepsilon' - \varepsilon_1 \xrightarrow{s \rightarrow 0} \varepsilon_2 - \varepsilon_1$$

Mathematically we have

$$\begin{aligned} & \left( \varepsilon' + \varepsilon_s + \sqrt{E_2^2 - \hbar^2 s^2 + 2i\hbar s E_2 - \Delta^2} \right) \left( \varepsilon' + \varepsilon_s - \sqrt{E_2^2 - \hbar^2 s^2 + 2i\hbar s E_2 - \Delta^2} \right) \\ & = A - 2i\hbar s E_2 \end{aligned}$$

So

$$\begin{aligned} It1 &= \int_{-\infty}^{\infty} \frac{A}{(A + 2i\hbar s E_2)(A - 2i\hbar s E_2)} \times e^{i\alpha \varepsilon_z} d\varepsilon_z \\ &= 2\pi i \frac{A}{(A + 2i\hbar s E_2)(A - 2i\hbar s E_2)} \left( \varepsilon' + \varepsilon_s \right. \\ & \quad \left. + \sqrt{E_2^2 - \hbar^2 s^2 - 2i\hbar s E_2 - \Delta^2} \right) e^{i\alpha \varepsilon_z} \quad \text{at pole 1} \\ & \quad + 2\pi i \frac{A}{(A + 2i\hbar s E_2)(A - 2i\hbar s E_2)} \left( \varepsilon' + \varepsilon_s \right. \\ & \quad \left. - \sqrt{E_2^2 - \hbar^2 s^2 + 2i\hbar s E_2 - \Delta^2} \right) e^{i\alpha \varepsilon_z} \quad \text{at pole 2} \end{aligned}$$

$$\xrightarrow{s \rightarrow 0} -\frac{\pi i}{2(\varepsilon_2 + \varepsilon_s)} e^{-i\alpha(\varepsilon_2 + \varepsilon_s + \varepsilon_1 + \varepsilon_s)} + \frac{\pi i}{2(\varepsilon_2 + \varepsilon_s)} e^{i\alpha(\varepsilon_2 - \varepsilon_1)}$$

$$It2 = \int_{-\infty}^{\infty} \frac{A \varepsilon_z}{(A + 2i\hbar s E_2)(A - 2i\hbar s E_2)} \times e^{i\alpha \varepsilon_z} d\varepsilon_z$$

$$\xrightarrow{s \rightarrow 0} \frac{\pi i(\varepsilon_2 + \varepsilon_s + \varepsilon_1 + \varepsilon_s)}{2(\varepsilon_2 + \varepsilon_s)} e^{-i\alpha(\varepsilon_2 + \varepsilon_s + \varepsilon_1 + \varepsilon_s)} + \frac{\pi i(\varepsilon_2 - \varepsilon_1)}{2(\varepsilon_2 + \varepsilon_s)} e^{i\alpha(\varepsilon_2 - \varepsilon_1)}$$

$$\begin{aligned}
& \int_{-\infty}^{\infty} \left[ -[1 - f(E_1 - \varepsilon_{ext}) - f(E_1 + \varepsilon_{ext})] \frac{A[g(\varepsilon_2 + \varepsilon_s) + (\varepsilon' + \varepsilon_s)]}{(A + 2i\hbar s E_2)(A - 2i\hbar s E_2)} \right] \\
& \quad \times \cos(\alpha \varepsilon_z) d\varepsilon_z \\
& = -[1 - f(E_1 - \varepsilon_{ext}) - f(E_1 + \varepsilon_{ext})] \times \{It1 \times [g(\varepsilon_2 + \varepsilon_s) + (\varepsilon_1 + \varepsilon_s)] + It2\} \\
& = -[1 - f(E_1 - \varepsilon_{ext}) - f(E_1 + \varepsilon_{ext})] \times \left[ \frac{\pi i}{2} (1 - g) e^{-i\alpha(\varepsilon_2 + \varepsilon_s + \varepsilon_1 + \varepsilon_s)} \right. \\
& \quad \left. + \frac{\pi i}{2} (1 + g) e^{i\alpha(\varepsilon_2 - \varepsilon_1)} \right] \\
& \xrightarrow{\text{real part}} -[1 - f(E_1 - \varepsilon_{ext}) - f(E_1 + \varepsilon_{ext})] \times \left\{ \frac{\pi}{2} (1 - g) \sin[\alpha(\varepsilon_2 + \varepsilon_s + \varepsilon_1 + \varepsilon_s)] \right. \\
& \quad \left. - \frac{\pi}{2} (1 + g) \sin[\alpha(\varepsilon_2 - \varepsilon_1)] \right\} \\
& It3 = \int_{-\infty}^{\infty} \frac{-2i\hbar s E_2}{(A + 2i\hbar s E_2)(A - 2i\hbar s E_2)} \times e^{i\alpha \varepsilon_z} d\varepsilon_z \\
& = 2\pi i \frac{-2i\hbar s E_2}{(A + 2i\hbar s E_2)(A - 2i\hbar s E_2)} \left( \varepsilon' + \varepsilon_s \right. \\
& \quad \left. + \sqrt{E_2^2 - \hbar^2 s^2 - 2i\hbar s E_2 - \Delta^2} \right) e^{i\alpha \varepsilon_z} \quad \text{at pole 1} \\
& \quad + 2\pi i \frac{-2i\hbar s E_2}{(A + 2i\hbar s E_2)(A - 2i\hbar s E_2)} \left( \varepsilon' + \varepsilon_s \right. \\
& \quad \left. - \sqrt{E_2^2 - \hbar^2 s^2 + 2i\hbar s E_2 - \Delta^2} \right) e^{i\alpha \varepsilon_z} \quad \text{at pole 2} \\
& \xrightarrow{s \rightarrow 0} -\frac{\pi i}{2(\varepsilon_2 + \varepsilon_s)} e^{-i\alpha(\varepsilon_2 + \varepsilon_s + \varepsilon_1 + \varepsilon_s)} - \frac{\pi i}{2(\varepsilon_2 + \varepsilon_s)} e^{i\alpha(\varepsilon_2 - \varepsilon_1)} \\
& It4 = \int_{-\infty}^{\infty} \frac{-2i\hbar s \varepsilon_z}{(A + 2i\hbar s E_2)(A - 2i\hbar s E_2)} \times e^{i\alpha \varepsilon_z} d\varepsilon_z
\end{aligned}$$

$$\begin{aligned}
& \xrightarrow{s \rightarrow 0} \frac{\pi i (\varepsilon_2 + \varepsilon_s + \varepsilon_1 + \varepsilon_s)}{2(\varepsilon_2 + \varepsilon_s)} e^{-i\alpha(\varepsilon_2 + \varepsilon_s + \varepsilon_1 + \varepsilon_s)} - \frac{\pi i (\varepsilon_2 - \varepsilon_1)}{2(\varepsilon_2 + \varepsilon_s)} e^{i\alpha(\varepsilon_2 - \varepsilon_1)} \\
& \int_{-\infty}^{\infty} \left[ -[1 - f(E_1 - \varepsilon_{ext}) - f(E_1 + \varepsilon_{ext})] \frac{-2i\hbar s E_2 [g(\varepsilon_2 + \varepsilon_s) + (\varepsilon' + \varepsilon_s)]}{(A + 2i\hbar s E_2)(A - 2i\hbar s E_2)} \right] \\
& \quad \times \cos(\alpha \varepsilon_z) d\varepsilon_z dE_a \\
& = -[1 - f(E_1 - \varepsilon_{ext}) - f(E_1 + \varepsilon_{ext})] \times \{It3 \times [g(\varepsilon_2 + \varepsilon_s) + (\varepsilon_1 + \varepsilon_s)] + It4\} \\
& = -[1 - f(E_1 - \varepsilon_{ext}) - f(E_1 + \varepsilon_{ext})] \times \left[ \frac{\pi i}{2} (1 - g) e^{-i\alpha(\varepsilon_2 + \varepsilon_s + \varepsilon_1 + \varepsilon_s)} \right. \\
& \quad \left. - \frac{\pi i}{2} (1 + g) e^{i\alpha(\varepsilon_2 - \varepsilon_1)} \right] \\
& \xrightarrow{\text{imaginary part}} -[1 - f(E_1 - \varepsilon_{ext}) - f(E_1 + \varepsilon_{ext})] \\
& \quad \times \left\{ \frac{\pi i}{2} (1 - g) \cos[\alpha(\varepsilon_2 + \varepsilon_s + \varepsilon_1 + \varepsilon_s)] \right. \\
& \quad \left. - \frac{\pi i}{2} (1 + g) \cos[\alpha(\varepsilon_2 - \varepsilon_1)] \right\}
\end{aligned}$$

Add real part and imaginary part together,

$$\begin{aligned}
& -[1 - f(E_1 - \varepsilon_{ext}) - f(E_1 + \varepsilon_{ext})] \left\{ \frac{\pi}{2} (1 - g) \{ \sin[\alpha(\varepsilon_2 + \varepsilon_s + \varepsilon_1 + \varepsilon_s)] + i \cos[\alpha(\varepsilon_2 + \varepsilon_s + \varepsilon_1 + \varepsilon_s)] \} \right. \\
& \quad \left. - \frac{\pi}{2} (1 + g) \{ \sin[\alpha(\varepsilon_2 - \varepsilon_1)] + i \cos[\alpha(\varepsilon_2 - \varepsilon_1)] \} \right\} \\
& = [1 - f(E_1 - \varepsilon_{ext}) - f(E_1 + \varepsilon_{ext})] \pi i \{ g \cos[\alpha(\varepsilon_1 + \varepsilon_s)] \\
& \quad + i \sin[\alpha(\varepsilon_1 + \varepsilon_s)] \} e^{-i\alpha(\varepsilon_2 + \varepsilon_s)}
\end{aligned}$$

Using  $E_2$  to replace  $E$  in the second term of  $L$ , this term can be calculated,

$$\begin{aligned}
& -[1 - f(E_2 - \varepsilon_{ext}) - f(E_2 + \varepsilon_{ext})] \pi i \{ g \cos[\alpha(\varepsilon_2 + \varepsilon_s)] \\
& \quad - i \sin[\alpha(\varepsilon_2 + \varepsilon_s)] \} e^{i\alpha(\varepsilon_1 + \varepsilon_s)}
\end{aligned}$$

The final result is

$$\begin{aligned}
& \pi i \int_{\Delta - \varepsilon_{ext}}^{\infty} [1 - f(E_1 - \varepsilon_{ext}) - f(E_1 + \varepsilon_{ext})] \{g \cos[\alpha(\varepsilon_1 + \varepsilon_s)] \\
& \quad + i \sin[\alpha(\varepsilon_1 + \varepsilon_s)]\} e^{-i\alpha(\varepsilon_2 + \varepsilon_s)} dE_a \\
& - \pi i \int_{\Delta - \varepsilon'_{ext} - \hbar\omega}^{\infty} [1 - f(E_2 - \varepsilon_{ext}) - f(E_2 + \varepsilon_{ext})] \{g \cos[\alpha(\varepsilon_2 + \varepsilon_s)] \\
& \quad - i \sin[\alpha(\varepsilon_2 + \varepsilon_s)]\} e^{i\alpha(\varepsilon_1 + \varepsilon_s)} dE_a
\end{aligned}$$

## Appendix C

Mathematica program for surface impedance calculation.

```
Clear["Global`*"]  
Physical constant  
  
Num = 20;  
  
h = 6.626`10 * 10^(-34 + Num);  
k = 1.38`10 * 10^(-23 + Num);  
e = 1.6`10 * 10^(-19);  
me = 9.11`10 * 10^(-31 + Num);  
c = 2.9979`10 * 10^8;  
 $\mu_0 = 4`10 * \pi * 10^(-7);$   
Parameters:  
  
Tc = 9.25`10;  
GapoverkTc = 1.85`10;  
 $\lambda L = 320`10;$   
 $\xi = 400`10;$   
l = 500`10;  
DebyeT = 275`10;  
Conditions :  
  
freq = 1.5`10;  
T = 2`10;  
Vs = 0`10;  
Derived parameters :  
  
Gap0 = GapoverkTc * k * Tc;  
Debye = k * DebyeT;  
 $\lambda L = \lambda L * 10^(-10);$   
 $\xi = \xi * 10^(-10);$   
l = l * 10^(-10);  
freq = freq * 10^9;  
 $\omega = 2`10 * \pi * freq;$   
photon = h * freq;  
Vf0[G_?NumericQ] := 2`10 *  $\pi * \pi * G * \xi / h;$ 
```

```

InteGap[G_?NumericQ] :=
  1/4*NIntegrate[1.0^10/√((ε+1/2*me*Vs*Vs)*(ε+1/2*me*Vs*Vs)+G*G)*
    (1.0^10-
      1.0^10/
        (Exp[√((ε+1/2*me*Vs*Vs)*(ε+1/2*me*Vs*Vs)+G*G)-me*Vf0[G]*Vs*x)/k/T]+
          1)-
      1.0^10/
        (Exp[√((ε+1/2*me*Vs*Vs)*(ε+1/2*me*Vs*Vs)+G*G)+me*Vf0[G]*Vs*x)/k/T]+
          1)), {ε, -Debye, Debye}, {x, -1, 1}] -
  1/4*NIntegrate[1.0^10/√ε*ε+Gap0*Gap0*
    (1.0^10-1.0^10/(Exp[√ε*ε+Gap0*Gap0]/k/T)+1)-
    1.0^10/(Exp[√ε*ε+Gap0*Gap0]/k/T)+1), {ε, -Debye, Debye}, {x, -1, 1}];

Gap = G /. FindRoot[InteGap[G], {G, Gap0}]

Vf = 2^10*π*π*Gap*ξ/h

Pf = me*Vf

Distribution of electrons:

sex1[x1_] := Pf*Vs*x1;
sex2[x2_] := Pf*Vs*x2;

f[En_] := 1^10/(Exp[En/k/T]+1);

En1[En_, x1_] := En+sex1[x1];
En2[En_, x2_] := En+sex2[x2]+photon;

g[En_, x1_, x2_] := (En1[En, x1]*En2[En, x2]+Gap*Gap)/√(En1[En, x1]*En1[En, x1]-Gap*Gap)/
  √(En2[En, x2]*En2[En, x2]-Gap*Gap);

g1b[En_, x1_, x2_] := (En1[En, x1]*En2[En, x2]+Gap*Gap)/√(Gap*Gap-En1[En, x1]*En1[En, x1])/
  √(En2[En, x2]*En2[En, x2]-Gap*Gap);

g2b[En_, x1_, x2_] := (En1[En, x1]*En2[En, x2]+Gap*Gap)/√(En1[En, x1]*En1[En, x1]-Gap*Gap)/
  √(Gap*Gap-En2[En, x2]*En2[En, x2]);

a1[q_, En_, x1_] := √(En1[En, x1]*En1[En, x1]-Gap*Gap)*2^10*π/h/Vf/q;
a2[q_, En_, x2_] := √(En2[En, x2]*En2[En, x2]-Gap*Gap)*2^10*π/h/Vf/q;
a3[q_] := 1^10/q/l;

a1b[q_, En_, x1_] := √(Gap*Gap-En1[En, x1]*En1[En, x1])*2^10*π/h/Vf/q;
a2b[q_, En_, x2_] := √(Gap*Gap-En2[En, x2]*En2[En, x2])*2^10*π/h/Vf/q;

Rab[a_, b_] :=
  -b/2+a*b/4*Log[(b*b+(1+a)*(1+a))/(b*b+(1-a)*(1-a))]+
  (1+b*b-a*a)/4*ArcTan[2*b/(b*b+a*a-1)]; b*b+a*a-1>0

Rab[a_, b_] :=
  -b/2+a*b/4*Log[(b*b+(1+a)*(1+a))/(b*b+(1-a)*(1-a))]+(1+b*b-a*a)/4*π/2;/
  b*b+a*a-1==0

Rab[a_, b_] :=
  -b/2+a*b/4*Log[(b*b+(1+a)*(1+a))/(b*b+(1-a)*(1-a))]+
  (1+b*b-a*a)/4*(ArcTan[2*b/(b*b+a*a-1)]+π); b*b+a*a-1<0

```



```

Sab[a_, b_] :=
a/2 - a*b/2*ArcTan[2*b/(b*b + a*a - 1)] +
(1 + b*b - a*a)/8*Log[(b*b + (1 + a)*(1 + a))/(b*b + (1 - a)*(1 - a))] /; b*b + a*a - 1 > 0

Sab[a_, b_] :=
a/2 - a*b/2*π/2 + (1 + b*b - a*a)/8*Log[(b*b + (1 + a)*(1 + a))/(b*b + (1 - a)*(1 - a))] /;
b*b + a*a - 1 == 0

Sab[a_, b_] := a/2 - a*b/2*(ArcTan[2*b/(b*b + a*a - 1)] + π) + (1 +
b*b - a*a)/8*Log[(b*b + (1 + a)*(1 + a))/(b*b + (1 - a)*(1 - a))] /; b*b + a*a - 1 < 0

nG = 10;

Ma[q_?NumericQ, x1_?NumericQ, x2_?NumericQ] :=
1/2 *
NIntegrate[
(f[En2[En, x2] + eext1[x1]] + f[En2[En, x2] - eext1[x1]] - f[En1[En, x1] + eext1[x1]] -
f[En1[En, x1] - eext1[x1]]) * (g[En, x1, x2] + 1) * Sab[a1[q, En, x1] - a2[q, En, x2], a3[q]] -
(2 - f[En2[En, x2] + eext1[x1]] - f[En2[En, x2] - eext1[x1]] - f[En1[En, x1] + eext1[x1]] -
f[En1[En, x1] - eext1[x1]]) * (g[En, x1, x2] - 1) * Sab[a1[q, En, x1] + a2[q, En, x2], a3[q]],
{En, Gap - eext1[x1], nG*Gap}] +
NIntegrate[(1 - f[En2[En, x2] + eext1[x1]] - f[En2[En, x2] - eext1[x1]]) *
(g1b[En, x1, x2] * Rab[a2[q, En, x2], a3[q] + alb[q, En, x1]] +
Sab[a2[q, En, x2], a3[q] + alb[q, En, x1]]), {En, Gap - eext2[x2] - photon, Gap - eext1[x1]}] /;
eext1[x1] < eext2[x2] + photon

Ma[q_?NumericQ, x1_?NumericQ, x2_?NumericQ] :=
1/2 *
NIntegrate[
(f[En2[En, x2] + eext1[x1]] + f[En2[En, x2] - eext1[x1]] - f[En1[En, x1] + eext1[x1]] -
f[En1[En, x1] - eext1[x1]]) * (g[En, x1, x2] + 1) * Sab[a1[q, En, x1] - a2[q, En, x2], a3[q]] -
(2 - f[En2[En, x2] + eext1[x1]] - f[En2[En, x2] - eext1[x1]] - f[En1[En, x1] + eext1[x1]] -
f[En1[En, x1] - eext1[x1]]) * (g[En, x1, x2] - 1) * Sab[a1[q, En, x1] + a2[q, En, x2], a3[q]],
{En, Gap - eext2[x2] - photon, nG*Gap}] +
NIntegrate[(1 - f[En1[En, x1] + eext1[x1]] - f[En1[En, x1] - eext1[x1]]) *
(g2b[En, x1, x2] * Rab[a1[q, En, x1], a3[q] + a2b[q, En, x2]] +
Sab[a1[q, En, x1], a3[q] + a2b[q, En, x2]]), {En, Gap - eext1[x1], Gap - eext2[x2] - photon}] /;
eext1[x1] > eext2[x2] + photon

Na[q_?NumericQ, x1_?NumericQ, x2_?NumericQ] :=
-1/2 *
NIntegrate[
(f[En2[En, x2] + eext1[x1]] + f[En2[En, x2] - eext1[x1]] - f[En1[En, x1] + eext1[x1]] -
f[En1[En, x1] - eext1[x1]]) *
((g[En, x1, x2] - 1) * Rab[a1[q, En, x1] + a2[q, En, x2], a3[q]] +
(g[En, x1, x2] + 1) * Rab[a1[q, En, x1] - a2[q, En, x2], a3[q]]),
{En, Gap - eext1[x1], nG*Gap}] /; eext1[x1] < eext2[x2] + photon

Na[q_?NumericQ, x1_?NumericQ, x2_?NumericQ] :=
-1/2 *
NIntegrate[
(f[En2[En, x2] + eext1[x1]] + f[En2[En, x2] - eext1[x1]] - f[En1[En, x1] + eext1[x1]] -
f[En1[En, x1] - eext1[x1]]) *
((g[En, x1, x2] - 1) * Rab[a1[q, En, x1] + a2[q, En, x2], a3[q]] +
(g[En, x1, x2] + 1) * Rab[a1[q, En, x1] - a2[q, En, x2], a3[q]]),
{En, Gap - eext2[x2] - photon, nG*Gap}] /; eext1[x1] > eext2[x2] + photon

```

```

qlimit =  $\pi / 2^{10} * \xi$ ;

Ke[q_?NumericQ] :=
  NIntegrate[Ma[q, x1, x2] + i * Na[q, x1, x2], {x1, -1^10, 1^10}, {x2, -1^10, 1^10},
    MaxPoints -> 1600] / q * 3^10 * 2^10 *  $\pi$  / (4^10 * h * Vf *  $\lambda L * \lambda L$ );

Z =
  i * 10^9 *  $\omega * \mu_0 * \pi$  / NIntegrate[Log[1 + Ke[q] / q^2], {q, 0, 100^10 / qlimit}, MaxPoints -> 40,
    EvaluationMonitor -> Print["q = ", q, " Ke[q] *  $\lambda L * \lambda L$  = ", Ke[q] *  $\lambda L * \lambda L$ ]]

```

## Appendix D

SuperFish code for SIC 2-D field simulation on 2<sup>nd</sup> generation cavity with 0.06 inch cap.

0 loss tangent of sapphire rod  
;Binping Xiao JLab 2010 TE011 cavity design.  
;For complex shape TE011, set ibound, nbsup, nbslo, nbslf, nbsrt to 0.  
;Sapphire is set to a little bit smaller than cavity to avoid "overlap".

```
$reg kprob=1,  
xreg1=0.01, kreg1=2,  
xreg2=11.29, kreg2=284,  
xreg3=11.30, kreg3=286,  
xreg4=11.46, kreg4=318,  
kmax=356,  
yreg1=0.59, lreg1=59,  
yreg2=0.6, lreg2=61,  
yreg3=1, lreg3=101,  
yreg4=1.93, lreg4=142,  
yreg5=2.16, lreg5=165,  
yreg6=2.54, lreg6=184,  
lmax=200,  
freq=7500,  
xdri=10.9, ydri=0.8,  
icylin=1,  
ibound=0,  
nbsup=0, nbslo=0, nbslf=0, nbsrt=0$
```

```
$po x=0,y=0$  
$po x=0,y=0.6$  
$po x=8.7,y=0.6$  
$po nt=2, x0=8.7, y0=0.95, R=0.35, THETA=0$  
$po nt=2, x0=9.1, y0=0.95, R=0.05, THETA=90$  
$po x=11.4, y=1$  
$po x=11.4, y=1.10$  
$po x=10.39, y=1.10$  
$po x=10.39, y=1.42$  
$po x=11.4, y=1.42$  
$po x=11.4, y=1.52$
```

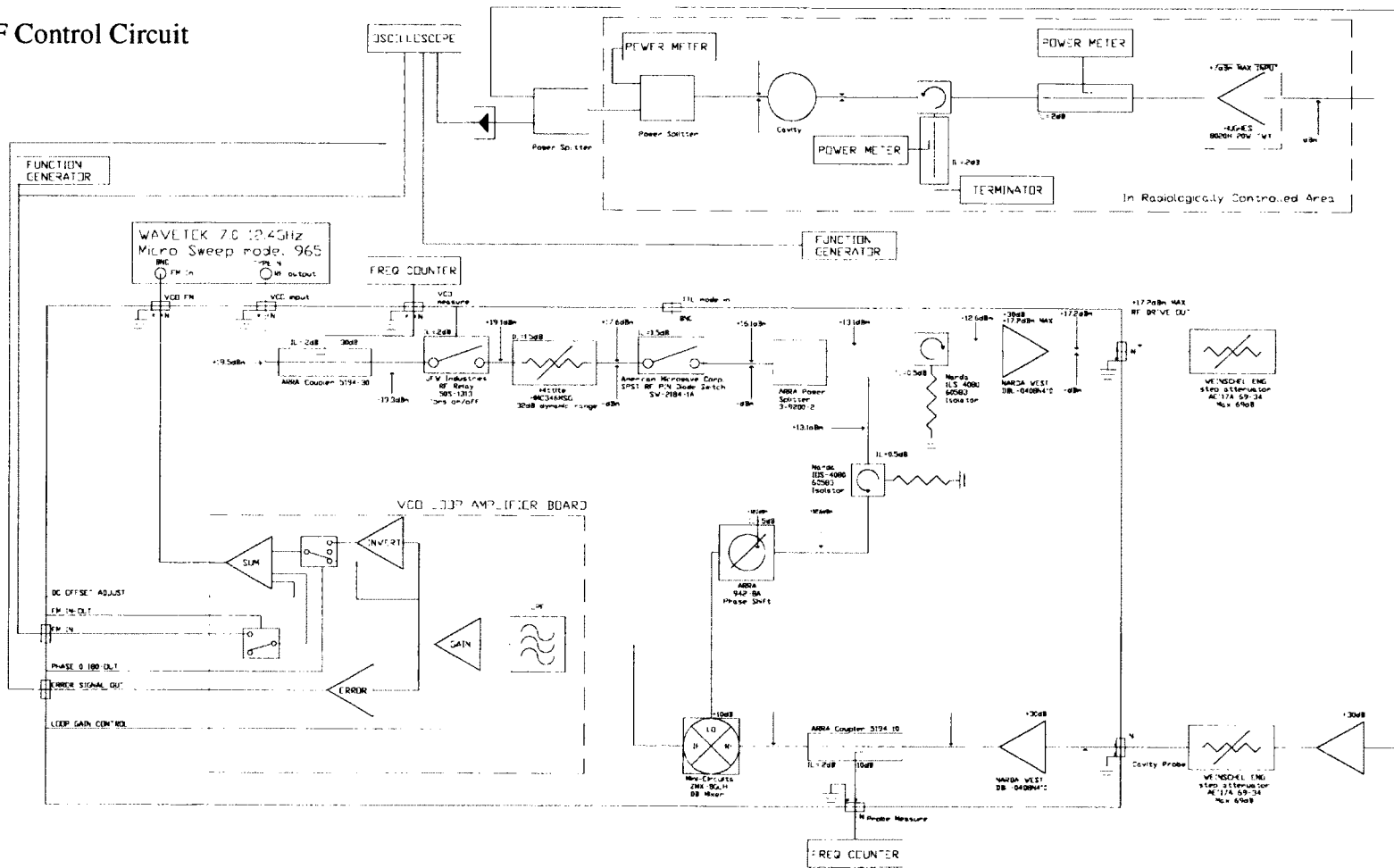
\$po x=10.39, y=1.52\$  
\$po x=10.39, y=1.84\$  
\$po x=11.4, y=1.84\$  
\$po x=11.4, y=1.93\$  
\$po x=11.29, y=1.93\$  
\$po x=11.29, y=2.7\$  
\$po x=16.4, y=2.7\$  
\$po x=16.4, y=2.54\$  
\$po x=11.30, y=2.54\$  
\$po x=11.30, y=2.16\$  
\$po x=11.45, y=2.16\$  
\$po x=11.45, y=0\$  
\$po x=0, y=0\$

\$reg mat=2, mtid=2\$  
\$po x=0.01, y=0\$  
\$po x=0.01, y=0.59\$  
\$po x=11.4, y=0.59\$  
\$po x=11.4, y=0\$  
\$po x=0.01, y=0\$

\$mt mtid=2  
epsilon=1  
mu=9.3\$

# Appendix E

## RF Control Circuit



## Appendix F

Input file for SuperFit 2.0, with first row the number of points for surface resistance and second row the number of points for penetration depth. Starting from the third row are data for surface resistance in ohm and penetration depth in angstrom, with first column the sample temperature in kelvin, second column the measured data and third column the error.

15		
32		
2.1	0.0000018	0.0000002
2.5	0.0000029	0.0000005
2.6	0.0000032	0.0000002
3	0.00000510	0.00000006
3.5	0.00000919	0.00000005
4	0.0000150	0.0000004
4.5	0.0000230	0.0000003
5	0.000034	0.000002
5.5	0.000051	0.000003
6	0.000070	0.000002
6.5	0.000099	0.000002
7	0.000153	0.000009
7.5	0.00023	0.00002
8	0.00039	0.00006
8.5	0.00074	0.00007
6.5	100	30
7	140	30
7.5	200	30
8	270	30
8.5	410	30
8.99	730	30
9	750	30
9.01	750	30
9.02	770	30
9.03	780	30

9.04	790	30
9.05	800	30
9.06	810	30
9.07	830	30
9.08	830	30
9.09	840	30
9.1	850	30
9.11	860	30
9.12	880	30
9.13	880	30
9.14	890	30
9.15	900	30
9.16	910	30
9.17	940	30
9.18	950	30
9.19	960	30
9.2	980	30
9.21	980	30
9.22	1020	30
9.23	1030	30
9.24	1050	30
9.25	1060	30

## Bibliography

1. Honkavaara, K., et al. *Status of the Free-Electron Laser User Facility FLASH*. in *Proceedings of the 14th International Conference on RF Superconductivity*. 2009. Berlin-Dresden, Germany.
2. Weise, H. *The European XFEL Based on Superconducting Technology*. in *Proceedings of the 14th International Conference on RF Superconductivity*. 2009. Berlin-Dresden, Germany.
3. Preble, J., et al. *JLab Upgrade and High Current Cavity Developments*. in *Proceedings of the 14th International Conference on RF Superconductivity*. 2009. Berlin-Dresden, Germany.
4. Mammosser, J. *Spallation Neutron Source Status and Upgrade Plans*. in *Proceedings of the 14th International Conference on RF Superconductivity*. 2009. Berlin-Dresden, Germany.
5. Mardor, I., et al. *The SARAF CW 40 MeV Proton/Deuteron Accelerator*. in *Proceedings of the 14th International Conference on RF Superconductivity*. 2009. Berlin-Dresden, Germany.
6. Yanagisawa, T., et al. *1500 MHZ Passive SRF Cavity for Bunch Lengthening in the NSLS-II Storage Ring*. in *Proceedings of the 23rd Particle Accelerator Conference*. 2009. Vancouver, Canada.
7. Belomestnykh, S. *Superconducting RF in Storage-Ring-Based Light Sources*. in *13th International Workshop on RF Superconductivity*. 2007. Beijing, China.
8. Chen, J.-e. *The Growth of SRF in China*. in *13th International Workshop on RF Superconductivity*. 2007. Beijing, China.
9. K.Hosoyama, et al. *Coconstruction and Commissioning of KEKB Superconducting Crab Cavities*. in *13th International Workshop on RF Superconductivity*. 2007. Beijing, China.



10. McIntosh, P., et al. *SRF System Operation on the ALICE ERL Facility at Daresbury*. in *Proceedings of the 14th International Conference on RF Superconductivity*. 2009. Berlin-Dresden, Germany.
11. Ben-Zvi, I. *ERL Prototype at BNL*. in *Proceedings of the 14th International Conference on RF Superconductivity*. 2009. Berlin-Dresden, Germany.
12. Elsen, E., et al., eds. *International Linear Collider A Technical Progress Report*.
13. Xiang, R., et al. *DC-SC Photo Injector with Low Emittance at Peking University*. in *Proceedings of 2005 Particle Accelerator Conference*. 2005. Knoxville, Tennessee.
14. Padamsee, H., J. Knobloch, and T. Hays, *RF Superconductivity for Accelerators*. 1998: Wiley-Interscience. 544.
15. Xiao, B.P., et al., *Radio frequency surface impedance characterization system for superconducting samples at 7.5 GHz*. *Review of Scientific Instruments*, 2011. **82**: p. 056104.
16. Pozar, D.M., *Microwave Engineering*. 2005: J. Wiley.
17. Hasan Padamsee, J.K., Tom Hays, *RF Superconductivity for Accelerators*. 1998.
18. Jensen, J.E., et al., eds. *Selected Cryogenic Data Notebook*. 1980.
19. Turneure, J.P., J. Halbritter, and H.A. Schwettman, *The surface impedance of superconductors and normal conductors: The Mattis-Bardeen theory*. *Journal of Superconductivity*, 1991. **4**(5): p. 341.
20. Bardeen, J., L.N. Cooper, and J.R. Schrieffer, *Theory of superconductivity*. *Physical Review*, 1957. **108**(5): p. 1175.
21. Mattis, D.C. and J. Bardeen, *Theory of the Anomalous Skin Effect in Normal and Superconducting Metals*. *Physical Review*, 1958. **111**(2): p. 412.
22. Miller, P.B., *Surface Impedance of Superconductors*. *Physical Review*, 1960. **118**(4): p. 928.
23. Gurevich, A., *Multiscale mechanisms of SRF breakdown*. *Physica C*, 2006. **441**: p. 38.

24. Bardeen, J., *Critical fields and Currents in Superconductors*. Reviews of Modern Physics, 1962. **34**(4): p. 667.
25. Kulik, I.O. and V. Palmieri, *Theory of Q-degradation and nonlinear effects in Nb-coated superconducting cavities*. Part. Accel., 1998. **60**: p. 257.
26. Ciovati, G., *Investigation of the Superconducting Properties of Niobium Radiofrequency Cavities*. 2005, Old Dominion University: Norfolk VA. p. 218.
27. Delayen, J.R., C.L. Bohn, and C.T. Roche, *Measurements of the Surface Resistance of High-Tc Superconductors at High RF Fields*. Journal of Superconductivity, 1990. **3**(3): p. 243-250.
28. Allen, L.H., *The Surface Resistance of Superconducting A15 Niobium-Tin Films at 8.6 GHz*, in *Physics*. 1986, Stanford University: Standord, California. p. 98.
29. Phillips, L., et al., *A Sapphire Loaded TE011 Cavity for Superconducting Impedance Measurements - Design, Construction and Commissioning Status*. SRF2005, 2005.
30. Fouaidy, M., et al., *New Results on RF Properties of Superconducting Niobium Films Using a Thermometric System*, in *Proceedings of the 8th European Particle Accelerator Conference*. 2002, EPS-IGA and CERN: Paris, France. p. 2229-2231.
31. Liang, C., *A New Surface Resistance Measurement Method with Ultrahigh Sensitivity*, in *Physics*. 1993, Virginia Polytechnic Institute and State University: Blacksburg, Virginia. p. 167.
32. Kneisel, P., G. Muller, and C. Reece, *Investigation of the Surface Resistance of Superconducting Niobium Using Thermometry in Superfluid Helium*. IEEE Transactions on Magnetics, 1987. **MAG-23**(2): p. 1417-1421.
33. Nantista, C., et al., *Test Bed for Superconducting Materials*, in *Proceedings of the 2005 Particle Accelerator Conference*. 2005. p. 4227-4229.
34. Phillips, L., et al., *A SAPPHIRE LOADED TE011 CAVITY FOR SURFACE IMPEDANCE MEASUREMENTS – DESIGN, CONSTRUCTION, AND COMMISSIONING STATUS*, in *Proceedings of the 12th International Workshop on RF Superconductivity*. 2005. p. 349-351.

35. Klein, N., et al., *Millimeter wave surface resistance of epitaxially grown YBa<sub>2</sub>Cu<sub>3</sub>O<sub>7-x</sub> thin films*. Applied Physics Letter, 1988. **54**: p. 757-759.
36. Tonkin, B.A. and Y.G. Proykova, *modular system for microwave surface impedance measurement of high temperature superconductors*. Superconductor Science and Technology, 1993. **6**: p. 353-359.
37. Misra, M., N.D. Kataria, and G.P. Srivastava, *Laterally resolved microwave surface-resistance measurement of high-T<sub>c</sub> superconductor Samples by Cavity Substitution Technique*. IEEE TRANSACTIONS ON MICROWAVE THEORY AND TECHNIQUES, 2000. **48**(5): p. 791-801.
38. Nantista, C., et al., *Test Bed for Superconducting Materials*. PAC 2005, 2005: p. 3.
39. Guo, J., et al. *Cryogenic RF Material Testing with a High-Q Copper Cavity*. in *Advanced Accelerator Concepts: 14th Workshop*. 2011: American Institute of Physics.
40. Martinet, G., et al., *Development of a TE<sub>011</sub> Cavity for Thin-Films Study*, in *Proceedings of the 14th International Conference on RF Superconductivity*. 2009: BERLIN-DRESDEN, GERMANY. p. 293-296.
41. Mahner, E., et al., *A new instrument to measure the surface resistance of superconducting samples at 400 MHz*. Review of Scientific Instruments, 2003. **74**(7): p. 3390-3394.
42. Junginger, T., W. Weingarten, and C. Welsch, *RF CHARACTERIZATION OF SUPERCONDUCTING SAMP*, in *Proceedings of the 14th International Conference on RF Superconductivity*. 2009: BERLIN-DRESDEN, GERMANY. p. 130-136.
43. Kneisel, P., G. Muller, and C. Reece, *INVESTIGATION OF THE SURFACE RESISTANCE OF SUPERCONDUCTING NIOBIUM USING THERMOMETRY IN SUPERFLUID HELIUM*. IEEE TRANSACTIONS ON MAGNETICS, 1987. **MAG-23**(2): p. 1417-1421.
44. Rubin, D.L., et al., *Observation of a narrow superconducting transition at 6GHz in crystals of YBCO*. Physical Review B, 1988. **38**, Number 10: p. 5.
45. Ormeno, R.J., et al., *Sapphire resonator for the measurement of surface impedance of high-temperature superconducting thin films*. Review of Scientific Instruments, 1997. **68**(5): p. 2121-2126.

46. Conway, Z.A., et al. *ILC Testing Program at Cornell University*. in *Proceedings of the 14th International Conference on RF Superconductivity*. 2009. Berlin-Dresden, Germany.
47. Xiao, B.P., et al. *RF Surface Impedance Measurement of Polycrystalline and Large Grain Nb Disk Sample at 7.5 GHz*. in *Proceedings of the 14th International Conference on RF Superconductivity*. 2009. Berlin-Dresden, Germany.
48. Xiao, B.P., et al. *Commissioning of the SRF Surface Impedance Characterization System at Jefferson Lab*. in *Proceedings of the 23rd Particle Accelerator Conference*. 2009. Vancouver, Canada.
49. Zhao, Y. and M.D. Cole, *The analysis of the cross-talk in a RF gun superconducting cavity*. PAC 2003, 2003.
50. Witek, G., et al., *Interaction of platinum colloids with single crystalline oxide and graphite substrates a combined AFM STM and XPS study*. *Catalysis Letters*, 1996. **37**: p. 35.
51. Schilcher, T., *Vector Sun Control of Pulsed Accelerating Fields in Lorentz Force Detuned Superconducting Cavities*. 1998: p. 137.
52. Matsuo, T., *Low temperature calorimetry for weakly interacting molecular systems*. *Pure and Applied Chemistry*, 1995. **67**(6): p. 911.
53. R. W. Newsome, J. and E.Y. Andrei, *Relaxation calorimetry technique for measuring low temperature specific heat*. *Review of Scientific Instruments*, 2004. **75**(1): p. 104.
54. Jensen, J.E., et al., *Brookhaven National Laboratory Selected Cryogenic Data Notebook*. Brookhaven National Laboratory Selected Cryogenic Data Notebook, 1980.
55. LakeShore, *User's Manual Model 332 Temperature Controller*, in *User's Manual Model 332 Temperature Controller*. 2005: Westerville, Ohio.
56. Keithley, *Model 2000 Multimeter User's Manual*, in *Model 2000 Multimeter User's Manual*. 2010: Cleveland, Ohio.
57. LakeShore, *Temperature Measurement and Control Catalog*, in *Temperature Measurement and Control Catalog*. 2004: Westerville, Ohio.

58. Gemme, G., et al., *rf surface resistance measurements of binary and ternary niobium compounds*. J. Appl. Phys., 1994. **77**(1).
59. Tajima, T., *possibility of MgB<sub>2</sub> application to superconducting cavities*. Eighth European Particle Accelerator Conference (EPAC2002), 2002.
60. Mathur, M.P., D.W. Deis, and J.R. Gavaler, *Lower Critical Field Measurements in NbN Bulk and Thin Films*. J. Appl. Phys., 1972. **43**(7).
61. Geng, R.L., et al. *High Gradient Studies for ILC With Single-Cell Re-Entrant Shape and Elliptical Shape Cavities Made of Fine-Grain and Large-Grain Niobium*. in *Proceedings of 2007 Particle Accelerator Conference*. 2007. Albuquerque, New Mexico.
62. Nagamatsu, J., et al., *Superconductivity at 39 K in magnesium diboride*. Nature, 2001. **410**: p. 63.
63. Buzea, C. and T. Yamashita, *Review of the superconducting properties of MgB<sub>2</sub>*. Superconductor Science and Technology 2001. **14**: p. 115.
64. Iavarone, M., et al., *Two-Band Superconductivity in MgB<sub>2</sub>*. Physical Review Letters, 2002. **89**: p. 187002.
65. Samanta, S.B., et al., *Grain boundaries as weak links The case of MgB<sub>2</sub> with reference to YNi<sub>2</sub>B<sub>2</sub>C*. Physical Review B, 2002. **65**: p. 092510.
66. Eisterer, M., *Magnetic Properties and Critical Currents of MgB<sub>2</sub>*. Superconductor Science and Technology, 2007. **20**: p. R47.
67. Gurevich, A. and G. Ciovati, *Dynamics of vortex penetration, jumpwise instabilities, and nonlinear surface resistance of type-II superconductors in strong rf fields*. Physical Review B, 2008. **77**: p. 104501.
68. Catelani, G. and J.P. Sethna, *Temperature dependence of the superheating field for superconductors in the high-k London limit*. Physical Review B, 2008. **78**: p. 224509.
69. Hand, E., *Can triniobium tin shrink accelerators*. Nature, 2008. **456**: p. 555.
70. Gurevich, A., *Enhancement of rf breakdown field of superconductors by multilayer coating*. Applied Physics Letter, 2006. **88**: p. 012511.
71. Putti, M., et al., *Two-band effects in the transport properties of MgB<sub>2</sub>*. Superconductor Science and Technology, 2003. **16**: p. 188.

72. ZENG, X., et al., *In situ epitaxial MgB<sub>2</sub> thin films for superconducting electronics*. Nature Materials, 2002. **1**: p. 35.
73. Zhuang, C., et al., *Clean MgB<sub>2</sub> thin films on different types of single-crystal substrate fabricated by hybrid physical-chemical vapor deposition*. Superconductor Science and Technology, 2009. **22**: p. 025002.
74. Zaitsev, A.G., et al., *Microwave properties of MgB<sub>2</sub> thin films prepared in situ by thermal evaporation combined with sputtering*. Journal of Physics: Conference Series, 2006. **43**: p. 309.
75. Jin, B.B., et al., *Energy gap, penetration depth and surface resistance of MgB<sub>2</sub> thin films determined by microwave resonator measurements*. Physical Review B: Condensed Matter and Materials Physics, 2001. **66**(10): p. 104521.
76. Klein, N., et al., *Microwave Properties of MgB<sub>2</sub> Thin Films*. IEEE Transactions on Applied Superconductivity, 2003. **13**(2): p. 3253.
77. Tan, T., et al., *Scale-up of hybrid physical chemical vapor deposition for large-area MgB<sub>2</sub> films*. unpublished.
78. HUMPHREYS, F.J., *Grain and subgrain characterisation by electron backscatter diffraction*. Journal of Material Science, 2001. **36**: p. 3833.
79. Birajdar, B., N. Peranio, and O. Eibl, *Quantitative electron microscopy and spectroscopy of MgB<sub>2</sub> wires and tapes*. Superconductor Science and Technology, 2008. **21**: p. 073001.
80. Birajdar, B., N. Peranio, and O. Eibl, *Quantitative Boron-Analysis Using EDX in SEM and TEM*. Microsc Microanal, 2007. **13**: p. 290.
81. Klein, N., et al., *The effective microwave surface impedance of high T<sub>c</sub> thin films*. Journal of Applied Physics, 1990. **67**(11): p. 6940.
82. Kneisel, P. *Surface Preparation of Niobium*. in *First Workshop on RF Superconductivity*. 1980. Karlsruhe, Germany.
83. Pogrebnyakov, A.V., et al., *Polycrystalline MgB<sub>2</sub> Films on Flexible YSZ Substrates Grown by Hybrid Physical-Chemical Vapor Deposition*. IEEE Transactions on Applied Superconductivity, 2007. **17**(2): p. 2854.
84. Oates, D.E., Y.D. Agassi, and B.H. Moeckly, *Intermodulation Distortion and Nonlinearity in MgB<sub>2</sub>: Experiment and Theory*. IEEE Transactions on Applied Superconductivity, 2007. **17**(2): p. 2871-2874.